

¹ Measurements of the $\cos\phi$ and $\cos 2\phi$ Moments of the Unpolarized SIDIS
² π^+ Cross-section at CLAS12

³ Richard Capobianco,^{1,2} M. Zurek,² Timothy B. Hayward,¹
⁴ Kyungseon Joo,¹ Stefan Diehl,¹ Andrey Kim,¹ and Marshall Scott²

⁵ *University of Connecticut, Storrs, Connecticut 06269*

⁶ *Argonne National Laboratory, Argonne, Illinois 60439*

⁷ (Dated: February 23, 2023)

⁸ Semi-inclusive deep inelastic π^+ electroproduction has been studied with the
⁹ CLAS12 detector at Jefferson Laboratory. Data was taken with a polarized 10.6
¹⁰ GeV electron beam, interacting with an unpolarized liquid hydrogen target. The
¹¹ collected statistics enable a high-precision study of the $\cos\phi$ and $\cos 2\phi$ azimuthal
¹² moments of the unpolarized cross-sections. These azimuthal moments may probe
¹³ the Boer-Mulders function, which describes the net transverse polarization of quarks
¹⁴ inside an unpolarized proton, and the Cahn effect, which has a purely kinematic
¹⁵ origin. The high statistics data will, for the first time, enable a multidimensional
¹⁶ analysis of both moments over a large kinematic range of Q^2 , x_B , z , and P_T . We will
¹⁷ present the status of this ongoing analysis, including the multidimensional unfolding
¹⁸ procedures used for acceptance corrections.

¹⁹ Current Version of Analysis Note: v3
²⁰ Released on February 22, 2023 for April APS 2023

²¹ Version v2 was released on October 1, 2022 for DNP 2022
²² Version v1 was released on August 2, 2022 for GRC 2022

23

CONTENTS

24	I. Introduction	3
25	II. Data Analysis	7
26	A. Resources	7
27	B. Data Set	7
28	C. PID	7
29	D. Fiducial Cuts	8
30	III. Channel Selection	9
31	IV. Distributions	10
32	V. Binning	13
33	VI. Monte Carlo	15
34	A. Description	15
35	B. Data vs MC Comparison	24
36	C. MC Event Matching	29
37	D. Acceptance Matrices	29
38	VII. Unfolding ϕ_h Distributions	32
39	VIII. Plots Requested for Release	43
40	IX. Appendix	56
41	References	60

42

I. INTRODUCTION

43 The study of semi-inclusive deep inelastic scattering (SIDIS) experiments offers opportunities
 44 to address questions about the three-dimensional structure of nucleons via their relationship to
 45 transverse momentum dependent parton distribution functions (TMDs). This analyses aims to study
 46 TMDs related to the unpolarized SIDIS cross-section for charged pion electroproduction in order to
 47 gain a greater understanding of the transverse motion of quarks and gluons inside the proton.

48 SIDIS reactions are described by $l(\ell) + N(P) \rightarrow l'(\ell') + h(P_h) + X(P_X)$ where an initial lepton
 49 beam (l) scatters off of a target nucleon (N) to produce a scattered lepton (l') and a single hadron
 50 (h). All other particles that may exist in the final state (X) are ignored. In this analysis, the initial
 51 lepton is a polarized electron while the nucleon is an unpolarized liquid hydrogen (i.e., a proton)
 52 target. In the final state, at least one scattered electron and π^+ pion are detected. Here, ℓ , P , ℓ' ,
 53 P_h , and P_X are the 4-momenta of their respective particles.

From this reaction, several important kinematic variables used in this analysis include (but are not limited to),

$$Q^2 = -q^2 \quad (1)$$

$$W^2 = (P + q)^2 \quad (2)$$

$$\nu = \frac{q \cdot P}{M} = E - E' \quad (3)$$

$$x_B = \frac{Q^2}{2P \cdot q} = \frac{Q^2}{2M\nu} \quad (4)$$

$$y = \frac{P \cdot q}{P \cdot \ell} = \frac{\nu}{E} \quad (5)$$

$$z = \frac{P \cdot P_h}{P \cdot q} = \frac{E_h}{\nu} \quad (6)$$

$$\gamma = \frac{2Mx}{Q} \quad (7)$$

$$\epsilon = \frac{1 - y - \frac{1}{4}\gamma^2y^2}{1 - y + \frac{1}{2}y^2 + \frac{1}{4}\gamma^2y^2} \quad (8)$$

$$x_F = \frac{2P_h \cdot q}{|q|W} \quad (9)$$

54 The exchanged virtual photon is defined as $q = \ell - \ell'$ such that $Q^2 = -q^2$ is the hard scale of the
 55 process (the virtuality of the exchanged photon). Conversely, W is the mass of the virtual photon,
 56 target system. If the electron beam has energy E and the scattered electron has energy E' then ν is
 57 defined as the difference between these two quantities. The variables x_B , y and z are the fraction of
 58 target momentum carried by the struck quark, the fraction of beam energy transferred to the virtual
 59 photon and the fraction of virtual photon energy carried by the hadron system. x_B here is therefore
 60 also known as “x-Bjorken”. The quantity γ describes the relationship between the energy transferred
 61 to the struck quark and the virtual photon energy. ϵ is the ratio of the longitudinal and transverse
 62 virtual photon flux. The “x-Feynman” variable, x_F , can be used to differentiate between current and
 63 target fragmentation and takes a positive value if the outgoing hadron moves in the same direction
 64 as the incoming electron, in the struck quark center-of-mass frame. Additionally, other important
 65 variables include P_T , which is the transverse momentum of the final state hadron, and ϕ_h , which is

the angle between the lepton scattering plane and the hadron production plane, according to the ‘Trento-convention’ [1]. Both of these variables can be directly measured in the target rest frame where the q -vector is along the z-axis (shown in Figure 1)¹.

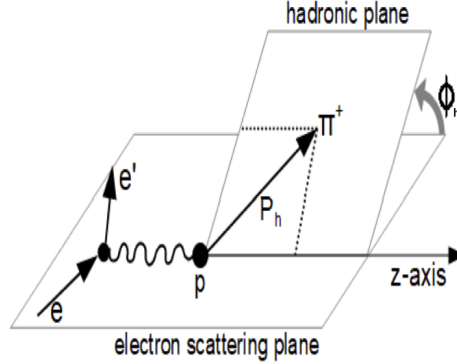


FIG. 1: Definition of the reaction kinematics of single pion SIDIS. Shows definition of ϕ_h (P_T is the perpendicular component of P_h with respect to the z-axis).

As this experiment involves an unpolarized target, by assuming single photon exchange and averaging over the beam polarization, the lepton-hadron SIDIS cross-section can be written as (see [2]):

$$\frac{d^5\sigma}{dx_B dQ^2 dz d\phi_h dP_{h\perp}^2} = A_0(1 + A_{UU}^{\cos \phi_h} \cos \phi_h + A_{UU}^{\cos 2\phi_h} \cos 2\phi_h) \quad (10)$$

where:

$$A_0 = \frac{2\pi\alpha^2}{x_B y Q^2} \frac{y^2}{2(1-\epsilon)} \left(1 + \frac{\gamma^2}{2x_B}\right) (F_{UU,T} + \epsilon F_{UU,L}) \quad (11)$$

$$A_{UU}^{\cos \phi_h} = \frac{\sqrt{2\epsilon(1+\epsilon)} F_{UU}^{\cos \phi_h}}{(F_{UU,T} + \epsilon F_{UU,L})} \quad (12)$$

$$A_{UU}^{\cos 2\phi_h} = \frac{\epsilon F_{UU}^{\cos 2\phi_h}}{(F_{UU,T} + \epsilon F_{UU,L})} \quad (13)$$

Here the functions F are the structure functions with the first subscript representing the beam polarization, the second subscript representing the target polarization, and the third subscript (if there is one) representing the virtual photon polarization, where U, L, and T are short for unpolarized, longitudinally polarized, and transversely polarized, respectively. At leading twist and next to leading twist, and by neglecting the higher twists (twists greater than or equal to three can be taken to be zero in the Wandzura-Wilezak approximation), these structure functions can be written as [2, 3]:

$$F_{UU}^{\cos 2\phi_h} = \mathcal{C} \left[-\frac{2(\hat{\mathbf{h}} \cdot \mathbf{p}_T)(\hat{\mathbf{h}} \cdot \mathbf{k}_T) - \mathbf{k}_T \cdot \mathbf{p}_T}{MM_h} h_1^\perp H_1^\perp + \dots \right] \quad (14)$$

$$F_{UU}^{\cos \phi_h} = \frac{2M}{Q} \mathcal{C} \left[-\frac{\hat{\mathbf{h}} \cdot \mathbf{k}_T}{M_h} x h H_1^\perp - \frac{\hat{\mathbf{h}} \cdot \mathbf{p}_T}{M} f_1 D_1 + \dots \right] \quad (15)$$

¹ This is the same center-of-mass frame in which x_F is also measured

where:

- \mathbf{p}_T = the transverse momentum of the struck quark
- \mathbf{k}_T = the transverse part of \mathbf{P}_h with respect to the quark direction
- $\mathbf{P}_{h\perp}$ = the transverse part of \mathbf{P}_h with respect to the virtual photon momentum
- $\hat{\mathbf{h}} = \frac{\mathbf{P}_{h\perp}}{|\mathbf{P}_{h\perp}|}$
- M = Mass of Nucleon
- M_h = Mass of Hadron
- x = Momentum fraction
- h = Unpolarized twist-3 TMD
- h_1^\perp = Boer-Mulders function
- H_1^\perp = Collins function
- f_1 = Unpolarized TMD
- D_1 = Unpolarized Fragmentation Function

69 The Boer-Mulders function is the main focus of this analysis. The Cahn effect is a kinematic
70 effect that will also be considered, as it is related to the $\frac{2M}{Q} \mathcal{C}[\frac{\hat{\mathbf{h}} \cdot \mathbf{p}_T}{M} f_1 D_1]$ term given above.²

This analysis ultimately aims to perform a multidimensional measurement of the $\cos \phi$ and $\cos 2\phi$ azimuthal moments of the unpolarized SIDIS π^+ cross-section which are sensitive to Cahn and Boer-Mulders effects. The cross-section moments (A_0 , $A_{UU}^{\cos \phi_h}$, and $A_{UU}^{\cos 2\phi_h}$) will be extracted from the fits of the ϕ_h distribution in different Q^2 , x_B , z , and P_T bins, with the function:

$$A(1 + B \cos \phi_h + C \cos 2\phi_h) \quad (16)$$

71 where the moments can then be expressly given as $A_0 = A$, $A_{UU}^{\cos \phi_h} = B$, and $A_{UU}^{\cos 2\phi_h} = C$.

To take the experimental measurements that are necessary, the SIDIS cross-section can be extracted from the following formula:

$$\frac{d^5\sigma}{dQ^2 dx_B dP_T dz d\phi_h} = \frac{1}{\Gamma_\nu} \frac{1}{\Delta Q^2 \Delta x_B \Delta P_T \Delta z \Delta \phi_h} \frac{N}{R \cdot BC \cdot \eta \cdot N_0} \frac{1}{(N_A \cdot \rho \cdot t / A_w)} \quad (17)$$

where:

- Γ_ν = Virtual Photon Flux
- R = Radiative Correction Factor
- N = Bin Yields
- BC = a factor which evolves bin-averaged differential cross-section to a specific kinematic point within the bin
- η = Acceptance Correction
- N_0 = Life-time corrected incident electron flux
- N_A = Avogadro's Number
- ρ = target density
- t = target length
- A_w = Atomic weight of the target

² The Cahn effect is not itself a TMD function.

⁷² Also, the ‘ Δ ’ terms on the right side of the equation refer to the bin volume of the particular bin
⁷³ that the cross-section is being measured in, while the last term in the equation refers to the target
⁷⁴ number density. Specifically, the whole term is one over the target number density.

At this time, no radiative corrections or bin averaging corrections have been completed (i.e., the factors R and BC have not been calculated). BC is a conversion factor which converts between the number of events within a given kinematic bin into the differential cross-section measurement which corresponds to specific points within that bin. The radiative correction factor R will be determined in a similar method as the acceptance corrections, in that the effects will be studied using the Monte Carlo Simulation. Acceptance corrections factor η can be calculated using a bin-by-bin comparison between the Monte Carlo Reconstructed and Generated data sets. In other words, for a bin that yielded N events in the experimental data,

$$\eta = \frac{\text{Number of Events Reconstructed Per Bin}}{\text{Number of Events Generated Per Bin}} \quad (18)$$

in the same bin from the Monte Carlo simulations. The radiative correction factor R can be defined in a similar fashion, with events with and without radiative effect taking the place of the number of reconstructed and generated events respectively so that

$$R = \frac{\text{Number of Events Per Bin With Raditative Effects}}{\text{Number of Events Per Bin Without Raditative Effects}} \quad (19)$$

⁷⁵ Additional methods of obtaining this acceptance correction do exist, including the use of Acceptance
⁷⁶ matrices, which help to minimize the bin migration effects and the event generator dependence in
⁷⁷ acceptance corrections. Further discussions of these matrices will be included in the **Acceptance**
⁷⁸ **Matrices** section later in this analysis note.

⁷⁹ The azimuthal modulation analysis requires multidimensional acceptance correction in Q^2 , x_B ,
⁸⁰ z , and P_T . The current stage of the analysis focuses on studying the bin migration effects and
⁸¹ acceptance correction. Only one dimensional acceptance matrices and the unfolded distributions
⁸² obtained by their use will be presented in this note.

83

II. DATA ANALYSIS

84

A. Resources

85 The data analysis procedure followed here is largely identical to that of several fully approved and
 86 published RG-A first experiment SIDIS analyses (inclusive π^+ and inclusive $\pi^+\pi^-$ papers) [4, 5]. In
 87 addition to these we make specific use of the following analysis notes:

- 88 • RG-A Common Analysis: https://clas12-docdb.jlab.org/DocDB/0009/000949/001/RGA_Analysis_Overview_and_Procedures-08172020.pdf
- 90 • “Back-to-back” (b2b) π^+ -proton analysis: <https://clas12-docdb.jlab.org/DocDB/0009/000935/007/v3%20to%20be%20submitted%20to%20the%20reviewers.pdf>

92

B. Data Set

93 The analyzed data corresponds to the RG-A Fall 2018 **inbending** runs with a polarized electron
 94 beam incident on a liquid hydrogen target. This analysis used **only the forward detector** of
 95 CLAS12 which contains a tracking subsystem consisting of drift chambers in a toroidal magnetic
 96 field and high and low threshold cherenkov counters to identify the scattered electron and final state
 97 hadrons, respectively.

98 Momentum corrections were also applied to the electron and π^+ pions in the selected events.
 99 These corrections were developed in a separate analysis using exclusive reactions to corrected the
 100 Missing Mass spectrum in exclusive $ep \rightarrow e\pi^+N$ reactions. Using these reactions, it was possible
 101 to calculate the ‘correct’ kinematics for the electron and the π^+ pion based on the other particle’s
 102 kinematics using 4-vector momentum conservation. The corrections were obtained by comparing the
 103 calculated momentum of the particles with their experimentally measured values to plot $\Delta P_{\text{Particle}} =$
 104 $p_{\text{Calculated}} - p_{\text{Measured}}$ versus p_{Measured} in different regions of the particle’s lab angle (ϕ). The final
 105 results of this procedure were independent momentum corrections for both particles that were sector-
 106 dependent functions of the measured momentum and azimuthal angles. These corrections were
 107 applied to the experimental data sample after the initial event selection cuts were applied (see below
 108 for details regarding the cuts). The effects of these corrections are demonstrated in Figures 55-56 in
 109 the **Appendix** section as examples. (For more details on these corrections, see **CLAS12 Momentum**
 110 **Corrections**)

111

C. PID

112 The RG-A Analysis Overview and Procedures note, pg. 58 [6] goes into significant detail about
 113 the common particle identification scheme used for RG-A. The first layer of identification is the
 114 CLAS12 EventBuilder which is used to associate detector responses from various CLAS12 subsystems
 115 to particles via an identification protocol. The resulting information is output to dedicated data
 116 structures, called HIPO banks, for further physics analysis. This first level of particle assignment by
 117 the EventBuilder is relatively loose and significant refinement was added on top of it to improve the

¹¹⁸ PID quality. The identification schema described in the following sections corresponds to the final
¹¹⁹ selection criteria used in this analysis.

¹²⁰ A full description of the electron PID used here with numerous supporting plots can be found in
¹²¹ the b2b analysis note starting on pg. 19. The criteria are as follows:

- ¹²² • Forward Detector
- ¹²³ • > 2 photoelectrons detected in the HTCC (b2b note Fig. 10)
- ¹²⁴ • > 0.07 GeV energy deposited in the PCAL (b2b note Fig. 11)
- ¹²⁵ • sector dependent sampling fraction cut (b2b note Fig. 12)
- ¹²⁶ • “diagonal cut” for electrons above 4.5 GeV (HTCC threshold) (b2b note Fig. 14)
- ¹²⁷ • $y < 0.75$, not strictly an “electron cut”, but sets the minimum electron energy approximately
¹²⁸ greater than 2.4 GeV

¹²⁹ A full description of the π^+ PID used here with numerous supporting plots can be found in the
¹³⁰ b2b analysis note starting on pg. 25. The criteria are as follows:

- ¹³¹ • Forward Detector
- ¹³² • $p > 1.25$ GeV
- ¹³³ • Refined chi2pid cuts. The corrected standard deviation σ of chipid is set to 0.88 for π^+ s.
¹³⁴ Lower bound of the cut is $\text{chi2pid} > -3\sigma$. Upper bound below 2.44 GeV is $\text{chi2pid} < 3\sigma$
¹³⁵ and above is set at 1/2 the distance in β between kaons and pions, by requiring chi2pid
¹³⁶ $< \sigma (0.00869 + 14.98587 \cdot e^{-p/1.18236} + 1.81751 \cdot e^{-p/4.86394})$.

¹³⁷ D. Fiducial Cuts

¹³⁸ A detailed discussion and explanation of the fiducial cuts placed on the calorimeter and drift
¹³⁹ chambers can be found in the RG-A Common Analysis note, pg. 70 [6] or on pg. 29 of the b2b note.
¹⁴⁰ Additional fiducial cuts were added to remove “bad detectors”, with [Figure 2](#) illustrating the effects
¹⁴¹ of these cuts.

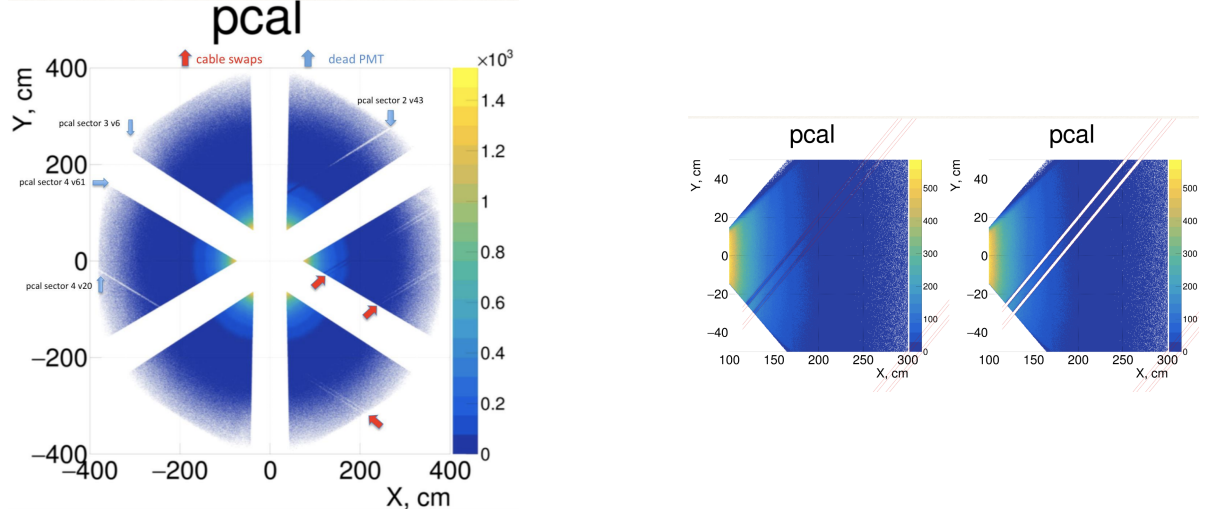


FIG. 2: PCAL stands for the Preshower Calorimeter. Code detailing exact cuts is included in the [Appendix](#) (Images and Code developed by Valerii Klimenko).

142

III. CHANNEL SELECTION

143 We avoid contamination from the target fragmentation region by requiring $x_F > 0$, contributions
 144 from exclusive meson production by requiring $M_X > 1.5$ GeV and limit radiative effects by requiring
 145 $y < 0.75$. To ensure good data and Monte Carlo matching, an additional the cut is placed on
 146 $Q^2 < 2$ GeV 2 to avoid acceptance edge effects. The cut was made to follow after the Q^2 peak in
 147 the data, with a sample image of this distribution shown below in [Figure 3](#). Other images of the
 148 kinematic distributions, including those showing some of the previously described cuts, will be shown
 149 in other sections of this analysis note, namely in the [Plots Requested for Release](#) Section.

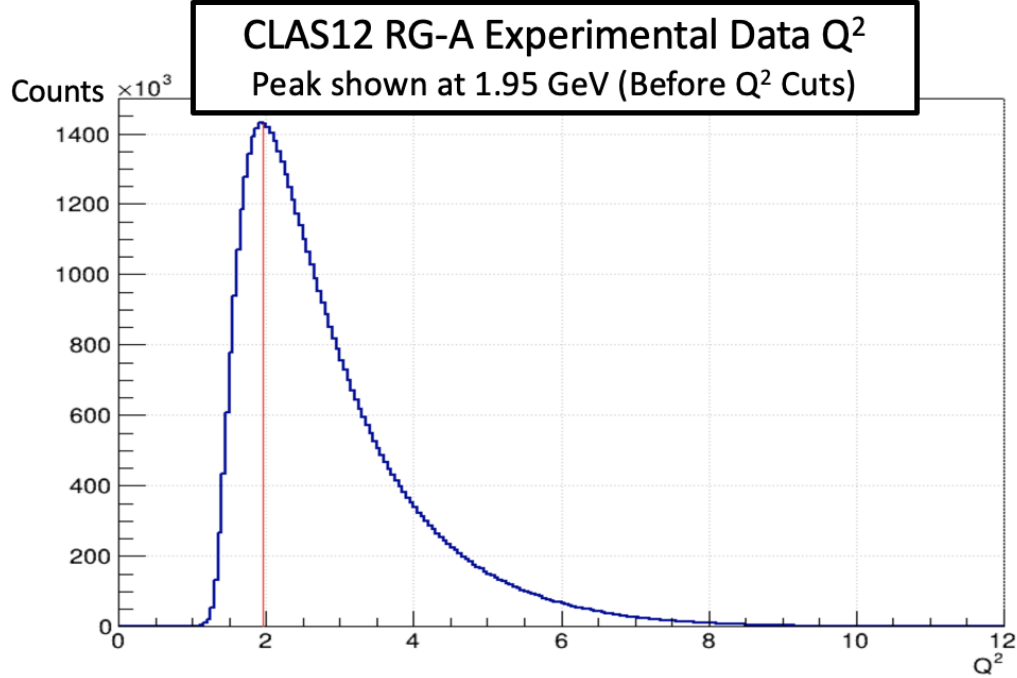


FIG. 3: Q^2 cut made after the peak (shown by the red line).

150

IV. DISTRIBUTIONS

151 The following histograms show the kinematic distributions of the particle momenta and the dis-
 152 tributions of Q^2 vs x_B and z vs P_T after all analysis cuts are applied. [Figure 6](#) and [Figure 7](#) show a
 153 comparison between the particle kinematics in the experimental data and the Monte Carlo files with
 154 the cuts described throughout the previous sections as well as those used to test and improve the
 155 Monte Carlo smearing functions (see [Description](#) for more details).

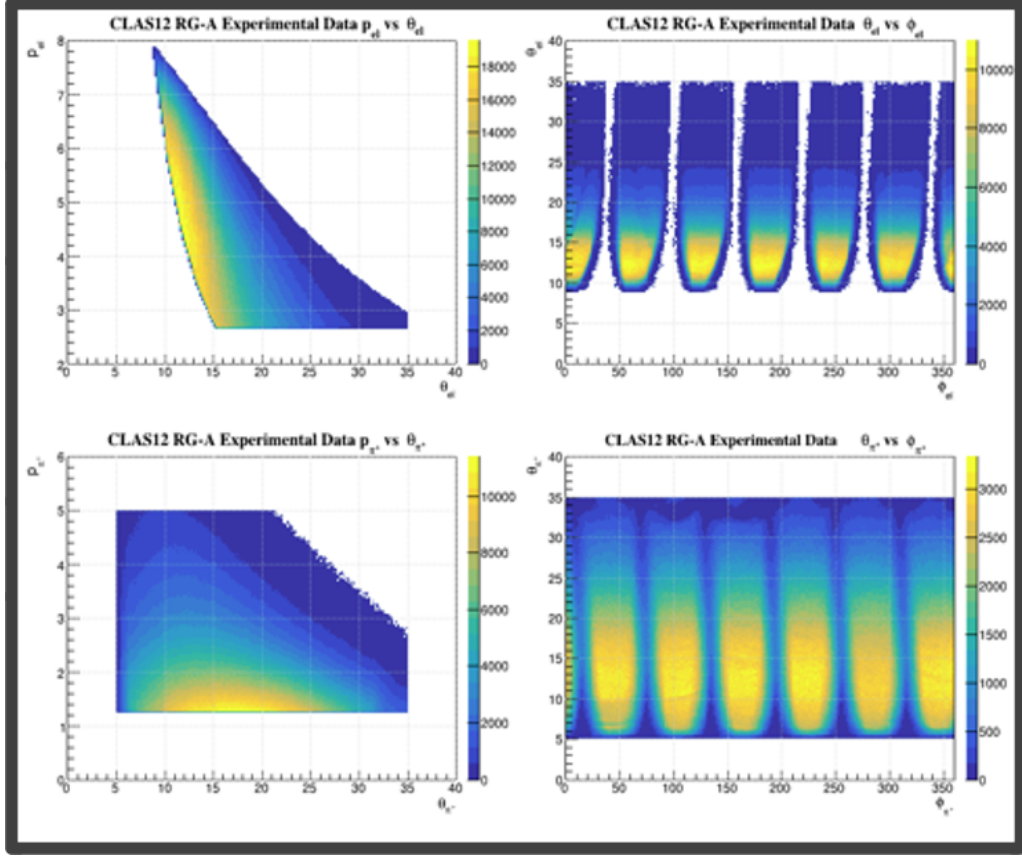


FIG. 4: Particle Kinematics after cuts. The histograms in the top row show the scattered electron kinematics while the bottom row shows the pion kinematics. The variables plotted are, in the first column, the particle's momentum vs its polar (θ) angle and, in the second column, that angle vs the azimuthal (ϕ) angle. Here, both angles are measured in the lab frame, so this ϕ angle does not share the same definition as the ϕ_h angle used elsewhere in this analysis.

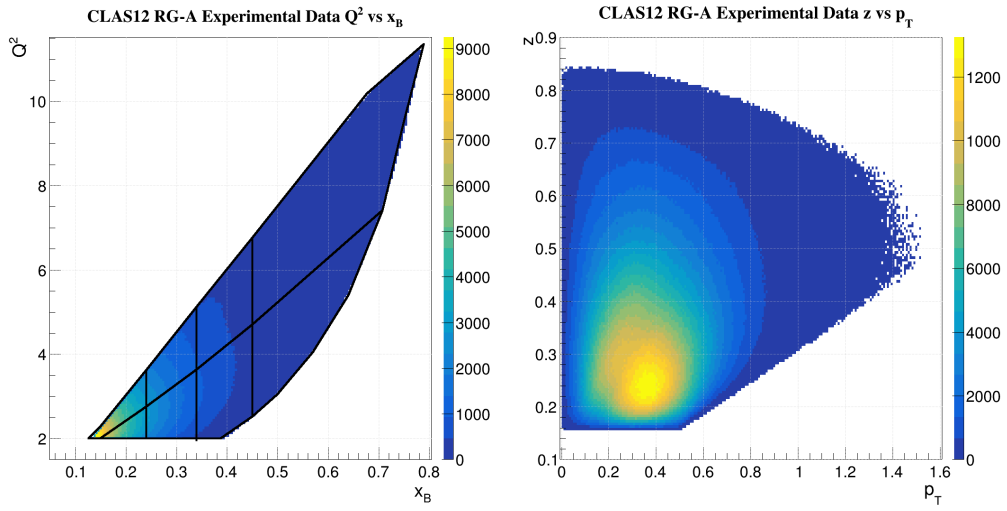


FIG. 5: 2D distributions of Q^2 , x_B , z , and P_T after all analysis cuts are applied to the RG-A data. The border lines drawn in the Q^2 vs x_B histogram define the binning schemes to be used in this analysis, which are described in more detail in the following section.

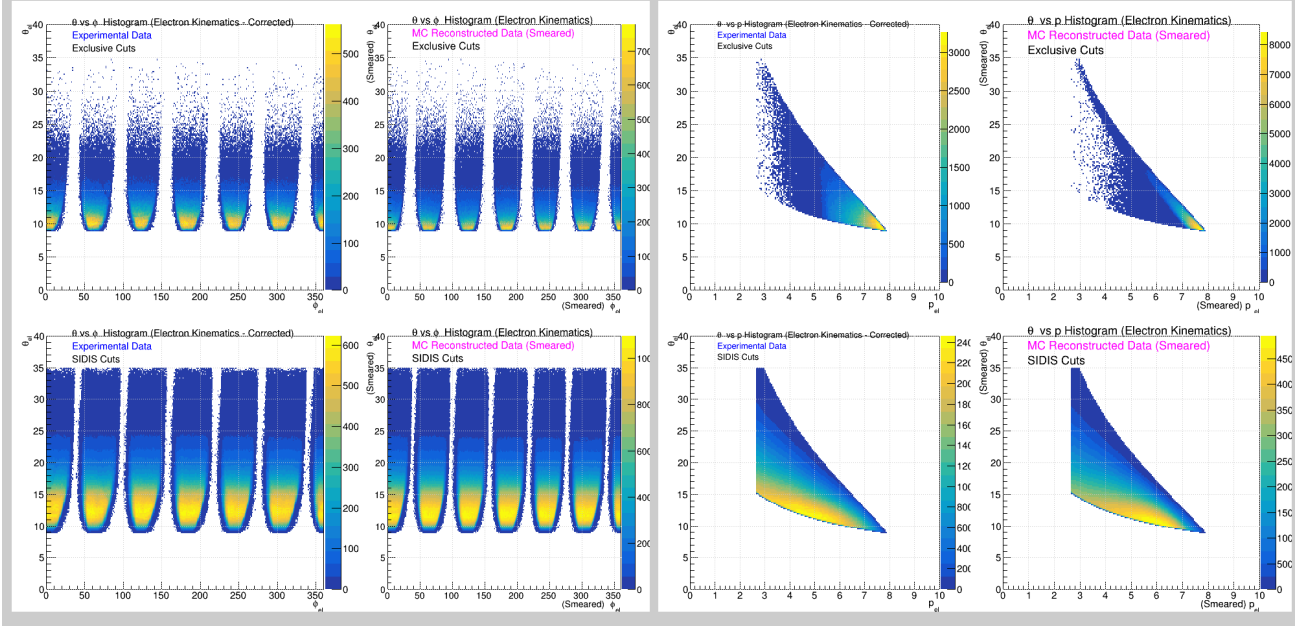


FIG. 6: **Electron** kinematic comparison between ‘SIDIS’ cuts and ‘Exclusive’ cuts. The plots on the top rows use the ‘Exclusive’ cuts made when obtaining the smearing factors used to improve the Monte Carlo while the bottom rows show the ‘SIDIS’ cuts used throughout the rest of the analysis.

The plots grouped on the left show θ vs ϕ while those on the right show θ vs p . The plots on the left within these groups (marked with a blue title) are made with the experimental data while the ones to their right come from the Reconstructed Monte Carlo files (marked with a pink title).

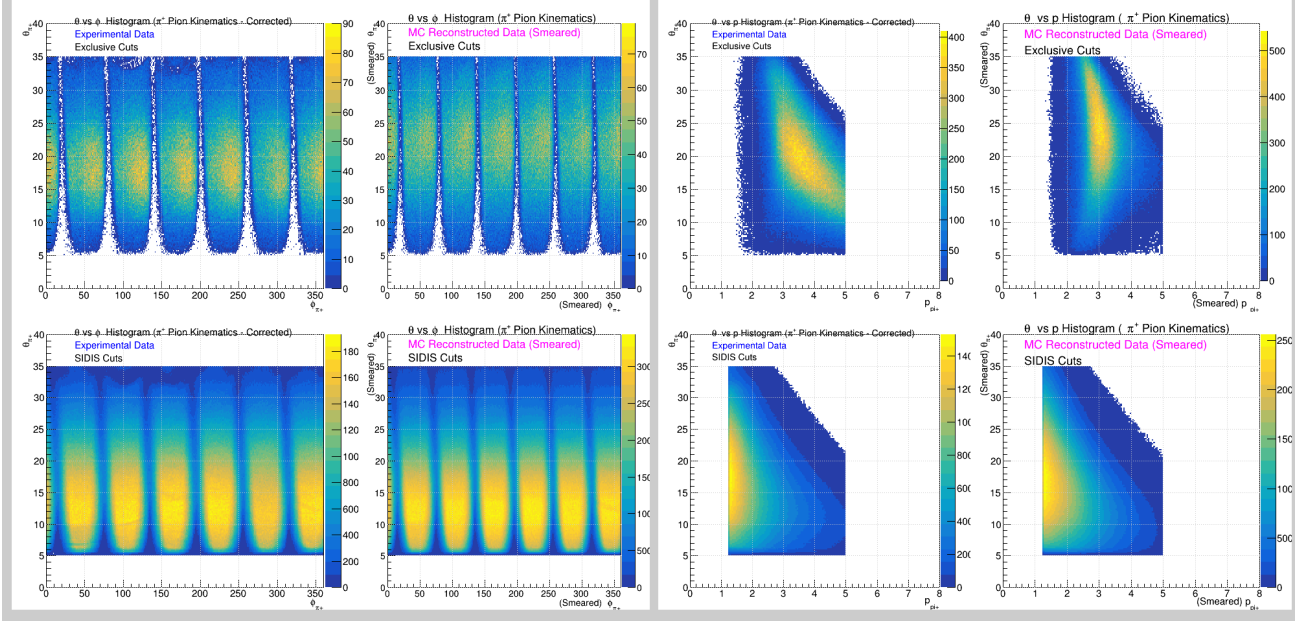


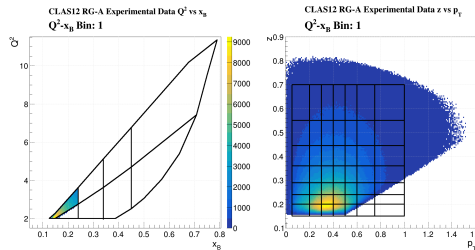
FIG. 7: π^+ **Pion** kinematic comparison between ‘SIDIS’ cuts and ‘Exclusive’ cuts. The plots on the top rows use the ‘Exclusive’ cuts made when obtaining the smearing factors used to improve the Monte Carlo while the bottom rows show the ‘SIDIS’ cuts used throughout the rest of the analysis.

The plots grouped on the left show θ vs ϕ while those on the right show θ vs p . The plots on the left within these groups (marked with a blue title) are made with the experimental data while the ones to their right come from the Reconstructed Monte Carlo files (marked with a pink title).

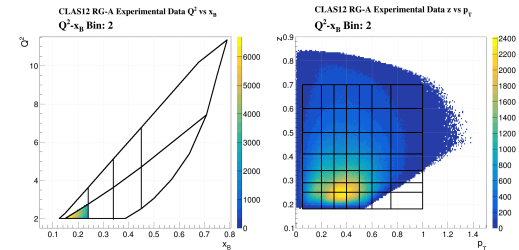
156

V. BINNING

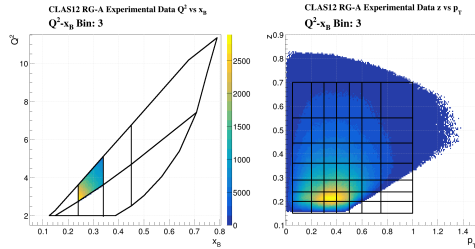
The kinematic binning used by this analysis consists of 8 Q^2 - x_B kinematic bins for which there exists anywhere between 4 to 7 bins of z and of P_T . Combined, this means that there can be anywhere from 20 to 49 z - P_T bins for any given Q^2 - x_B bins. These two-dimensional binning schemes are based on a prior multidimensional study of π^+ BSAs by S. Diehl [5], with modifications being made as a result of a larger cut on Q^2 . The change consists of merging what was previously considered Q^2 - x_B bins 1 and 3 (keeping bin 3's definitions of the z - P_T bins), and thus reducing the total number of these bins from 9 to 8. Depictions of each set of two-dimensional bin definitions are included below. ϕ_h is planned to use 36 bins for each of the other set of kinematic bins, with the size and number of these bins being independent of the other variables.



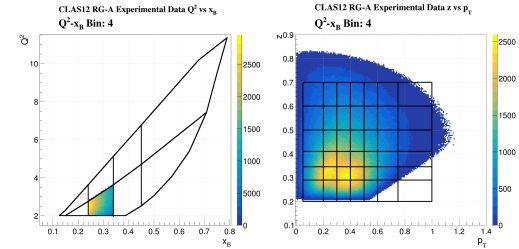
(a) 2D distributions of Q^2 , x_B , z , and P_T after all analysis cuts are applied to the RG-A data. Figure shows events in $Q^2 \cdot x_B$ bin 1.



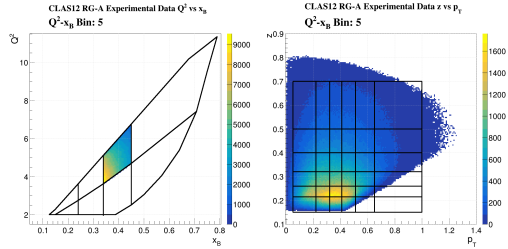
(b) 2D distributions of Q^2 , x_B , z , and P_T after all analysis cuts are applied to the RG-A data. Figure shows events in $Q^2 \cdot x_B$ bin 2.



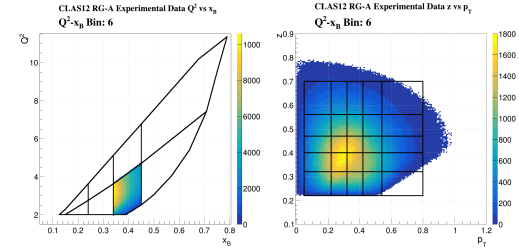
(c) 2D distributions of Q^2 , x_B , z , and P_T after all analysis cuts are applied to the RG-A data. Figure shows events in $Q^2 \cdot x_B$ bin 3.



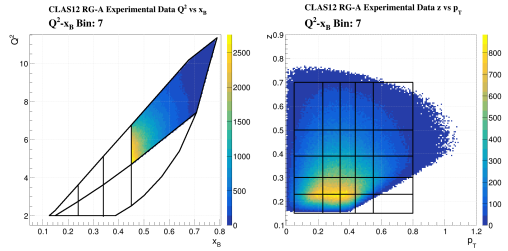
(d) 2D distributions of Q^2 , x_B , z , and P_T after all analysis cuts are applied to the RG-A data. Figure shows events in $Q^2 \cdot x_B$ bin 4.



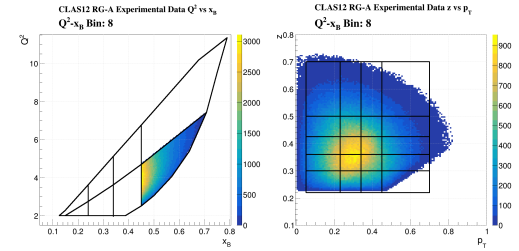
(e) 2D distributions of Q^2 , x_B , z , and P_T after all analysis cuts are applied to the RG-A data. Figure shows events in $Q^2 \cdot x_B$ bin 5.



(f) 2D distributions of Q^2 , x_B , z , and P_T after all analysis cuts are applied to the RG-A data. Figure shows events in $Q^2 \cdot x_B$ bin 6.



(g) 2D distributions of Q^2 , x_B , z , and P_T after all analysis cuts are applied to the RG-A data. Figure shows events in $Q^2 \cdot x_B$ bin 7.



(h) 2D distributions of Q^2 , x_B , z , and P_T after all analysis cuts are applied to the RG-A data. Figure shows events in $Q^2 \cdot x_B$ bin 8.

166

VI. MONTE CARLO

167

A. Description

168 The CLAS12 Fall 2018 RG-A experimental configuration has been described in detail in GEMC [7],
 169 a GEANT4 based simulation package that offers the possibility to easily implement detectors in a full
 170 GEANT simulation. The position of the detectors in Hall B have been matched to survey data and a
 171 realistic map of the magnetic field has been generated to accurately reproduce the experimental set
 172 up. LUND generators were used to produce realistic final states that were read by GEMC version
 173 4.3.2 and passed through the the detector system of CLAS12. The results of this process were cooked
 174 with COATJAVA version 6.5.3 and the reconstructed banks were added to the original generated
 175 banks for comparison. The generator used for SIDIS Monte Carlo analysis is clasdis [8] which is based
 176 on the PEPSI generator [9, 10], the polarized version of the well-known LEPTO generator [11].

177 In order to better mimic realistic resolution effects, a smearing function is also applied to the
 178 reconstructed Monte Carlo data. An original particle-independent function was first developed by
 179 F.X. Girod, but was later modified to smear the momentum of the measured electrons and pions
 180 separately. These modifications were made by using exclusive reactions within the data samples
 181 to match the widths of the ΔP distributions in both the experimental data and Monte Carlo files.
 182 Similar cuts as those previously described were still applied to obtain this sample of the data, with
 183 the exception of the Missing Mass cuts which were removed.³ The modifications to the smearing
 184 functions were made in an iterative process following a similar procedure that produced the exclusive
 185 momentum corrections. However, here the correction factor used to bring the Monte Carlo into
 186 agreement with the experimental data was the ratio of the widths of the ΔP distributions whereas
 187 the momentum corrections just relied on the peak positions of the experimental plots. Details about
 188 the smearing functions used to in this analysis set are included in the [Appendix](#) while [Figures 9-12](#)
 189 show the effects of using F.X. Girod's particle-independent smearing function and [Figures 13-16](#) show
 190 the particle-dependent version developed for this analysis.⁴

³ For the exclusive reactions, a Missing Mass cut is instead applied within the region of the Neutron mass peak which was the same as the ones used to develop the experimental momentum corrections mentioned in the [Data Set](#) section of this note. See [Distributions](#) for more details regarding this comparison.

⁴ Data smearing is applied before the analysis cuts but does not effect the particle matching detailed in [MC Event Matching](#).

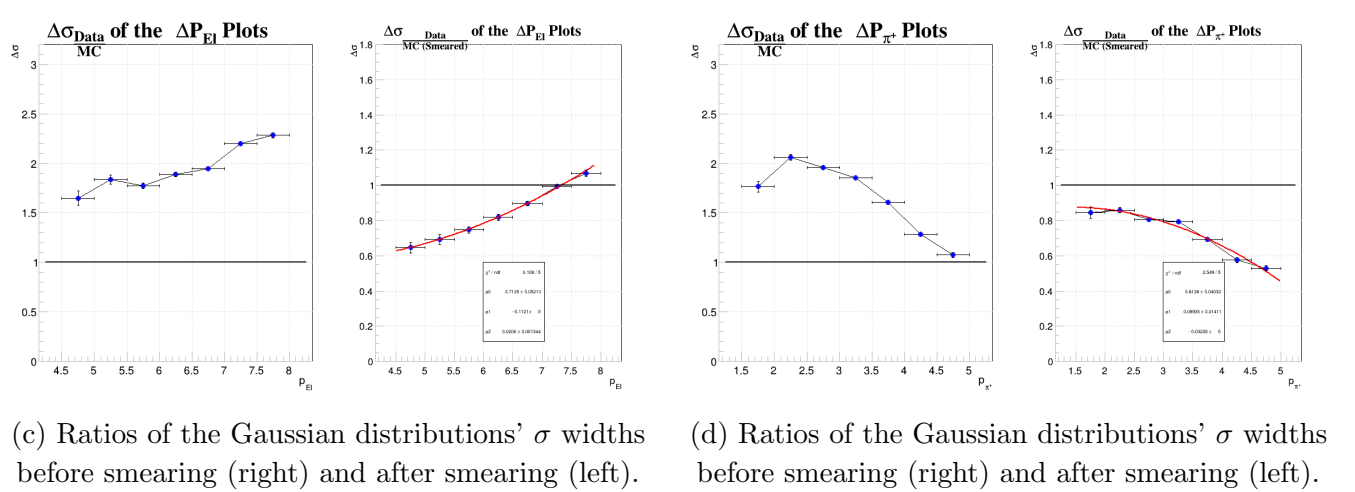
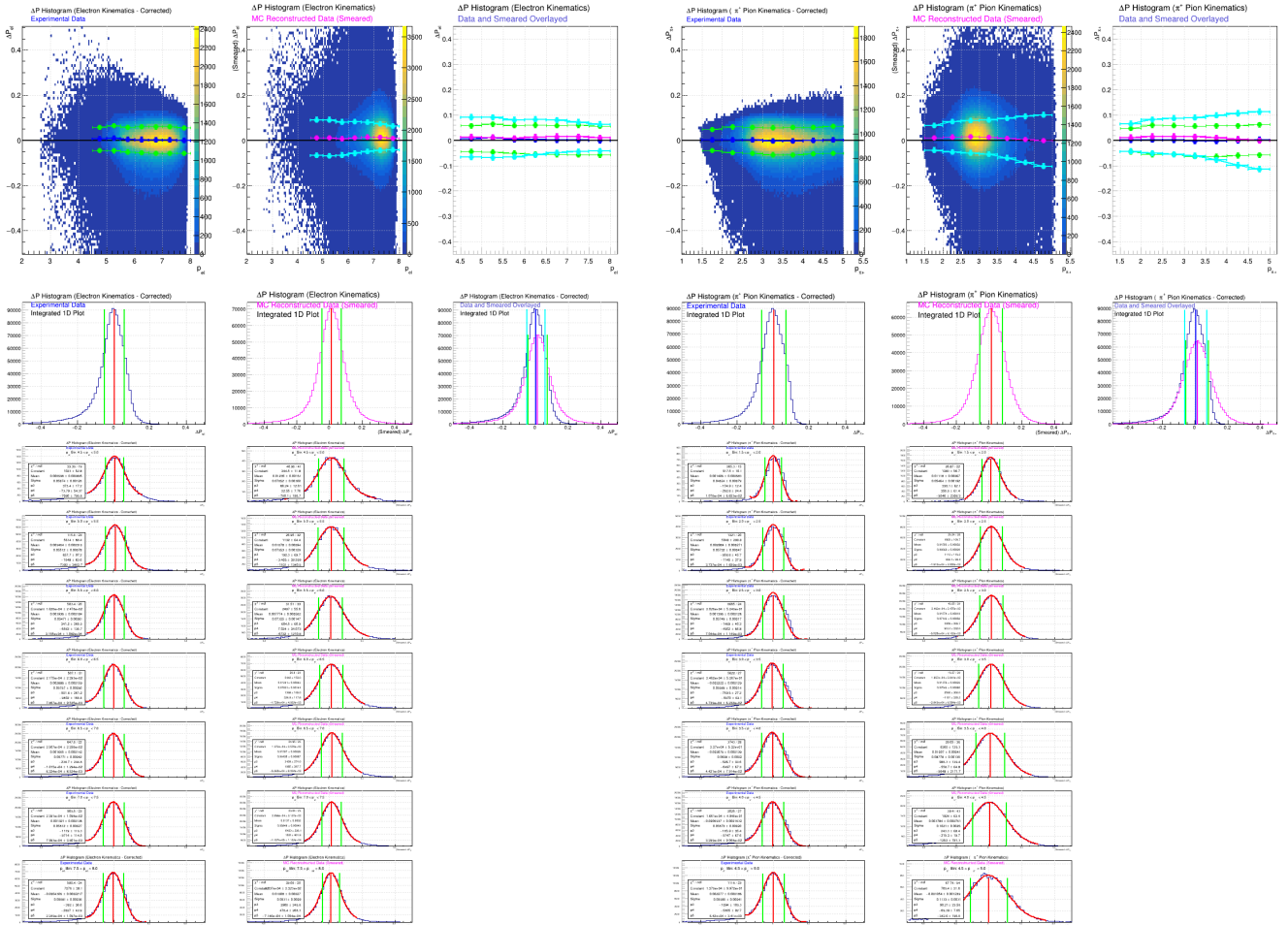
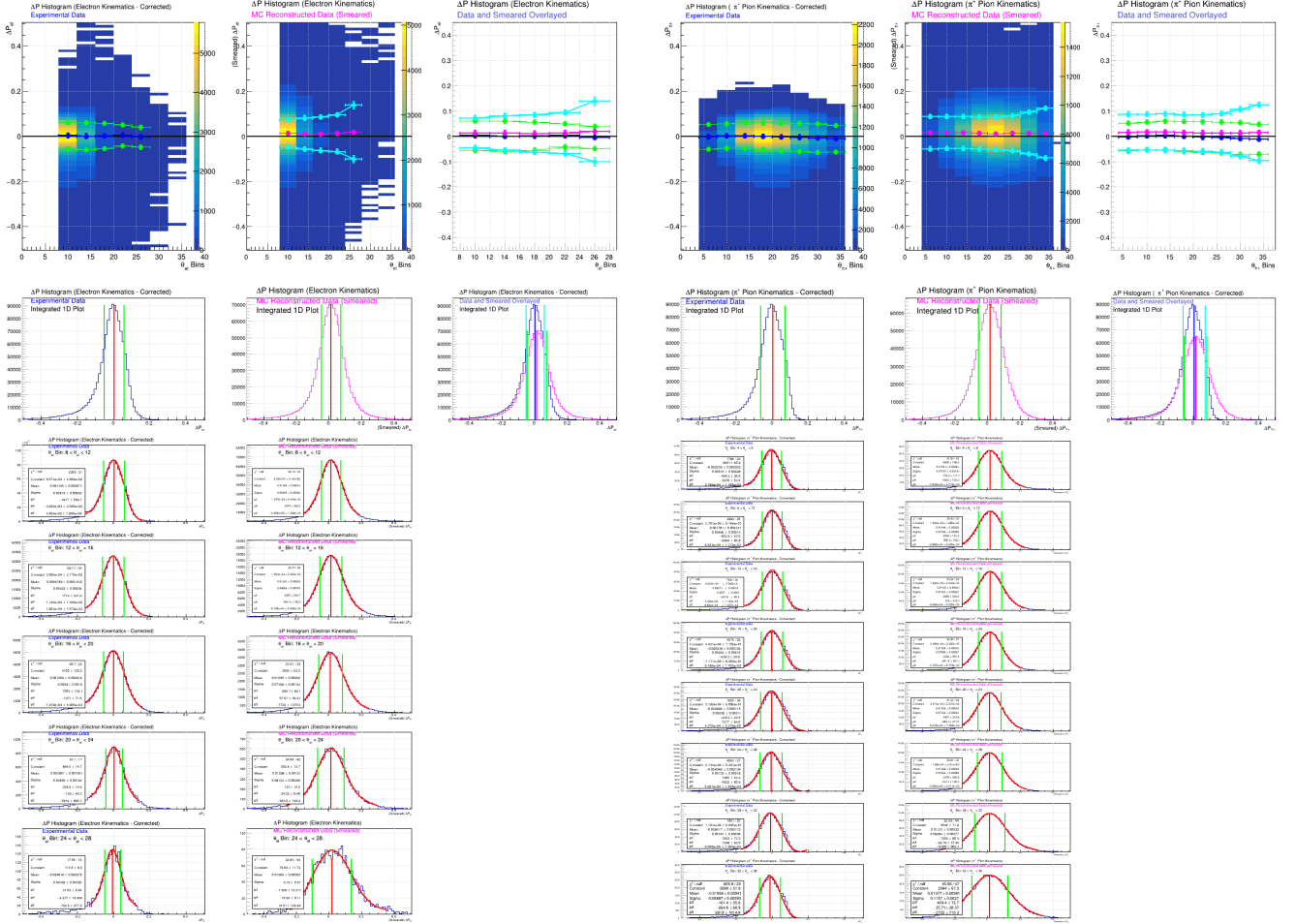
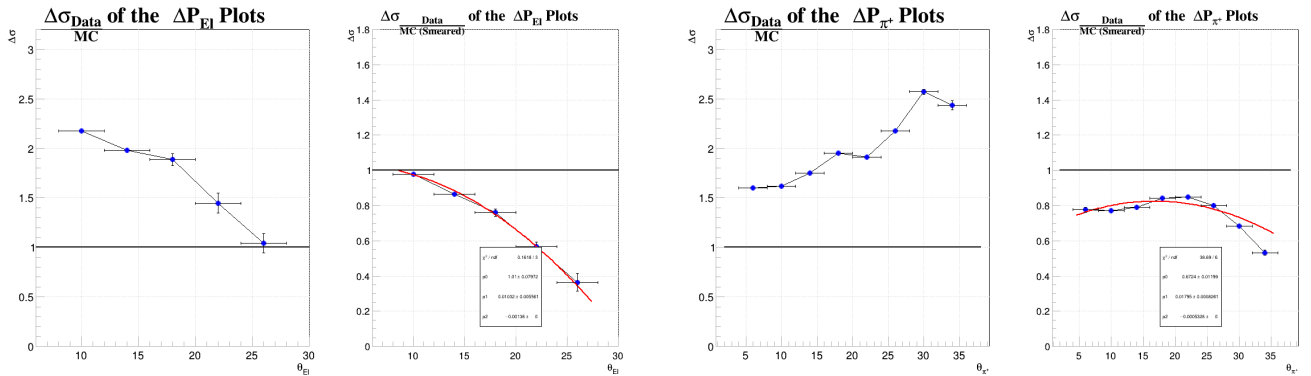


FIG. 9: ΔP vs. p plots for Electron (right) and π^+ Pion (left) Kinematics. Using F.X. Girod's version of the smearing function.

For Figures (a) and (b), the left-most plots show the experimental resolutions, the middle plots show the smeared Monte Carlo resolutions, and the right-most plots show them overlapped. For Figures (c) and (d), the quadratic fits shown are used to develop additional iterations of the smearing functions.



(a) Sliced fits of the correction parameters (Electron). (b) Sliced fits of the correction parameters (π^+ Pion).

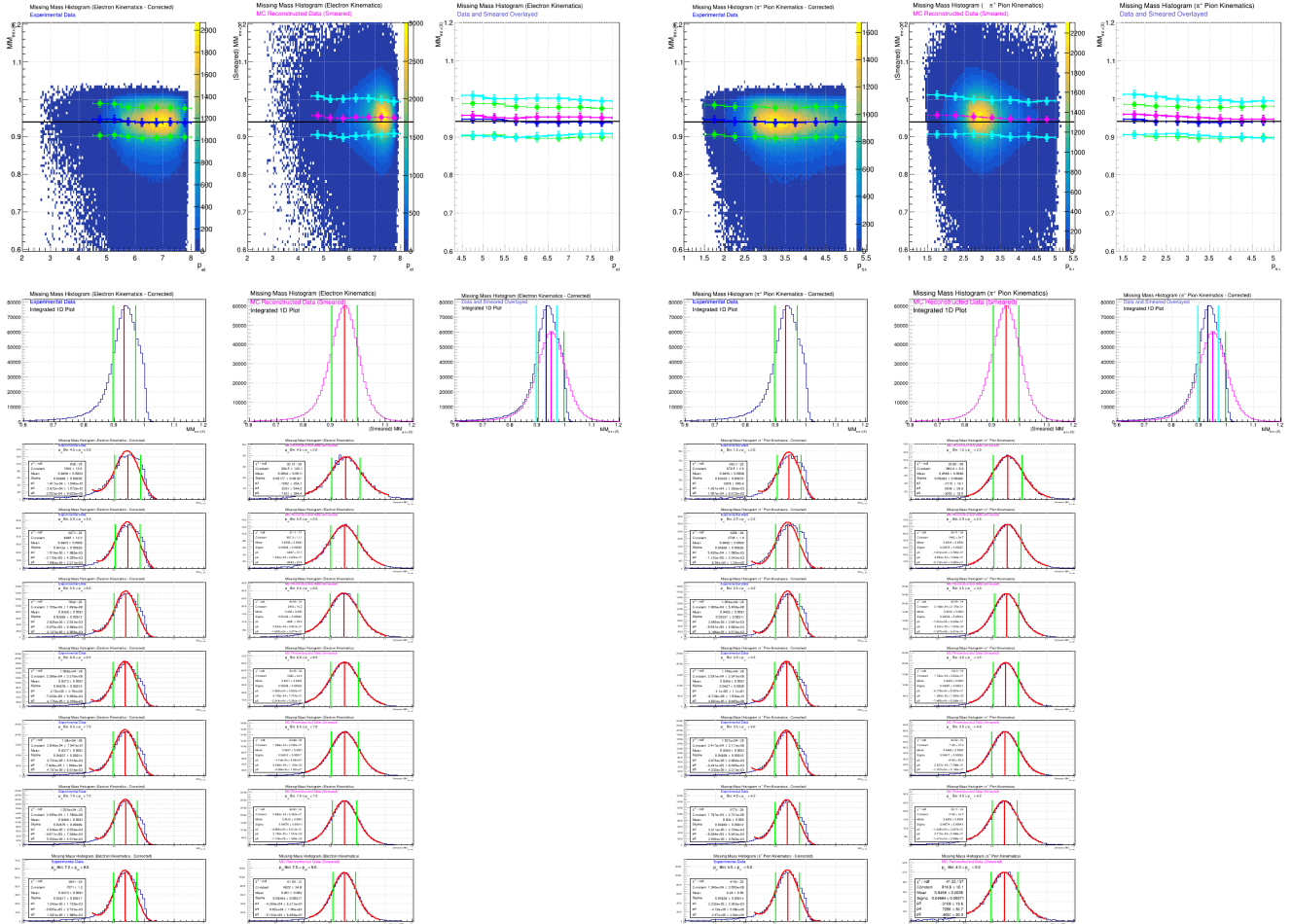
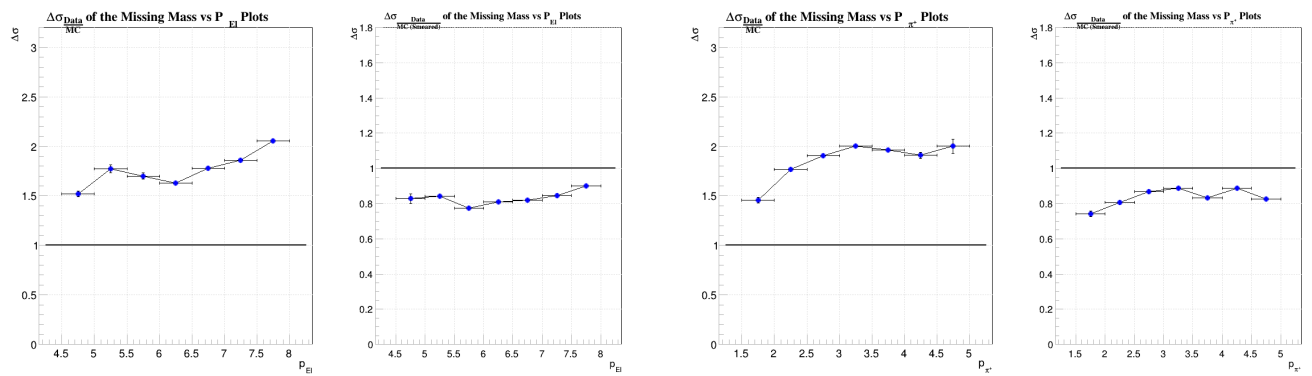


(c) Ratios of the Gaussian distributions' σ widths before smearing (right) and after smearing (left).

(d) Ratios of the Gaussian distributions' σ widths before smearing (right) and after smearing (left).

FIG. 10: ΔP vs. θ plots for Electron (right) and π^+ Pion (left) Kinematics. Using F.X. Girod's version of the smearing function.

For Figures (a) and (b), the left-most plots show the experimental resolutions, the middle plots show the smeared Monte Carlo resolutions, and the right-most plots show them overlapped. For Figures (c) and (d), the quadratic fits shown are used to develop additional iterations of the smearing functions.

(a) Sliced fits of the correction parameters (Electron).(b) Sliced fits of the correction parameters (π^+ Pion).(c) Ratios of the Gaussian distributions' σ widths before smearing (right) and after smearing (left).(d) Ratios of the Gaussian distributions' σ widths before smearing (right) and after smearing (left).FIG. 11: Missing Mass vs. p plots for Electron (right) and π^+ Pion (left) Kinematics. Using F.X. Girod's version of the smearing function.

For Figures (a) and (b), the left-most plots show the experimental resolutions, the middle plots show the smeared Monte Carlo resolutions, and the right-most plots show them overlapped.

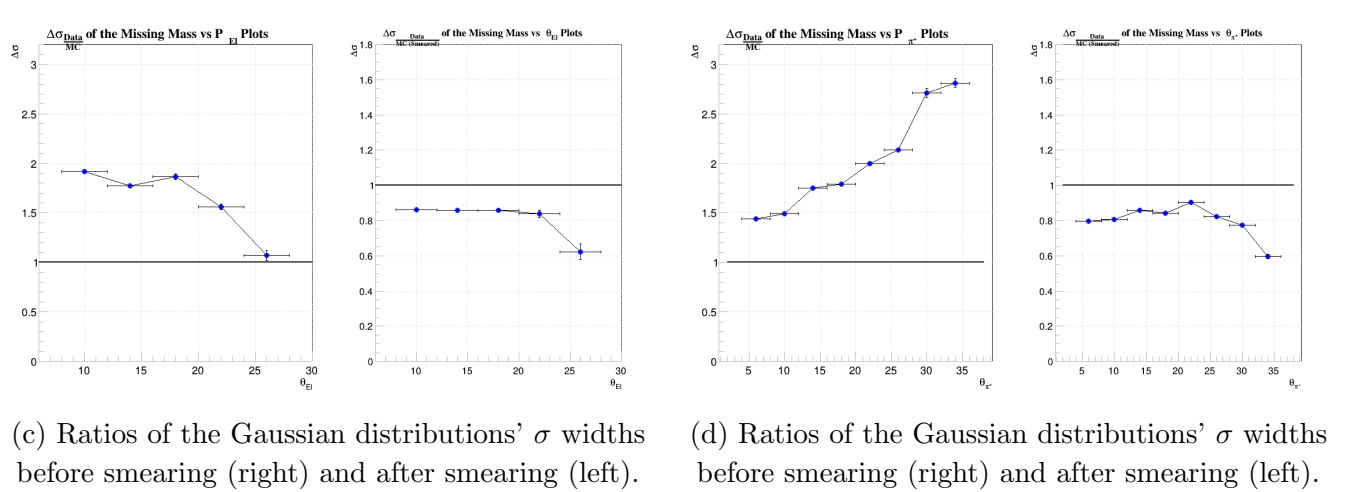
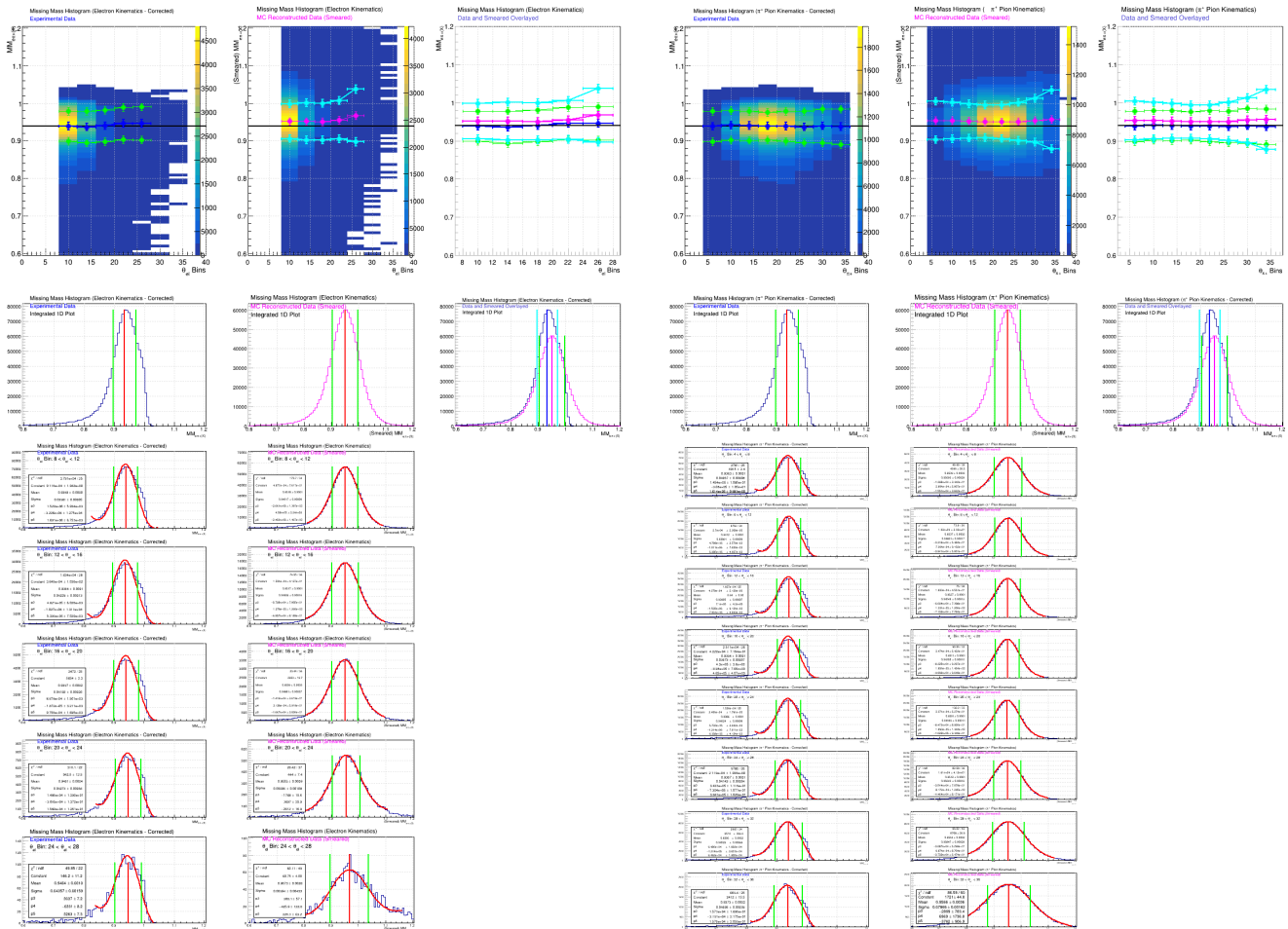


FIG. 12: Missing Mass vs. θ plots for Electron (right) and π^+ Pion (left) Kinematics. Using F.X. Girod's version of the smearing function.

For Figures (a) and (b), the left-most plots show the experimental resolutions, the middle plots show the smeared Monte Carlo resolutions, and the right-most plots show them overlapped.

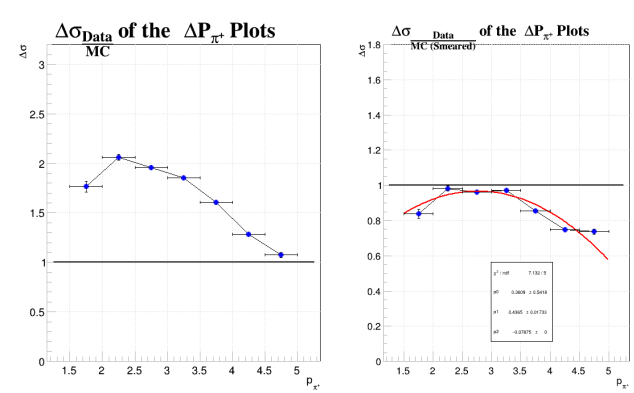
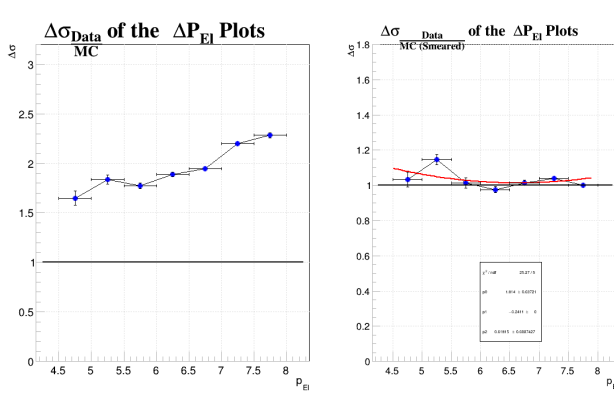
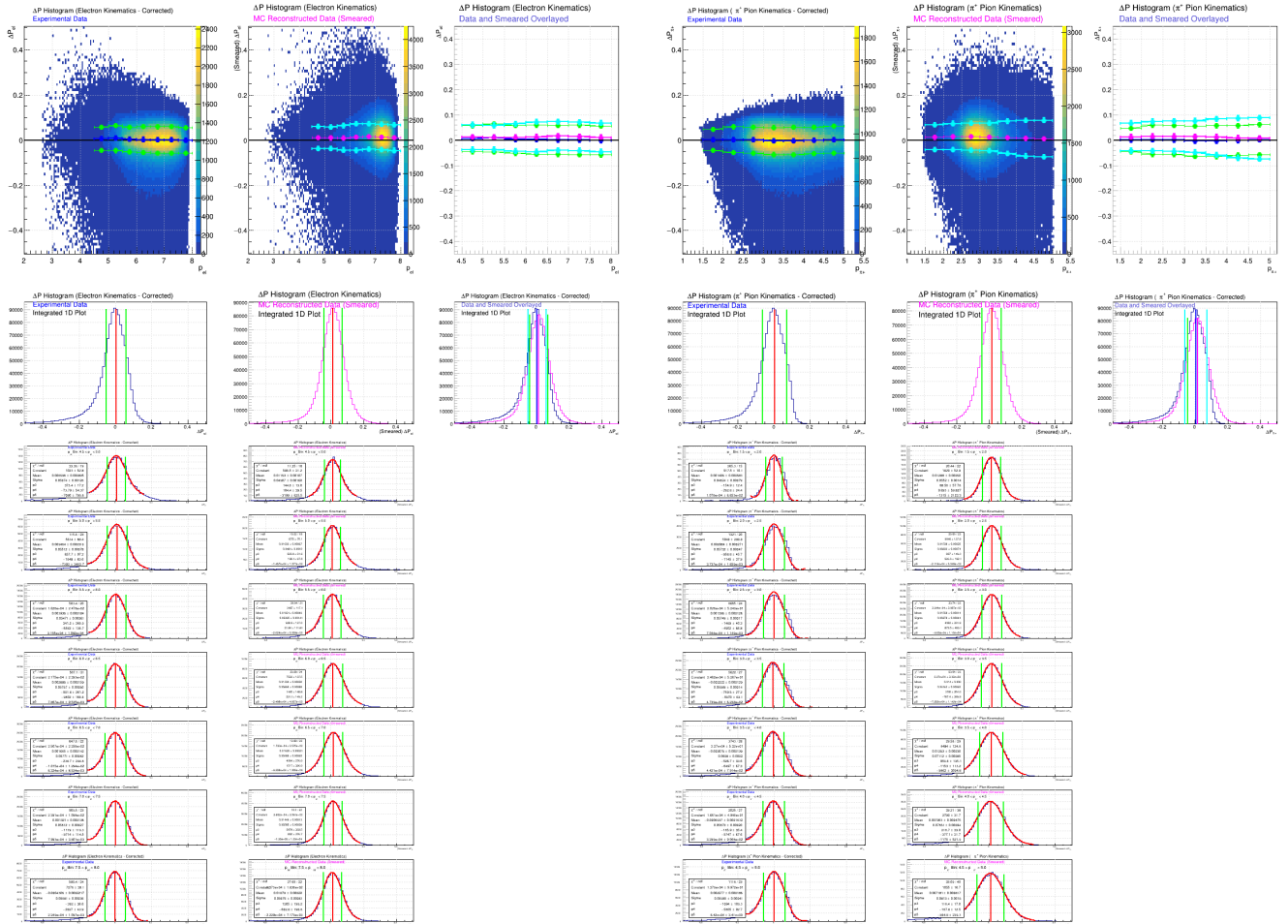
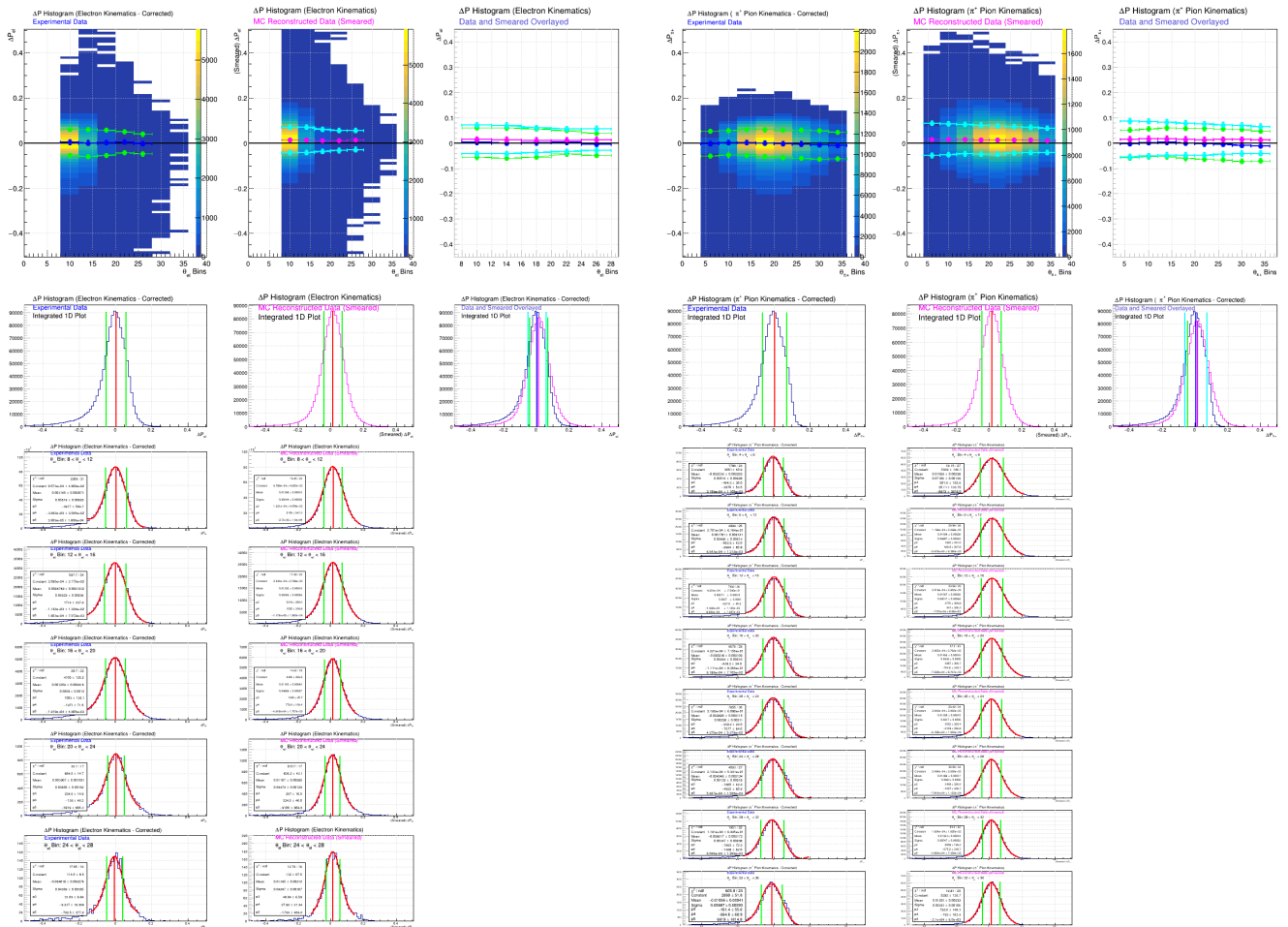
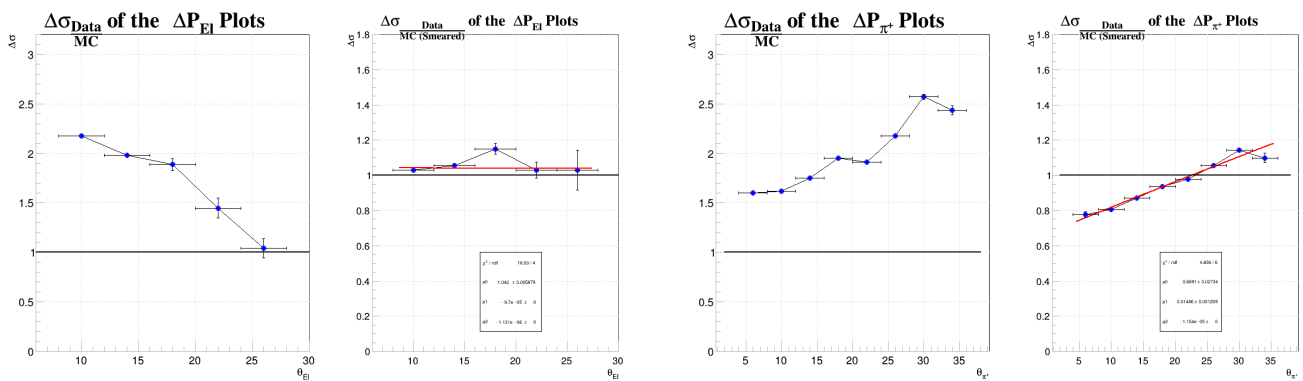


FIG. 13: ΔP vs. p plots for Electron (right) and π^+ Pion (left) Kinematics. Using Modified version of the smearing function.

For Figures (a) and (b), the left-most plots show the experimental resolutions, the middle plots show the smeared Monte Carlo resolutions, and the right-most plots show them overlapped. For Figures (c) and (d), the quadratic fits shown are used to develop additional iterations of the smearing functions.



(a) Sliced fits of the correction parameters (Electron).(b) Sliced fits of the correction parameters (π^+ Pion).

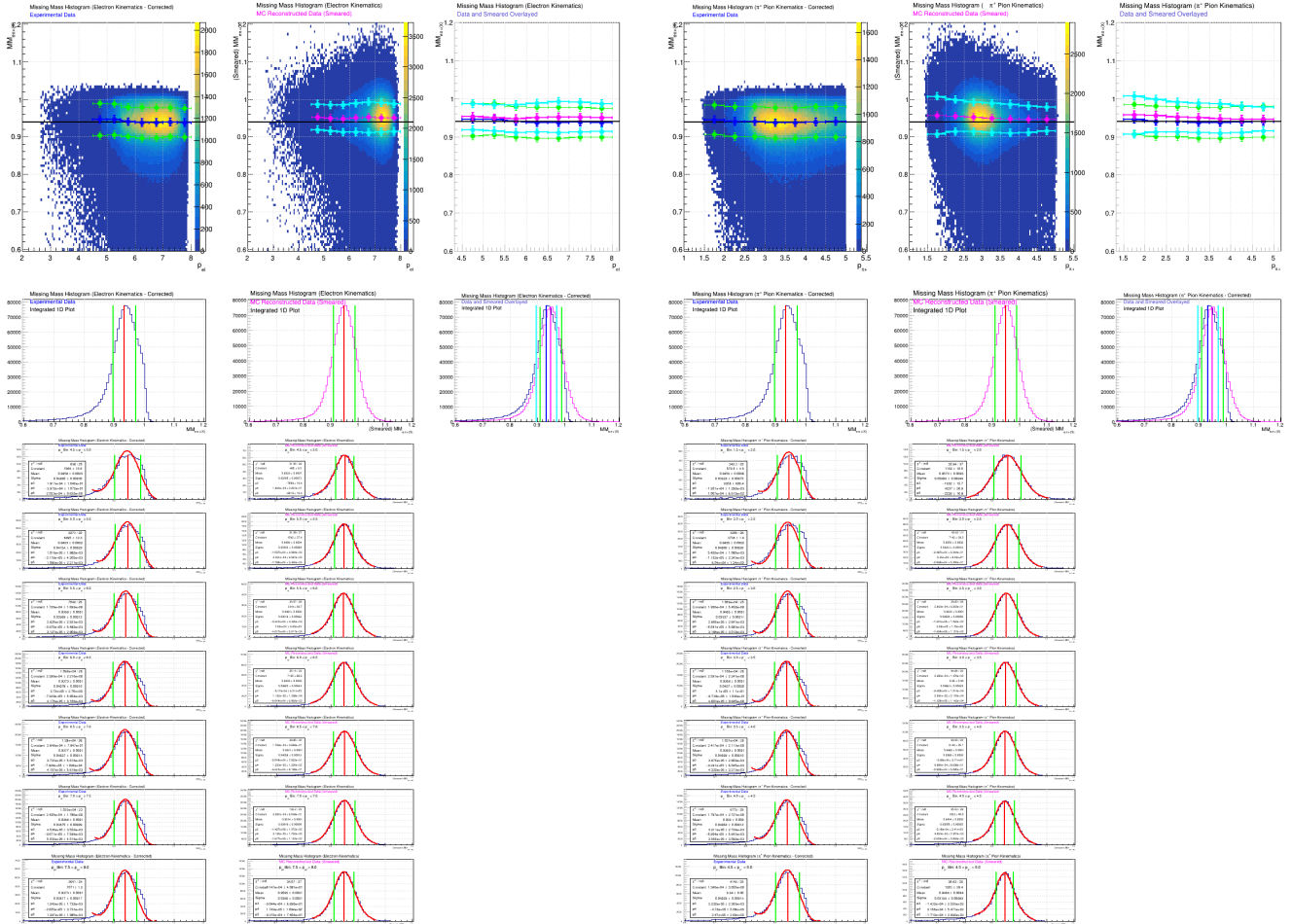


(c) Ratios of the Gaussian distributions' σ widths before smearing (right) and after smearing (left).

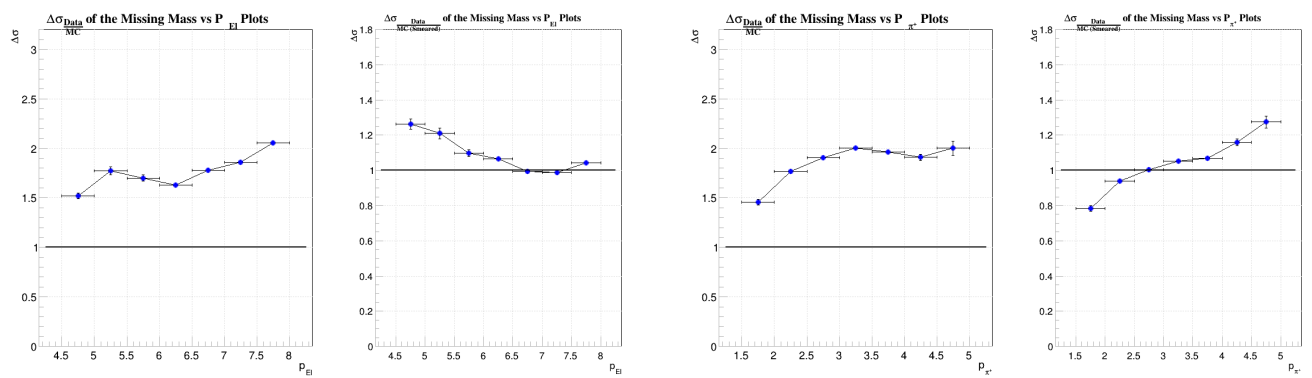
(d) Ratios of the Gaussian distributions' σ widths before smearing (right) and after smearing (left).

FIG. 14: ΔP vs. θ plots for Electron (right) and π^+ Pion (left) Kinematics.
Using the Modified version of the smearing function.

For Figures (a) and (b), the left-most plots show the experimental resolutions, the middle plots show the smeared Monte Carlo resolutions, and the right-most plots show them overlapped. For Figures (c) and (d), the quadratic fits shown are used to develop additional iterations of the smearing functions.



(a) Sliced fits of the correction parameters (Electron).(b) Sliced fits of the correction parameters (π^+ Pion).



(c) Ratios of the Gaussian distributions' σ widths before smearing (right) and after smearing (left).

(d) Ratios of the Gaussian distributions' σ widths before smearing (right) and after smearing (left).

FIG. 15: Missing Mass vs. p plots for Electron (right) and π^+ Pion (left) Kinematics. Using Modified version of the smearing function.

For Figures (a) and (b), the left-most plots show the experimental resolutions, the middle plots show the smeared Monte Carlo resolutions, and the right-most plots show them overlapped.

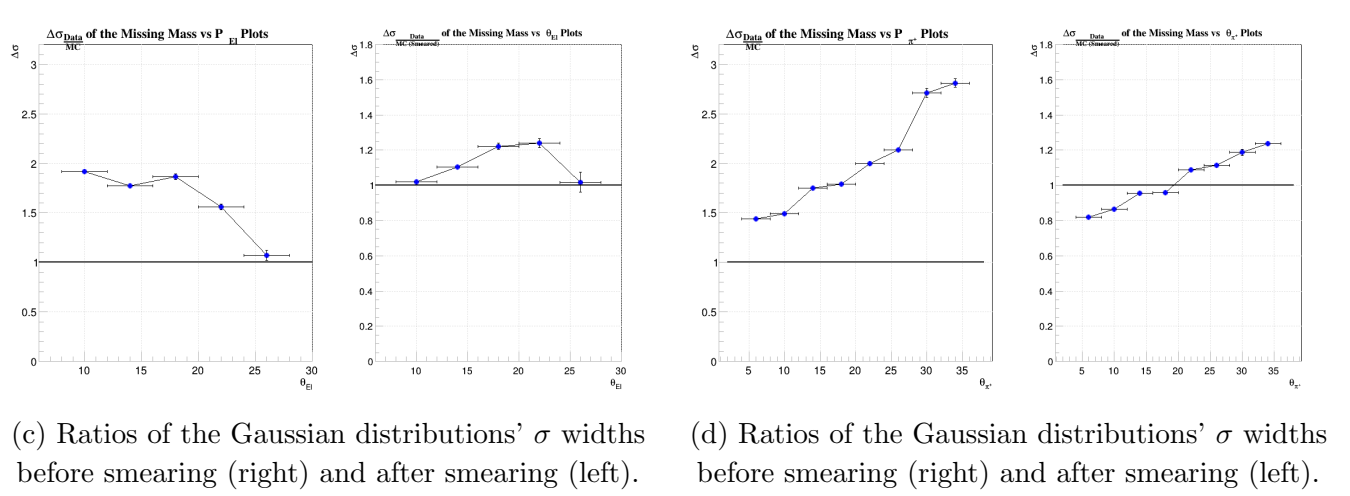
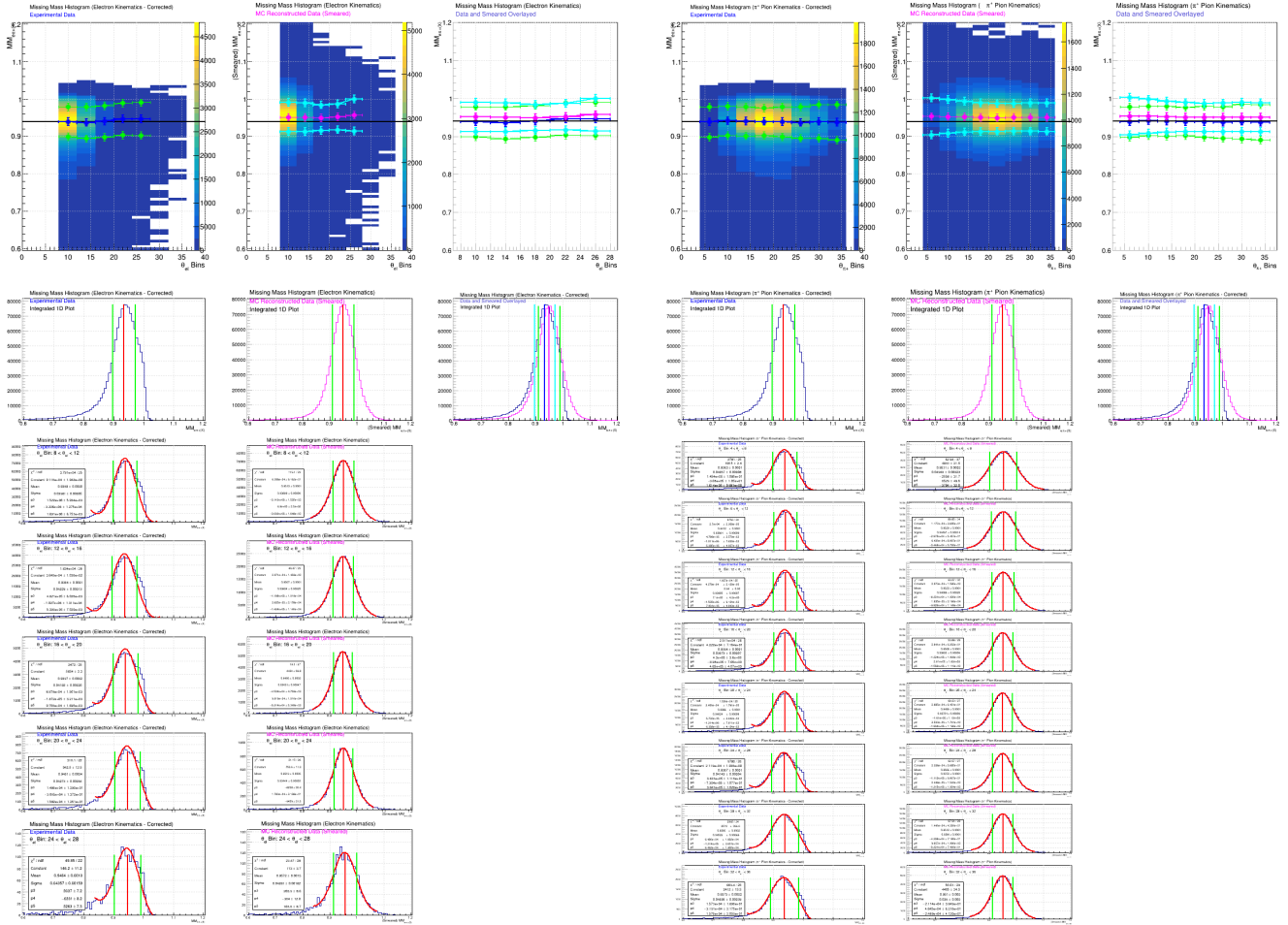


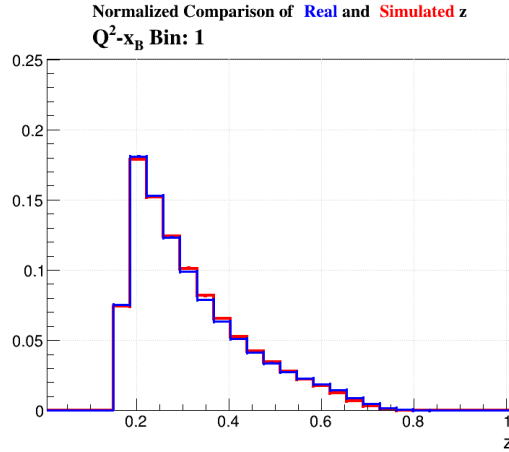
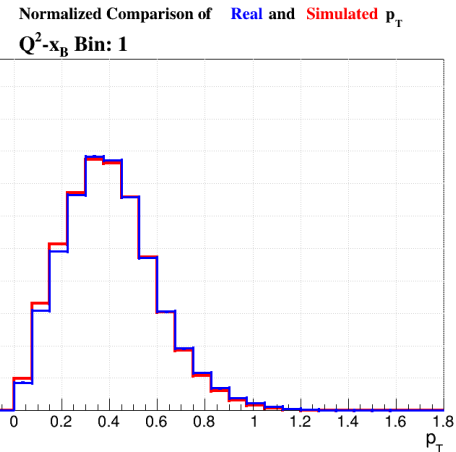
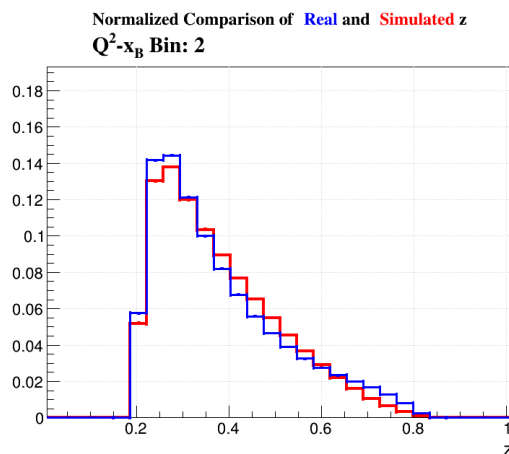
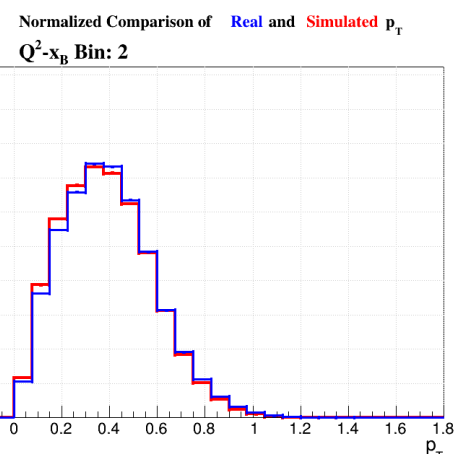
FIG. 16: Missing Mass vs. θ plots for Electron (right) and π^+ Pion (left) Kinematics. Using Modified version of the smearing function.

For Figures (a) and (b), the left-most plots show the experimental resolutions, the middle plots show the smeared Monte Carlo resolutions, and the right-most plots show them overlapped.

191

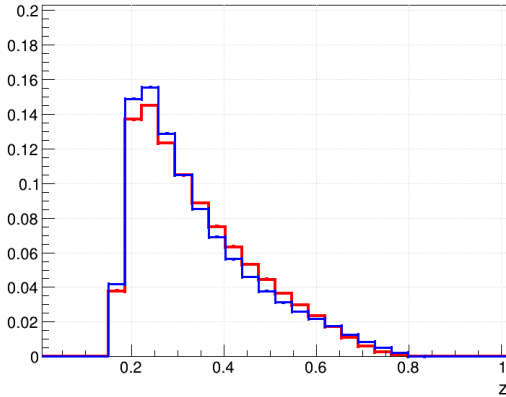
B. Data vs MC Comparison

192 The following images show the normalized comparisons between the Reconstructed (in red) Monte
 193 Carlo data and the Real Experimental data (in blue). The distributions shown will be of Q^2 , x_B , z ,
 194 P_T , and ϕ_h ⁵. Comparisons of z and P_T are also shown for each of the Q^2-x_B bins.

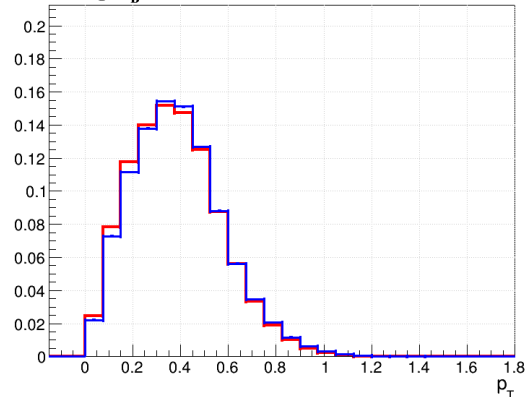
(a) Normalized Comparison of z for Q^2-x_B Bin 1(b) Normalized Comparison of p_T for Q^2-x_B Bin 1(a) Normalized Comparison of z for Q^2-x_B Bin 2(b) Normalized Comparison of p_T for Q^2-x_B Bin 2

⁵ The ϕ_h distribution is not expected to be ideal as the Monte Carlo simulation was initialized with a flat distribution. Future aspects of this analysis will use the measurements of the azimuthal modulations mentioned in the [Introduction](#) to reiterate the Monte Carlo simulation for progressively more realistic results.

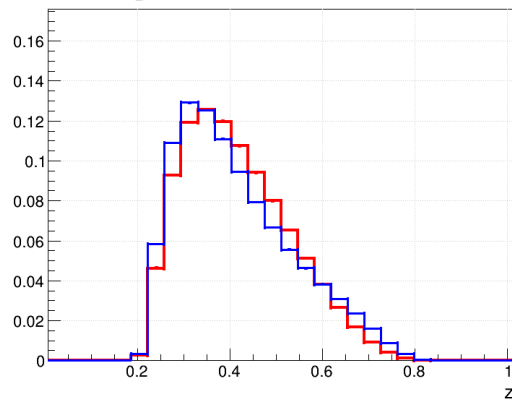
Normalized Comparison of Real and Simulated z
 Q^2-x_B Bin: 3

(a) Normalized Comparison of z for Q^2-x_B Bin 3

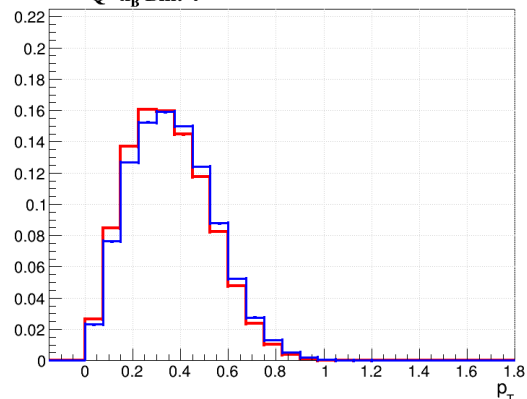
Normalized Comparison of Real and Simulated p_T
 Q^2-x_B Bin: 3

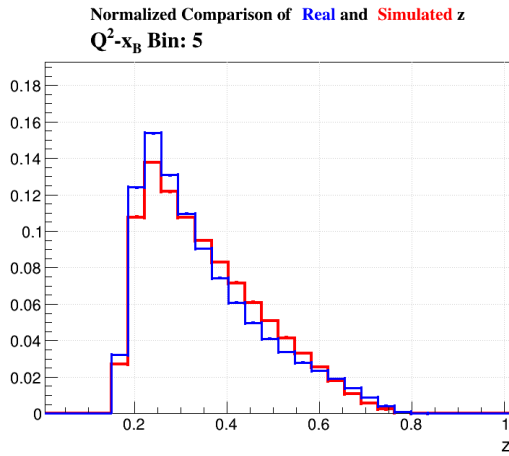
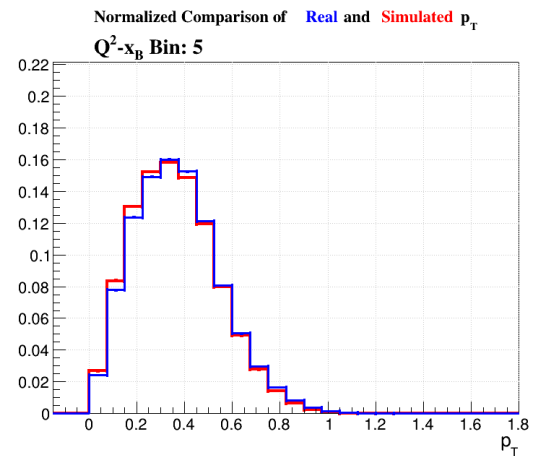
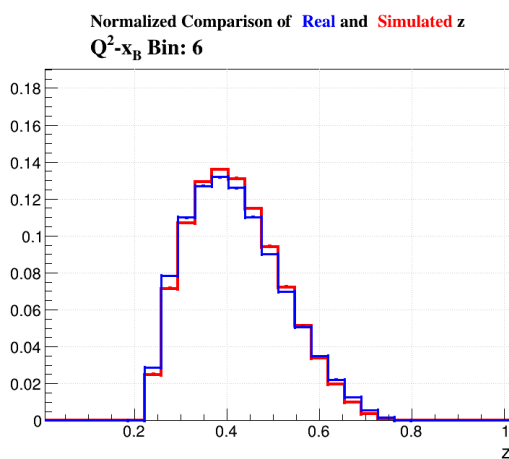
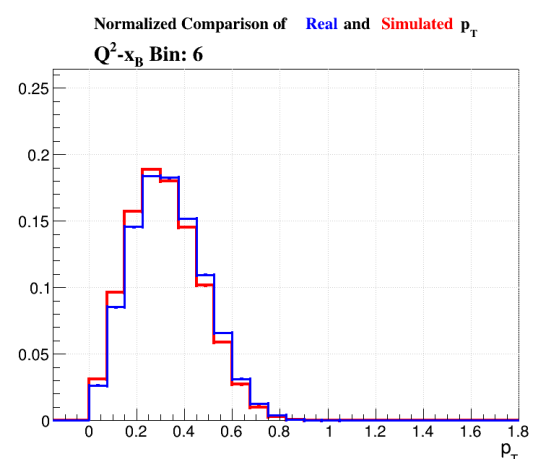
(b) Normalized Comparison of p_T for Q^2-x_B Bin 3

Normalized Comparison of Real and Simulated z
 Q^2-x_B Bin: 4

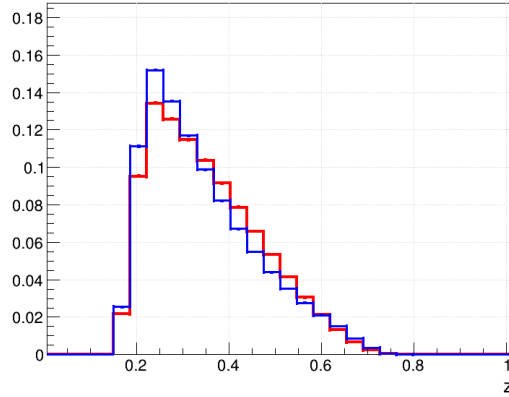
(a) Normalized Comparison of z for Q^2-x_B Bin 4

Normalized Comparison of Real and Simulated p_T
 Q^2-x_B Bin: 4

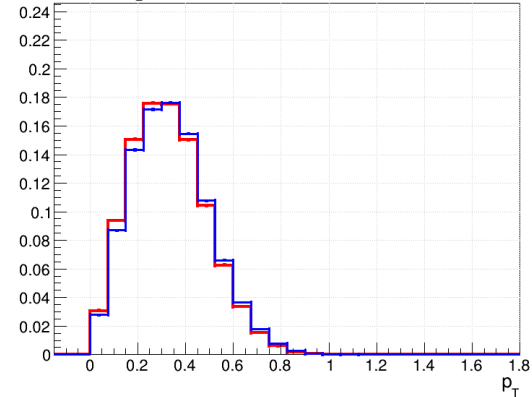
(b) Normalized Comparison of p_T for Q^2-x_B Bin 4

(a) Normalized Comparison of z for Q^2-x_B Bin 5(b) Normalized Comparison of p_T for Q^2-x_B Bin 5(a) Normalized Comparison of z for Q^2-x_B Bin 6(b) Normalized Comparison of p_T for Q^2-x_B Bin 6

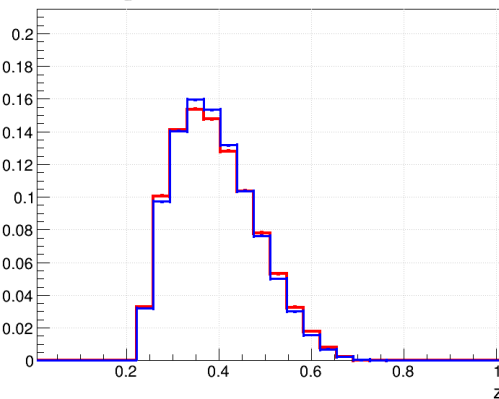
Normalized Comparison of Real and Simulated z
 Q^2-x_B Bin: 7

(a) Normalized Comparison of z for Q^2-x_B Bin 7

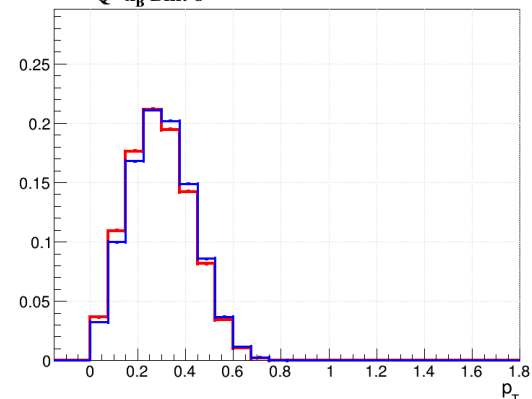
Normalized Comparison of Real and Simulated p_T
 Q^2-x_B Bin: 7

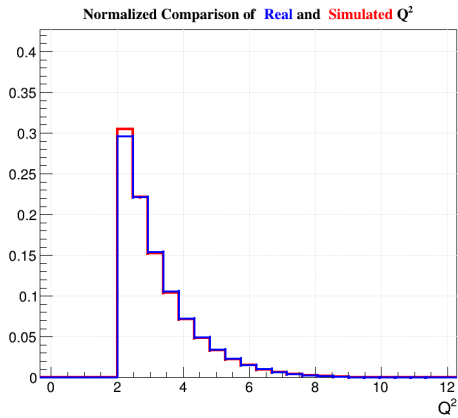
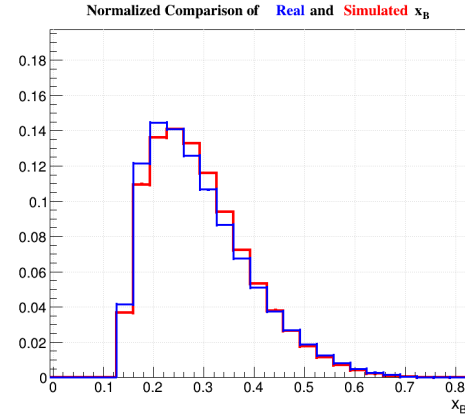
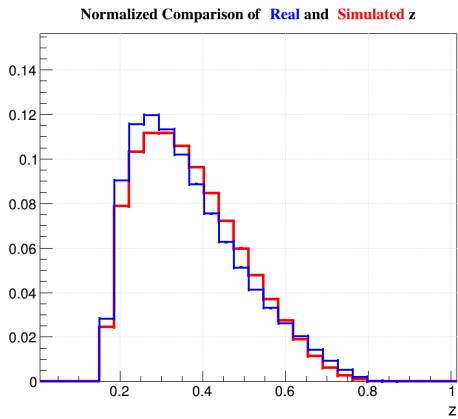
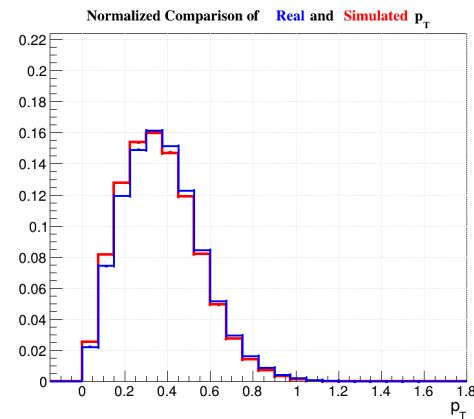
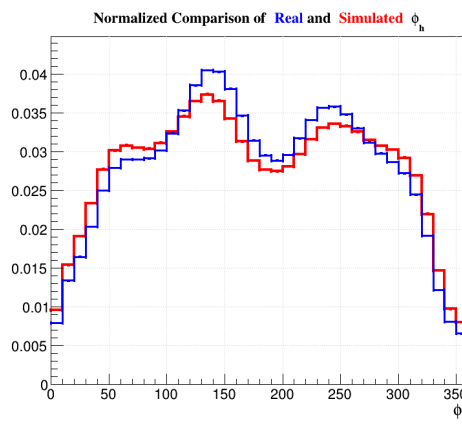
(b) Normalized Comparison of p_T for Q^2-x_B Bin 7

Normalized Comparison of Real and Simulated z
 Q^2-x_B Bin: 8

(a) Normalized Comparison of z for Q^2-x_B Bin 8

Normalized Comparison of Real and Simulated p_T
 Q^2-x_B Bin: 8

(b) Normalized Comparison of p_T for Q^2-x_B Bin 8

(a) Normalized Comparison of Q^2 (b) Normalized Comparison of x_B (c) Normalized Comparison of z (d) Normalized Comparison of P_T (e) Normalized Comparison of ϕ_h .

195

C. MC Event Matching

In order to study the bin migration effects in the Monte Carlo simulation, reconstructed events had to be ‘matched’ to their generated counterparts. The Monte Carlo simulation used does not track information about the generated partner of a reconstructed particle, so this matching must be done event-by-event. This is done by matching the reconstructed particles to whichever generated particle has the most similar polar and azimuthal lab angles. In addition, the following requirements for a match are applied:

- Both the Reconstructed (REC) and Generated (GEN) particle must have the same electric charge.⁶
- $\Delta\theta_{(\text{REC} - \text{GEN})} < 6^\circ$
- $\Delta\phi_{(\text{REC} - \text{GEN})} < 10^\circ$
- Each particle can only have one match
- If more than one reconstructed particle fulfils the criteria above, the one with the smallest ‘ Δ ’ value defined below is chosen.

$$\Delta = \frac{|\Delta\theta_{(\text{REC}-\text{GEN})}|}{|\theta_{\text{REC}}|} + \frac{|\Delta\phi_{(\text{REC}-\text{GEN})}|}{|\phi_{\text{REC}}|} \quad (20)$$

With these criteria and after all other analysis cuts, the majority of reconstructed events (more than 98%) are able to be matched to a generated event. Unmatched events (defined as events in which either the electron or pion partners are not found within the given criteria) are excluded from the acceptance matrices.

211

D. Acceptance Matrices

In order to correct for acceptance while considering the effects of bin migration, the Acceptance matrix $A_{(i, j)}$ should be used where:

$$A_{(i, j)} = \frac{\text{Number of events generated in bin } j \text{ but reconstructed in bin } i}{\text{Total number of events generated in the } j\text{-th bin}} \quad (21)$$

where the values of the matrix are calculated using the Monte Carlo simulation. With this matrix, it is possible to go from a set of experimental data (represented by a vector \mathbf{Y}_i where this vector is equal to the number of events experimentally measured in the i -th bin) to the acceptance unfolded data (represented by a vector \mathbf{X}_j where this vector is equal to the number of acceptance-corrected events in the j -th bin). This can be done by unfolding the relation:⁷

$$\mathbf{Y}_i = A_{(i, j)} \mathbf{X}_j \iff \mathbf{X}_j = A_{(i, j)}^{-1} \mathbf{Y}_i \quad (22)$$

⁶ This requirement is done in place of having a PID requirement to allow for cases in which the event reconstruction mis-identifies a particle.

⁷ If $A_{(i, j)}$ does not have any non-diagonal terms (i.e., if for $i \neq j$, $A_{(i, j)} = 0$) then these terms can be applied in the same way as the correction factor η was in the [cross-section equation](#) from the [Introduction](#) section.

212 where the right-hand side of the equation gives the acceptance corrected form of a given data set.

213 To illustrate this Acceptance matrix, the Reconstructed Monte Carlo events can be plotted against
 214 the Matched Generated Monte Carlo events and normalized by the total number of Generated events
 215 per bin. The resulting histogram then shows the values of the Acceptance matrix within each
 216 histogram bin. In this analysis note, one dimensional Acceptance matrices were produced which only
 217 considered a single kinematic variable at a time (i.e., the bin migrations of the other variables were not
 218 considered within the individual examples shown). The final analysis will require a multidimensional
 219 Acceptance matrix which simultaneously considers bin migrations of all five kinematic variables (Q^2 ,
 220 x_B , z , P_T , and ϕ_h).

221 The examples used in this note consist of five equally sized bins for the kinematic variables Q^2 ,
 222 x_B , z , and P_T . The bin sizes are determined by the distribution of each variable, with the range of
 223 coverage being based on the two dimensional binning schemes discussed in the [Binning](#) section of
 224 this note. The number of bins per variable was chosen to very roughly imitate the two dimensional
 225 bins sizes, though an exact representation of these bins in only one dimension is not possible in such
 226 a simplified example. The ranges used and bin sizes are given with each of these examples, which
 227 are included in the final section of this analysis note ([Plots Requested for Release](#)).

228 In addition to these Acceptance matrices, an additional set of ‘Response matrices’ are also given
 229 with a larger number of bins used (these matrices do not try to imitate the 2D binning schemes).
 230 Response matrices differ from the Acceptance matrices in that they are not normalized to the total
 231 number of events generated in each given bin. They correspond only to the numerator of the definition
 232 of Acceptance matrices (see [Eq. 21](#)). The reason for their use mainly relates to the application of
 233 unfolding procedures such as the Singular Value Decomposition (SVD) or Bayesian method, which
 234 both allows one to unfold and regularize the experimental data given this simulated Response matrix.
 235 While the SVD method does this through calculating the inverted response matrix, the Bayesian
 236 method takes an iterative approach to predict the unfolded response matrix using an algorithm
 237 based on elements of Bayesian statistics. A full description of the SVD method can be see in
 238 “SVD Approach to Data Unfolding” by Andreas Höcker and Vakhtang Kartvelishvili [12] while the
 239 Bayesian method was introduced by Giulio D’Agostini in “A Multidimensional unfolding method
 240 based on Bayes’ theorem” [13].

241 An implementation of the both the SVD method (for single variable matrices with the same
 242 number of bins for the measured and the unfolded spectrum) and the Bayesian method are already
 243 available in the ROOT library called ‘RooUnfold’. In the case of the SVD method, the ‘RooUnfold’
 244 library uses another existing library known as ‘TSVDUnfold’ which was independently used during
 245 the initial implementation of the unfolding procedures used in this analysis. These libraries take as
 246 inputs a set of 1D histograms for the generated and reconstructed simulations and a Response matrix,
 247 which are then all used to unfold the experimental data. With the implementation of the ‘RooUnfold’
 248 library, these inputs are stored in a custom Response matrix object (i.e., `RooUnfoldResponse`) which
 249 is allows for the easy application of several different unfolding methods such as those used in this
 250 analysis. The application of the ‘TSVDUnfold’ library’s basic example was used to help set the
 251 regularization parameter of `kreg = 13` (used to regularize the final unfolded distributions) for this
 252 analysis.⁸ The example used to model the application of the SVD method is available within the
 253 ROOT Reference Guide for `TSVDUnfoldExample.C`.⁹ The number of iterations used for the Bayesian

⁸ The regularization parameter used in the unfolding procedure presented in this note was chosen as a preliminary test of the SVD method. This choice of the regularization parameter was shown to work reasonably well for the current systems it was applied to, however, future developments in this analysis, especially regarding plans for multidimensional binning and unfolding will likely generate the need to revisit this parameter’s value at a later time. For the purposes of demonstrating the unfolded procedure in this note, this parameter is a reasonable choice.

⁹ This example is available here: https://root.cern/doc/master/TSVDUnfoldExample_8C.html

method was increased from the default value of 4 used by ‘RooUnfold’ to 10 iterations to help ensure the convergence of the χ^2 value used to evaluate how well each iteration performed. The plotted results of these procedures, as well as comparisons between all of the unfolding methods, for the kinematic variables Q^2 , x_B , z , and P_T are included in the final section of this analysis note ([Plots Requested for Release](#)).

The one dimensional comparisons between the SVD, Bayesian, and bin-by-bin methods demonstrates the relative similarities between them, which is preferable in these examples as a way to verify that the more complex methods are being applied reasonably. At this stage, there should not be as significant of a difference between the results of these methods, since any matrix unfolding method should give increasingly similar results to the bin-by-bin method as the number of off-diagonal terms gets smaller (i.e., a completely diagonal Response/Acceptance Matrix should inherently give the same correction as the bin-by-bin correction). In higher dimensions, the Bayesian method will become more essential as its iterative procedure does not make use of continuous variables, making it more applicable to multidimensional problems than other unfolding methods. [13]

For each set of images showing this comparison of the acceptance corrections, (see [Figures 48-51](#) in the [Plots Requested for Release](#) section of this note), the following descriptions apply to each set of figures:

- Radiative effects are NOT included in any of these plots (i.e., have not been introduced to the Monte Carlo simulations yet).
- All other variables not explicitly mentioned in the figure were integrated over during the creation of these plots (i.e., each plot encompasses the whole range of kinematics from the other variables not listed).
- The **top left** plot show the 2D Response matrix used as an input for the SVD and Bayesian methods.
- The **bottom left** plot shows the 1D, bin-by-bin acceptance correction factor, which was defined in the [Introduction](#) section of this note.
- The **top right** plots shows a normalized comparison between the uncorrected distributions of the experimental data (in blue) and the Monte Carlo Reconstructed data (in red).
- The **bottom right** plots shows a normalized comparison between the SVD Unfolded distribution (in pink), the bin-by-bin acceptance corrected distribution (in brown), the Bayesian Unfolded distribution (in dark green), and the Monte Carlo Generated distribution (in light green).

VII. UNFOLDING ϕ_h DISTRIBUTIONS

Following the unfolding procedures discussed in [Acceptance Matrices](#), the desired results of this analysis will be to perform a multidimensional unfolding correction for the ϕ_h distribution which can then be fit with [Eq. 16](#) to extract the azimuthal moments of the SIDIS cross-section as functions of Q^2 , x_B , z , and P_T . At this time, the unfolding of the ϕ_h distributions is not done as a fully multidimensional process, as this aspect of the analysis is still being developed. Plots included in this analysis note will show the preliminary results of the one dimensional unfolded distributions of ϕ_h when plotted within each of the separate kinematic bins. In these plots, the kinematic bins were treated as additional ‘cuts’ before the creation of the necessary histograms for the unfolding procedures (i.e., a new set of the necessary histograms for unfolding is created for each separate kinematic bin which are only filled with events from that specific bin). The unfolded ϕ_h distributions are then fitted with an equation of the form of [Eq. 16](#). These one dimensional examples are meant to provide an opportunity to test the implementations of the unfolding methods on a simplified version of the larger multidimensional problem faced by this analysis and will likely serve as a useful point of comparison when the fully multidimensional corrections are performed (much like how the bin-by-bin corrections are currently used for a comparison with the more complex unfolding procedures already discussed). Plots included in this analysis note show, for every z - P_T bin in the first and last Q^2 - x_B bin, the unfolded distributions of ϕ_h using the Bayesian, SVD, and Bin-by-bin correction methods along with the corresponding response matrices and pre-unfolded distributions in the experimental and Monte Carlo data (see below¹⁰). These images, along with those for all of the other Q^2 - x_B bins, are all documented and kept updated on the following web page created for this analysis: https://userweb.jlab.org/~richcap/Interactive_Webpage_SIDIS_richcap/Interactive_Unfolding_Page.html.

¹⁰ The z - P_T plots in these images are flipped so that the variable P_T is on the y-axis and z is on the x-axis. As such, to be consistent with the normal method of defining the z - P_T bins (i.e., starting at the top-left-most bin when plotting z vs P_T and increasing from left to right), the z - P_T bins are placed in the grid such that the first bin starts in the bottom-right-most corner of the grid with the bin numbers increasing from bottom to top. Aside from this visual difference, all other elements of these plots are consistent with the other similar plots included in this analysis note.

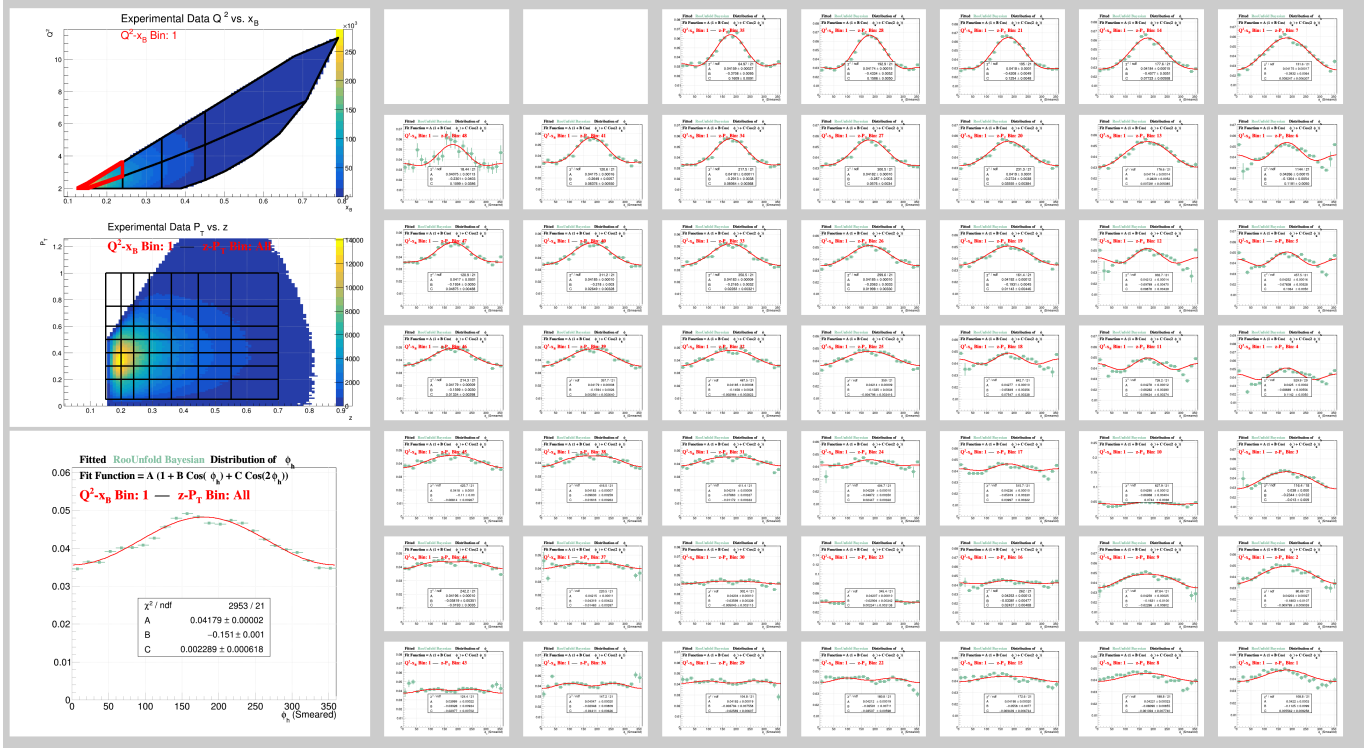


FIG. 26: ϕ_h Unfolded distributions using the **Bayesian Unfolding method**. Plots show the distributions within Q^2 - x_B Bin 1 (highlighted in red) and in each of the individual z - P_T bins. Each plot has been fitted with an equation of the form of Eq. 16.

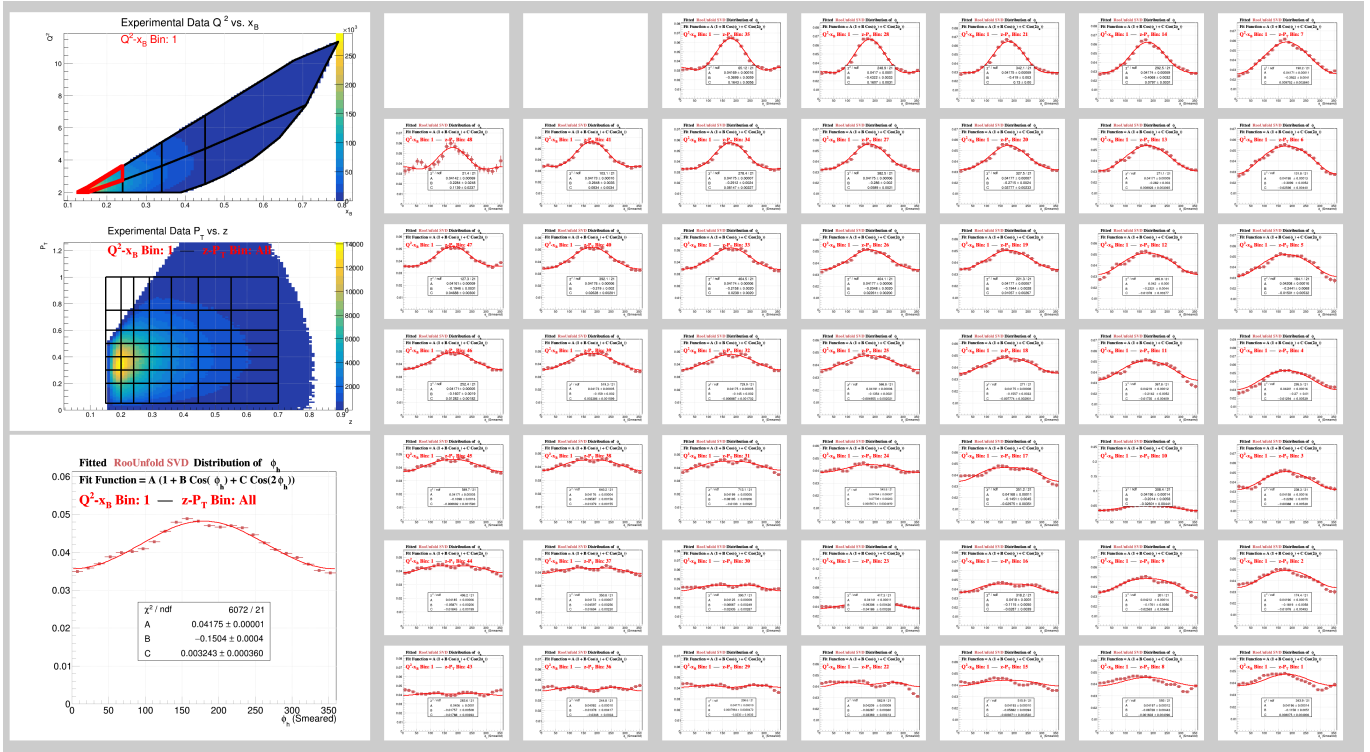


FIG. 27: ϕ_h Unfolded distributions using the **SVD Unfolding method** (using the ‘RooUnfold’ library). Plots show the distributions within Q^2 - x_B Bin 1 (highlighted in red) and in each of the individual z - P_T bins. Each plot has been fitted with an equation of the form of Eq. 16.

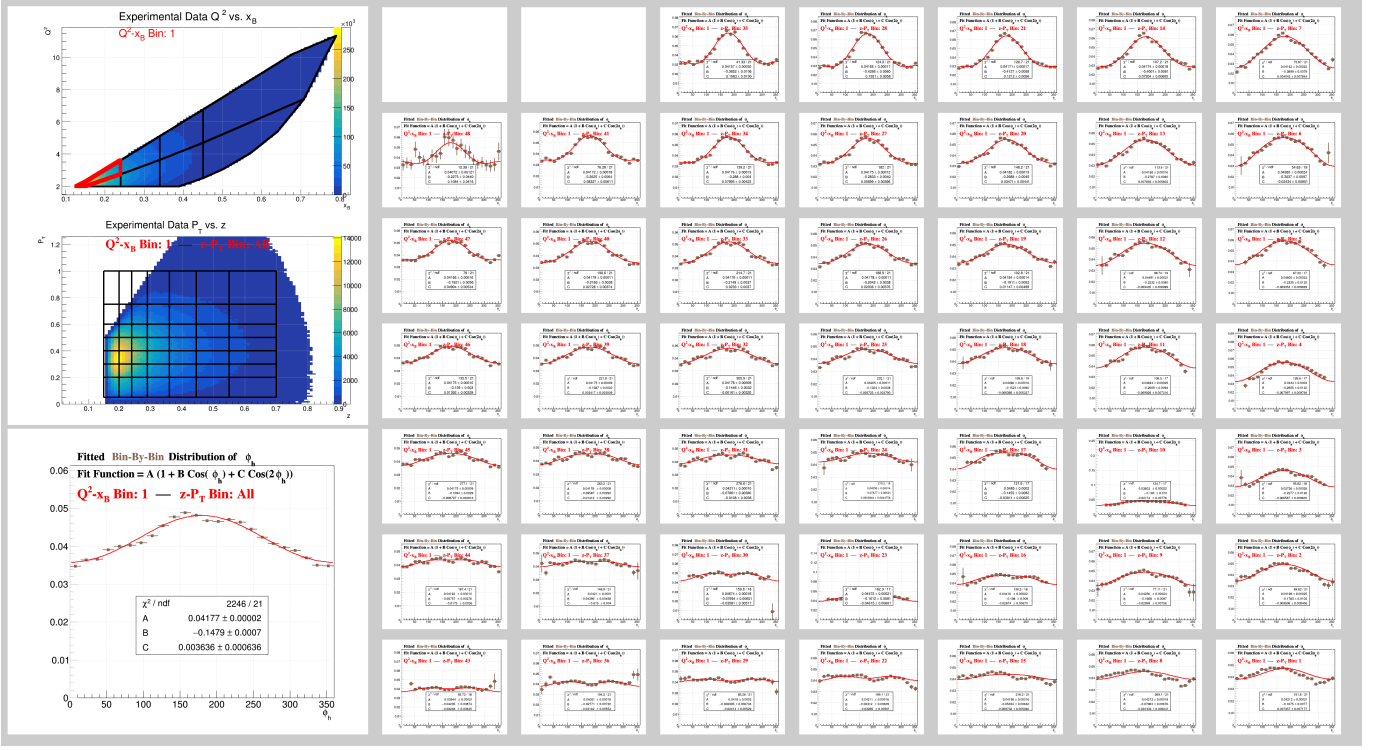


FIG. 28: ϕ_h Unfolded distributions using the **Bin-by-bin Correction method**. Plots show the distributions within Q^2 - x_B Bin 1 (highlighted in red) and in each of the individual z - P_T bins. Each plot has been fitted with an equation of the form of Eq. 16.

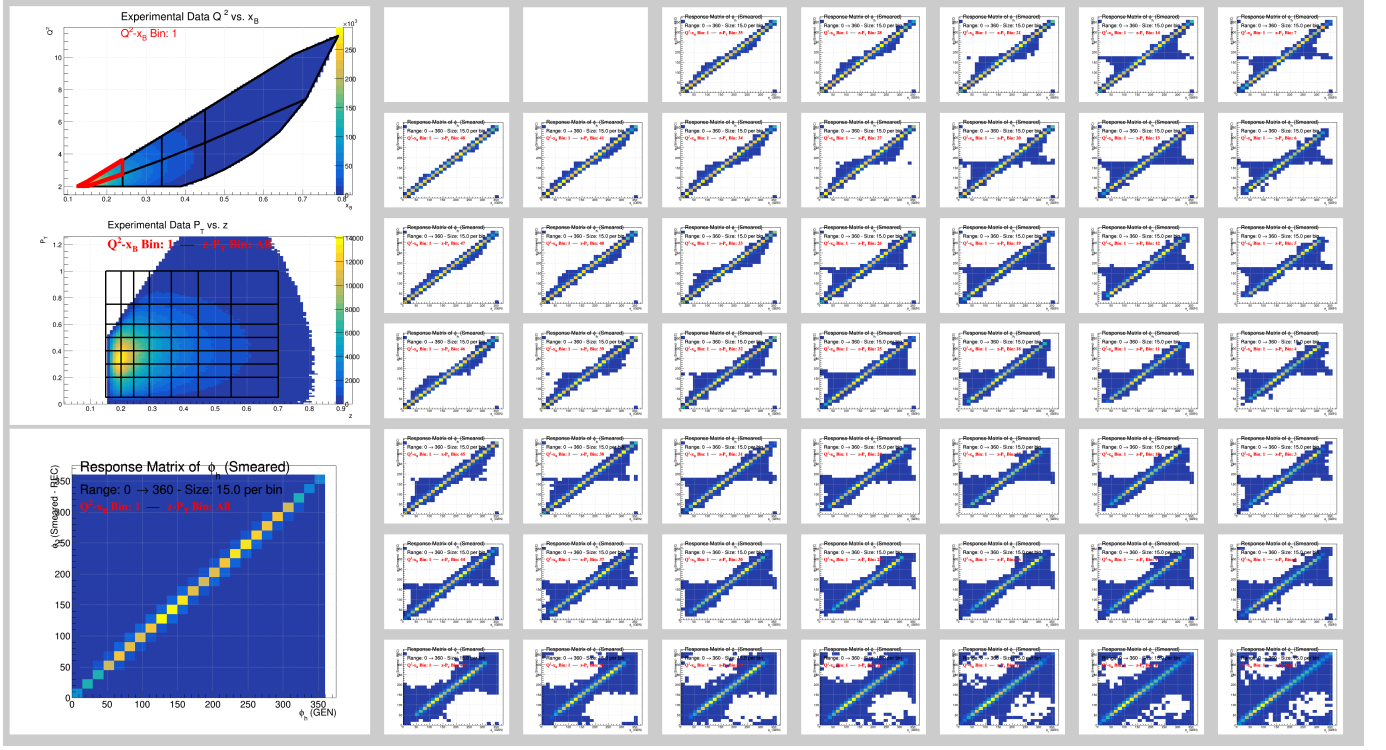


FIG. 29: Response Matrices for ϕ_h distributions within Q^2 - x_B Bin 1 (highlighted in red) and in each of the individual z - P_T bins. These response matrices are used in the Bayesian and SVD unfolding procedures shown above.

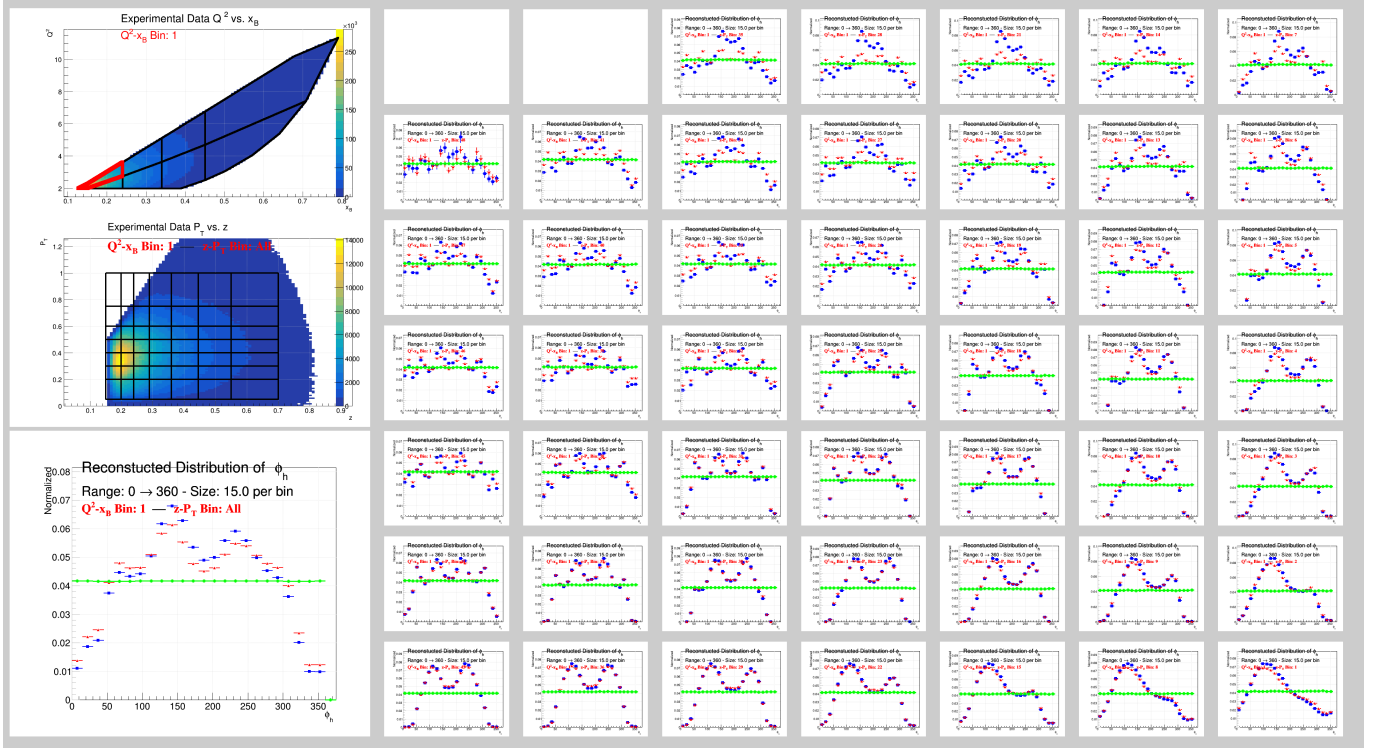


FIG. 30: Normalized ϕ_h distributions before unfolding. Plots show the distributions within Q^2 - x_B Bin 1 (highlighted in red) and in each of the individual z - P_T bins. The plots in blue show the distributions as measured in the experimental data while the red and green plots show the corresponding reconstructed and generated distributions within the Monte Carlo data files.

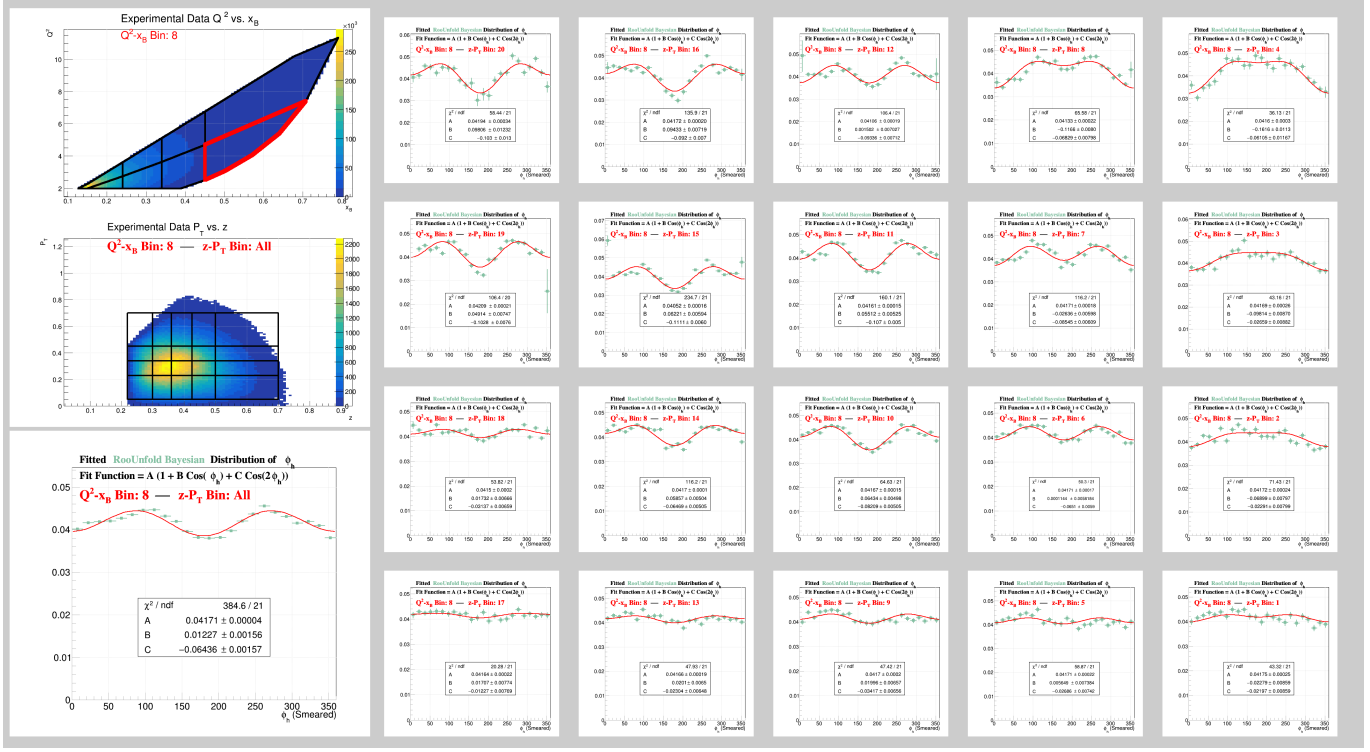


FIG. 31: ϕ_h Unfolded distributions using the **Bayesian Unfolding method**. Plots show the distributions within $Q^2 \cdot x_B$ Bin 8 (highlighted in red) and in each of the individual $z \cdot P_T$ bins. Each plot has been fitted with an equation of the form of Eq. 16.

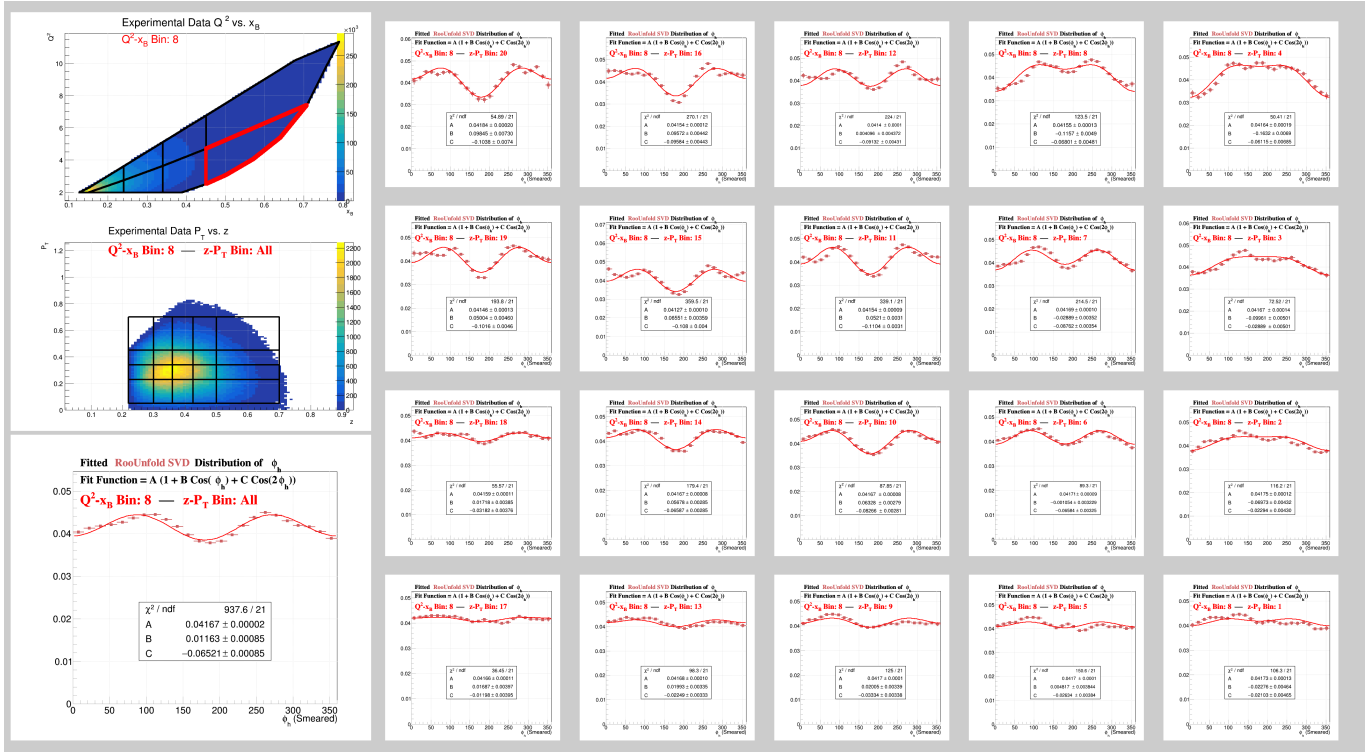


FIG. 32: ϕ_h Unfolded distributions using the **SVD Unfolding method** (using the ‘RooUnfold’ library). Plots show the distributions within $Q^2 \cdot x_B$ Bin 8 (highlighted in red) and in each of the individual $z \cdot P_T$ bins. Each plot has been fitted with an equation of the form of Eq. 16.

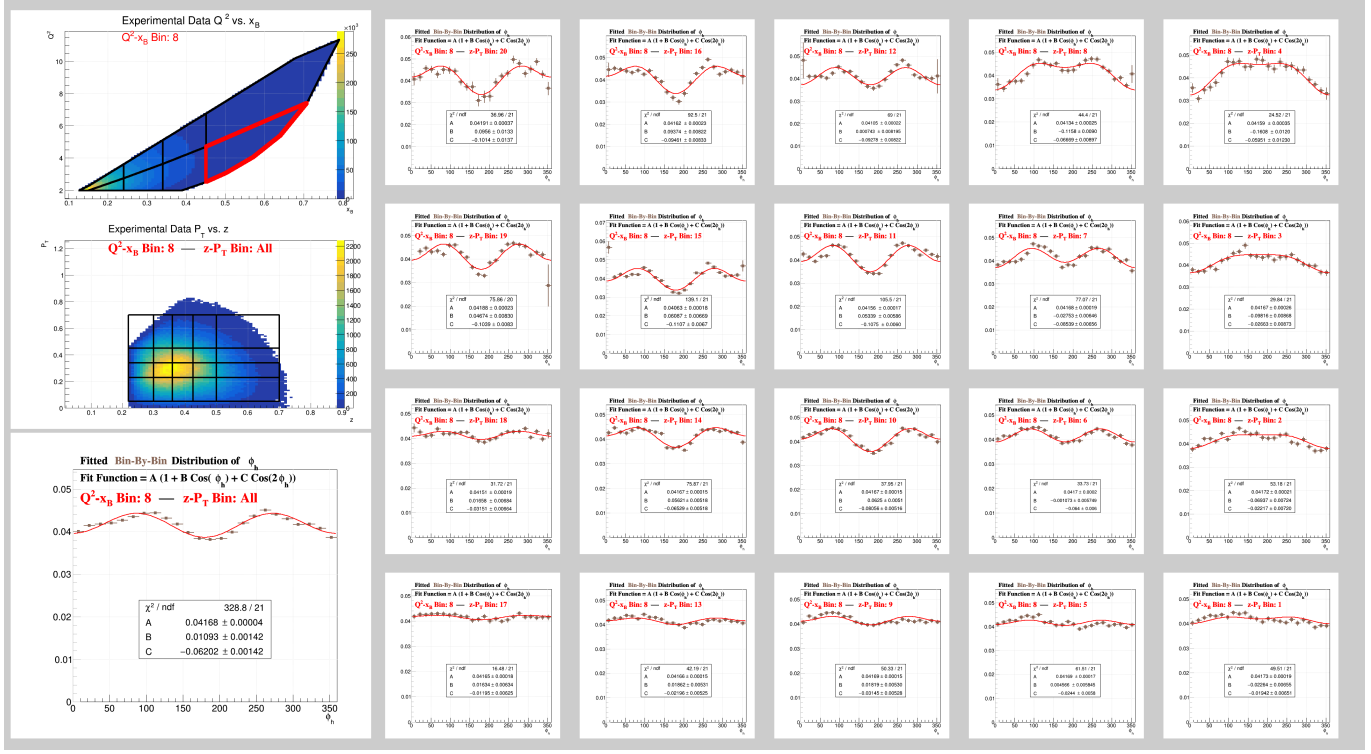


FIG. 33: ϕ_h Unfolded distributions using the **Bin-by-bin Correction method**. Plots show the distributions within Q^2 - x_B Bin 8 (highlighted in red) and in each of the individual z - P_T bins. Each plot has been fitted with an equation of the form of Eq. 16.

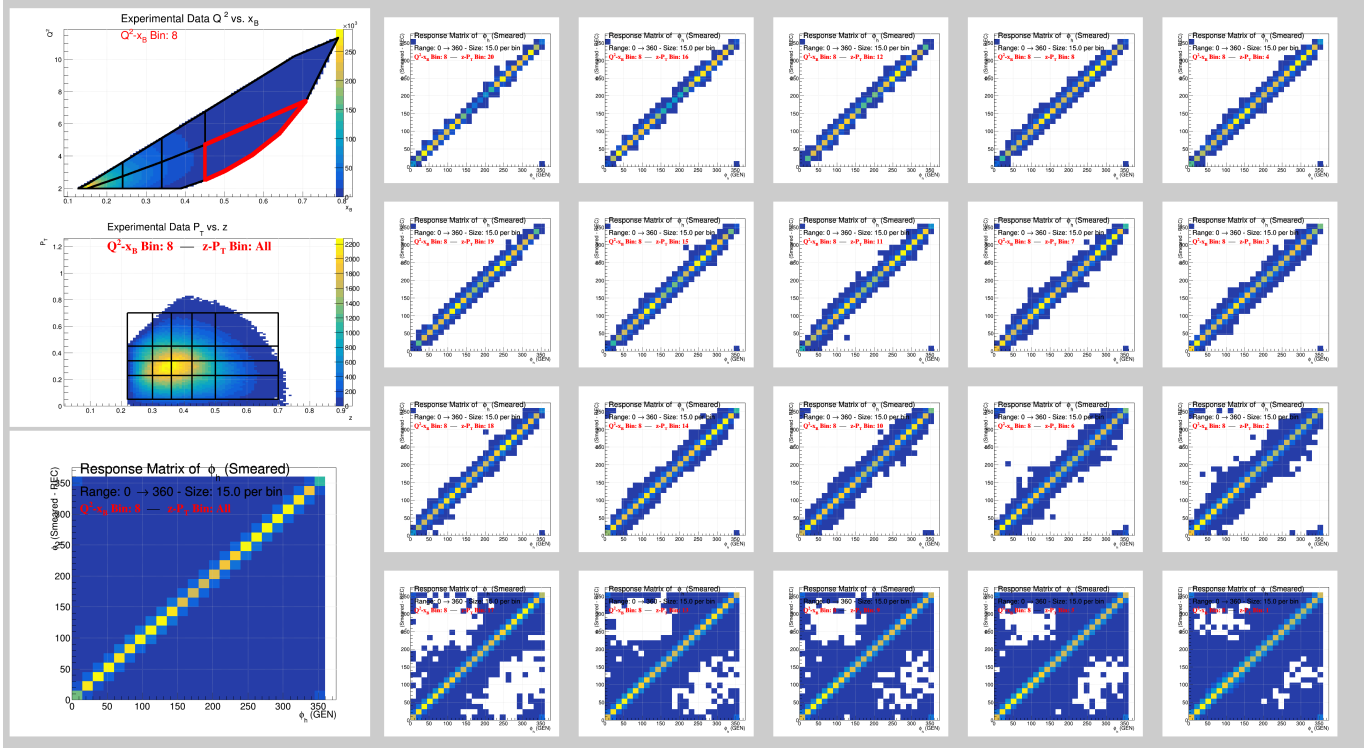


FIG. 34: **Response Matrices** for ϕ_h distributions within Q^2 - x_B Bin 8 (highlighted in red) and in each of the individual z - P_T bins. These response matrices are used in the Bayesian and SVD unfolding procedures shown above.

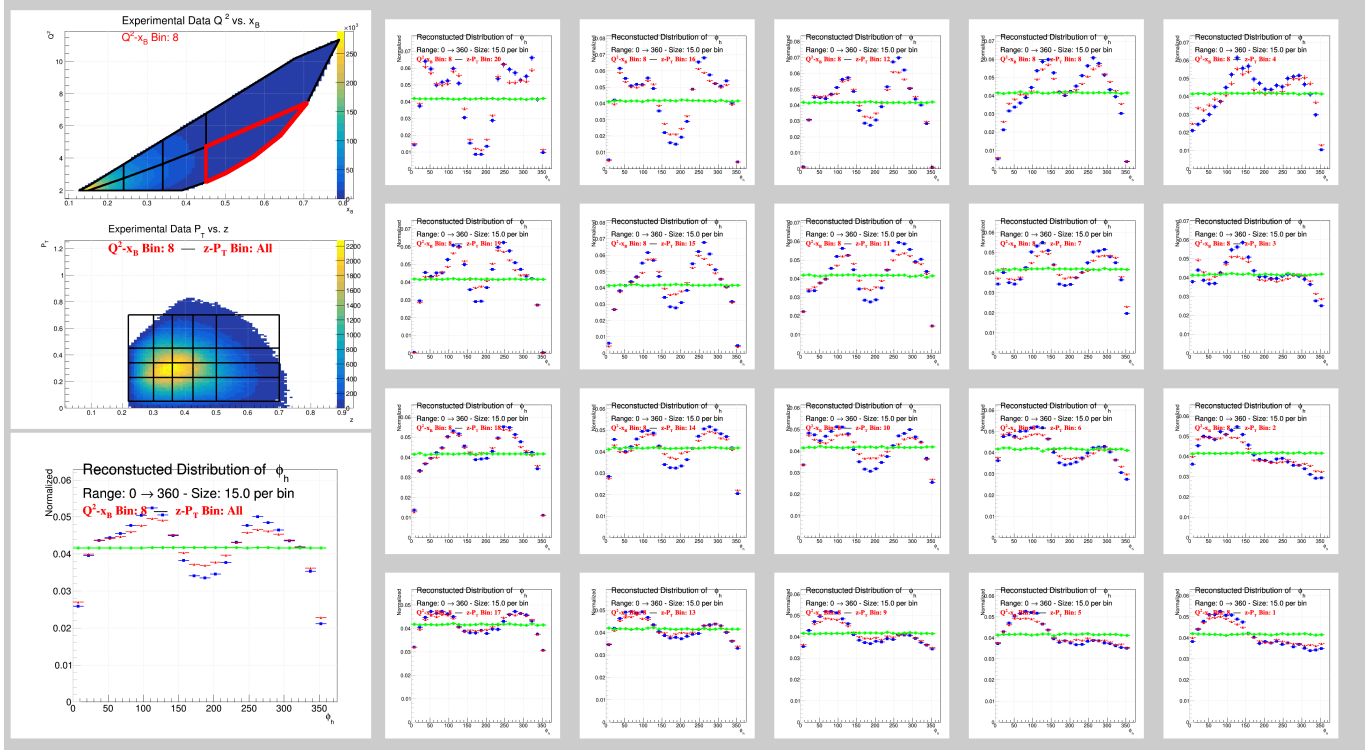


FIG. 35: Normalized ϕ_h distributions before unfolding. Plots show the distributions within Q^2 - x_B Bin 8 (highlighted in red) and in each of the individual z - P_T bins. The plots in blue show the distributions as measured in the experimental data while the red and green plots show the corresponding reconstructed and generated distributions within the Monte Carlo data files.

309

VIII. PLOTS REQUESTED FOR RELEASE

310 The images shown in this section are planned to be shown at the upcoming “APS Topical Group on
 311 Hadronic Physics” and the “April APS Quarks to Cosmos” conferences in Minneapolis, Minnesota.
 312 All details that are to be presented have been discussed in the prior sections of this analysis note.

313 Several of the figures below have already been approved for release and shown at the previous
 314 Division of Nuclear Physics Conference in New Orleans, LA, and the Gordon Research Conference
 315 in Holderness, NH (these conference were both held in 2022). Figures 48-51 have been updated since
 316 these conferences to include the Unfolded Bayesian distributions and the new smearing functions
 317 and momentum corrections. Figures 42-46 have been added to show at the upcoming conferences
 318 to provide examples of the unfolding procedures currently being performed. All other plots in this
 319 section are as they appeared when they were originally approved.

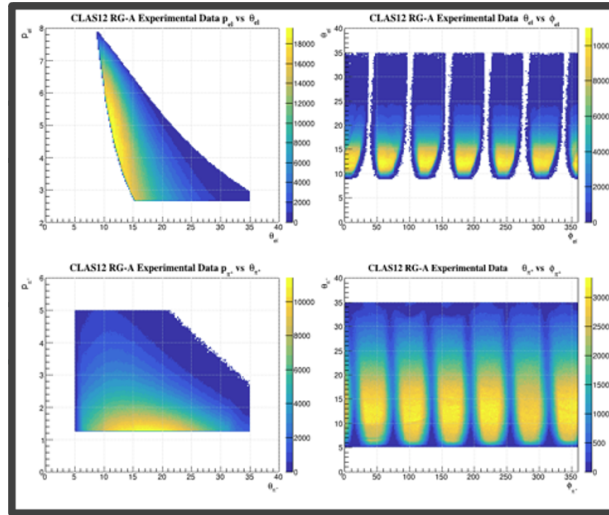


FIG. 36: Particle Kinematics after cuts. Discussed in [Distributions](#).

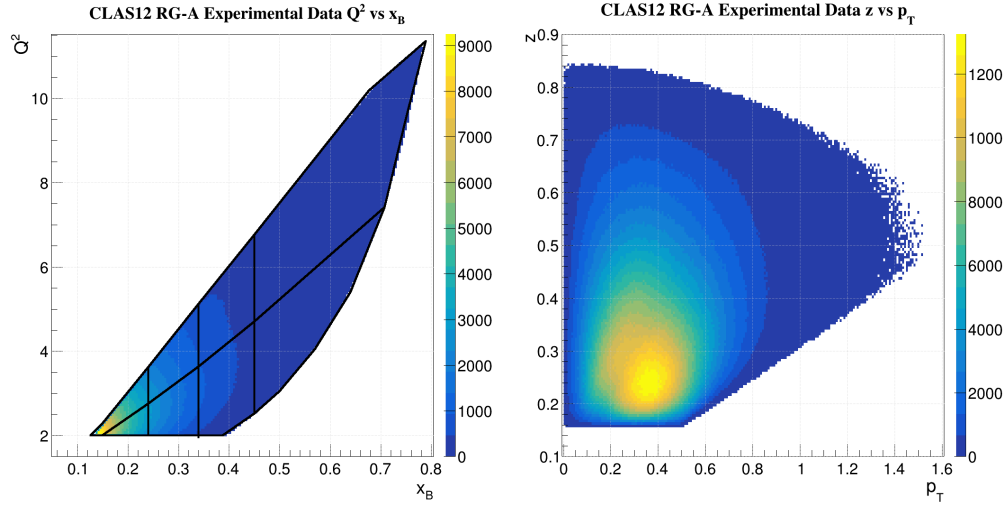


FIG. 37: 2D distributions of Q^2 , x_B , z , and P_T after all analysis cuts are applied to the RG-A data. Discussed in [Distributions](#).

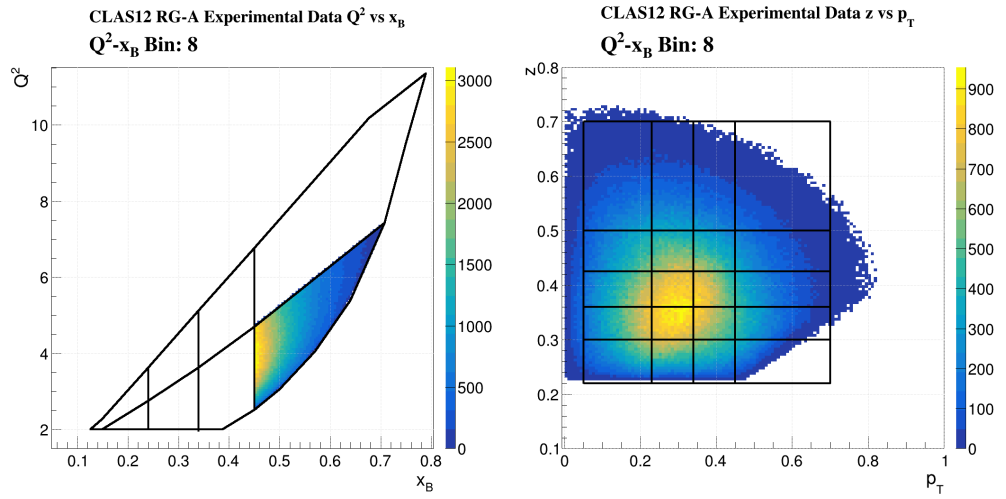


FIG. 38: 2D distributions of Q^2 , x_B , z , and P_T after all analysis cuts are applied to the RG-A data. Figure shows events in Q^2 - x_B bin 8. Discussed in [Binning](#). Will be shown as a single example of the kinematic bins.

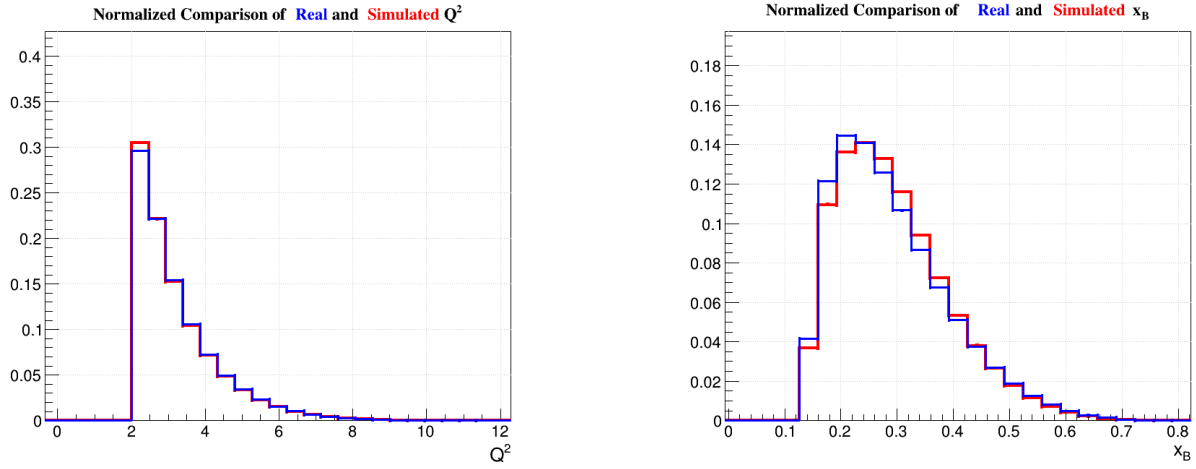
(a) Normalized Comparison of Q^2 (b) Normalized Comparison of x_B .

FIG. 39: Discussed in Data vs MC Comparison.

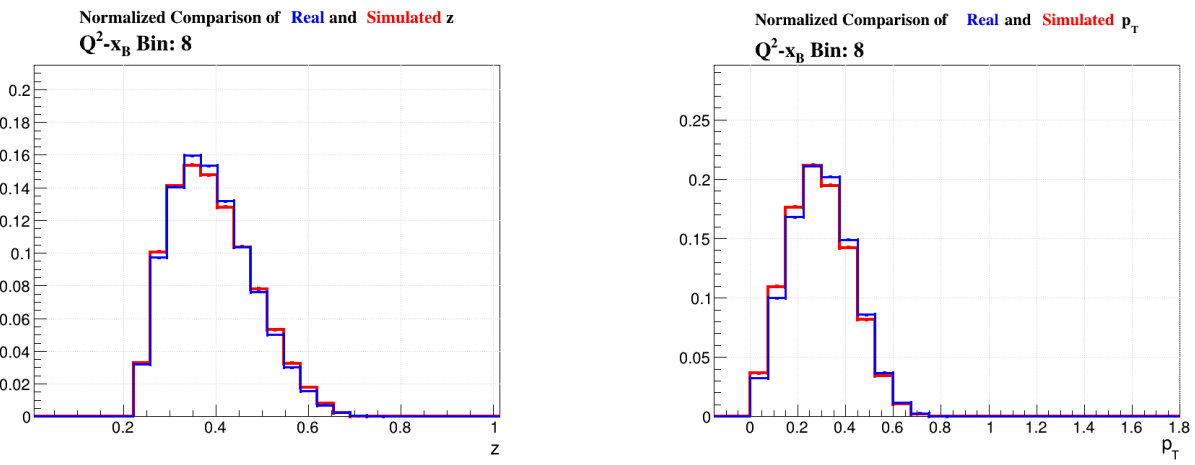
(a) Normalized Comparison of z for Q^2-x_B Bin 8(b) Normalized Comparison of P_T for Q^2-x_B Bin 8

FIG. 40: Discussed in Data vs MC Comparison. Will be shown as examples of the kinematic bins.

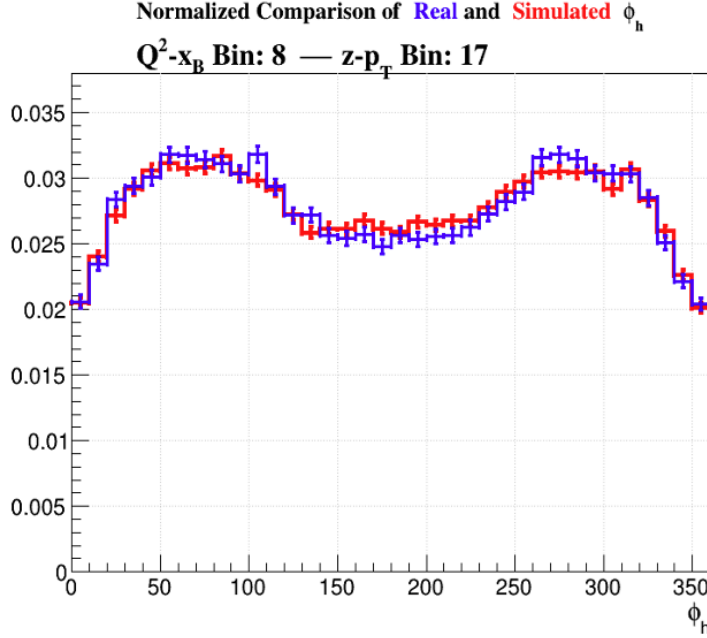


FIG. 41: Normalized Comparison of ϕ_h . Figure shows events in Q^2-x_B bin 8 and $z-P_T$ bin 17 (bottom-left most corner of the $z-P_T$ bins for this Q^2-x_B bin). Discussed in [Data vs MC Comparison](#). Has been shown as a single example of the kinematic bins.

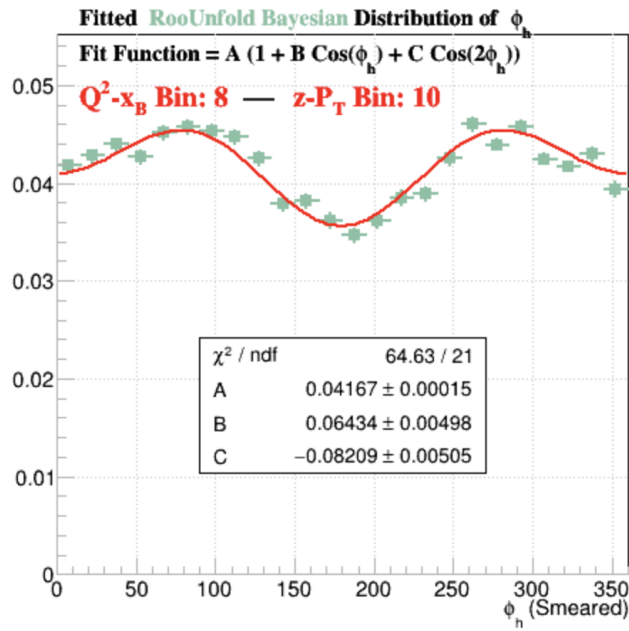


FIG. 42: Normalized Unfolded distribution of ϕ_h using the Bayesian Method. Figure shows events in Q^2-x_B bin 8 and $z-P_T$ bin 10 (one of the $z-P_T$ bins in the center of the binning scheme). Discussed in [Unfolded \$\phi_h\$ Distributions](#). Will be shown as an example of the unfolding results within a single kinematic bins.

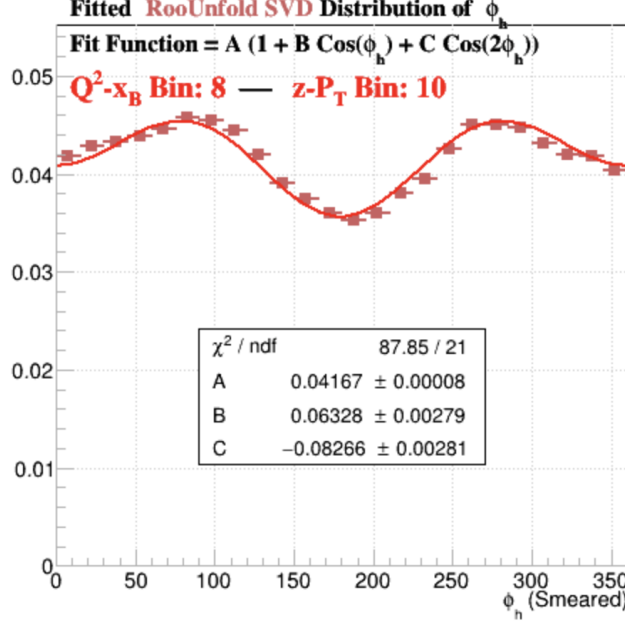


FIG. 43: Normalized Unfolded distribution of ϕ_h using the SVD Method. Figure shows events in Q^2-x_B bin 8 and $z-P_T$ bin 10 (one of the $z-P_T$ bins in the center of the binning scheme). Discussed in [Unfolded \$\phi_h\$ Distributions](#). Will be shown as an example of the unfolding results within a single kinematic bins.

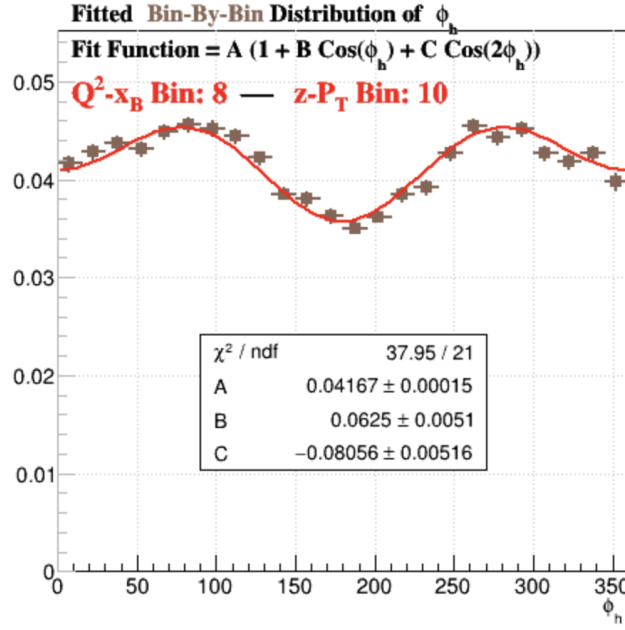


FIG. 44: Normalized Unfolded distribution of ϕ_h using the Bin-by-bin Method. Figure shows events in Q^2-x_B bin 8 and $z-P_T$ bin 10 (one of the $z-P_T$ bins in the center of the binning scheme). Discussed in [Unfolded \$\phi_h\$ Distributions](#). Will be shown as an example of the unfolding results within a single kinematic bins.

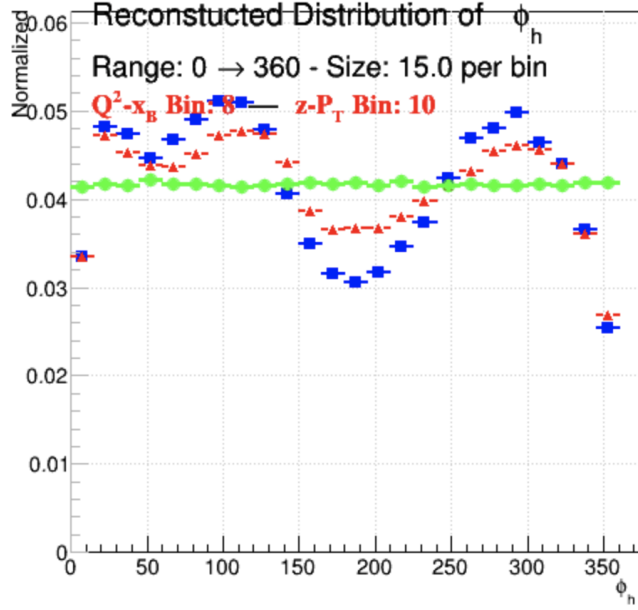


FIG. 45: Normalized Comparison of ϕ_h in the Experimental (blue) and Monte Carlo Reconstructed (red)/Generated (green) data sets. Figure shows events in Q^2 - x_B bin 8 and z - P_T bin 10 (one of the z - P_T bins in the center of the binning scheme). Discussed in [Unfolded \$\phi_h\$ Distributions](#). Will be shown as an example of the distribution of ϕ_h within a single kinematic bins before unfolding.

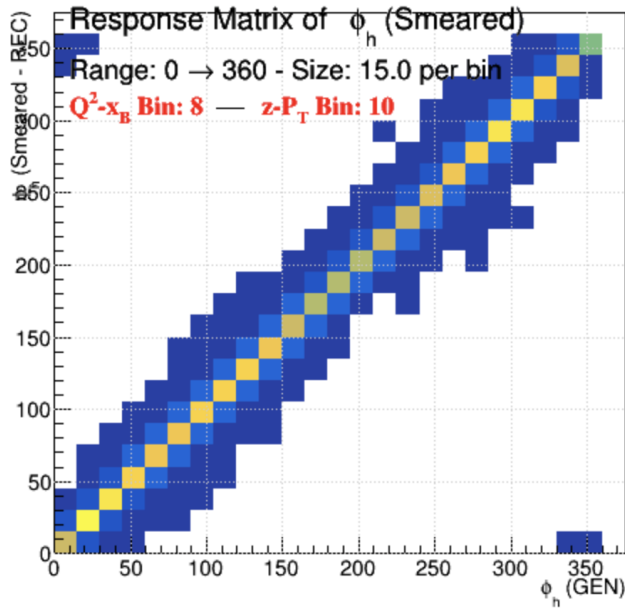


FIG. 46: Response Matrix for ϕ_h in Q^2 - x_B bin 8 and z - P_T bin 10 (one of the z - P_T bins in the center of the binning scheme). Discussed in [Unfolded \$\phi_h\$ Distributions](#). May be shown as an example of the response matrix used to produce the unfolded distributions in Figures 38-40.

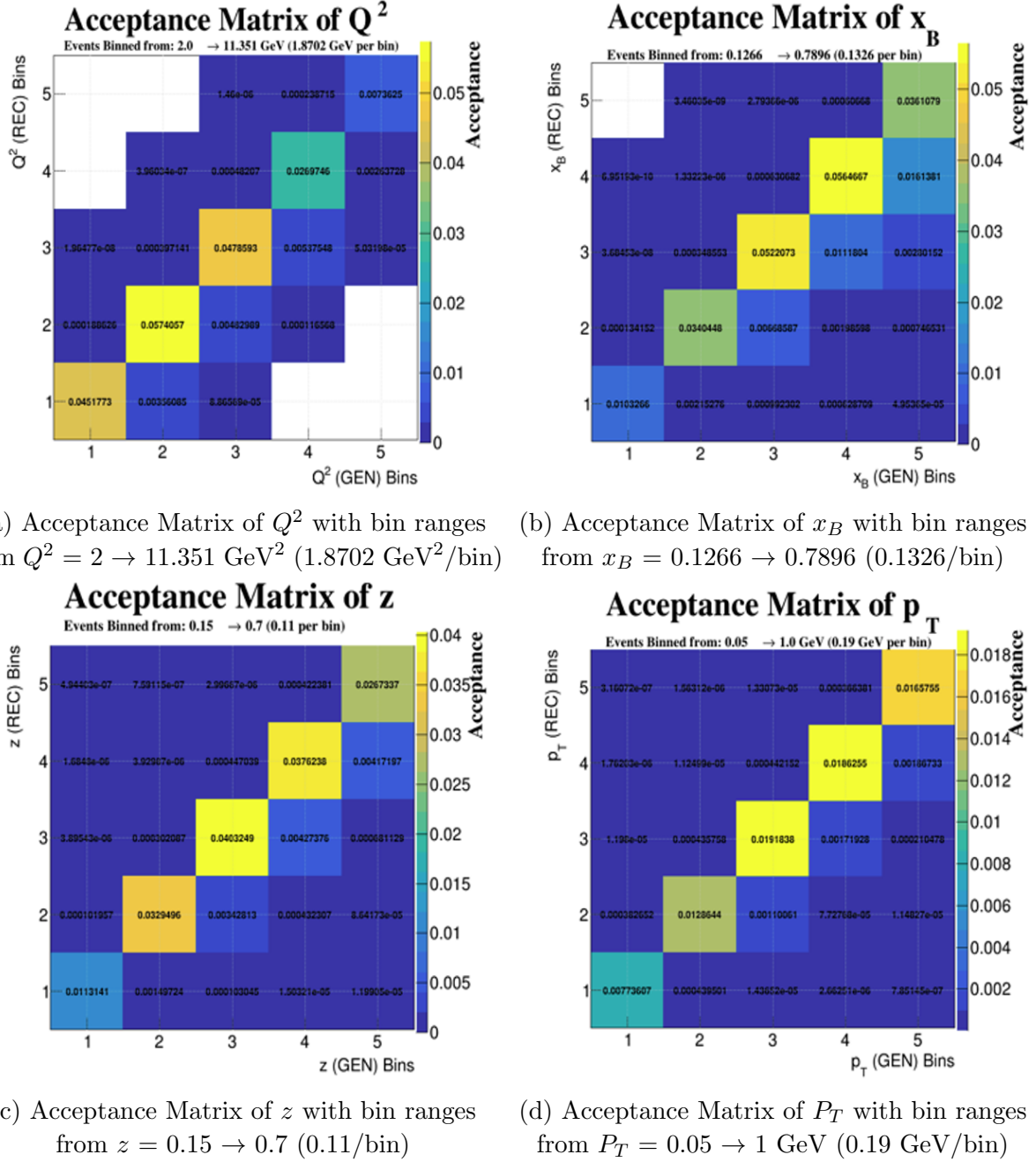


FIG. 47: Discussed in [Acceptance Matrices](#). Each matrix shown consists of 5 equally sized bins (sizes of each bin given in captions). The ranges of each bin are given in the captions of each image, with all other kinematic variables being integrated over all space.

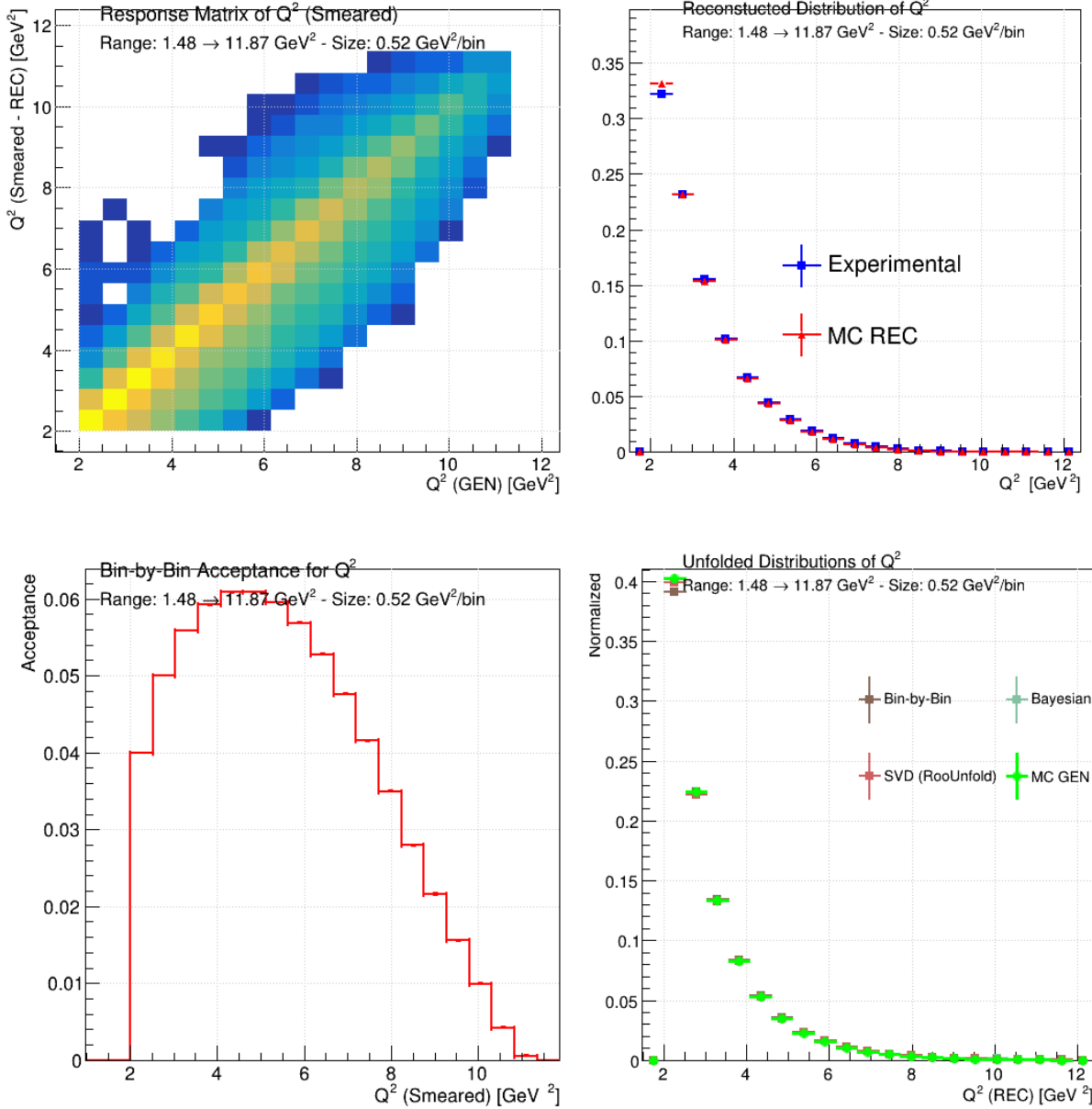


FIG. 48: Normalized Comparisons between data sets (including unfolded data) for Q^2 . Also discussed in [Acceptance Matrices](#) (See this section for more details).

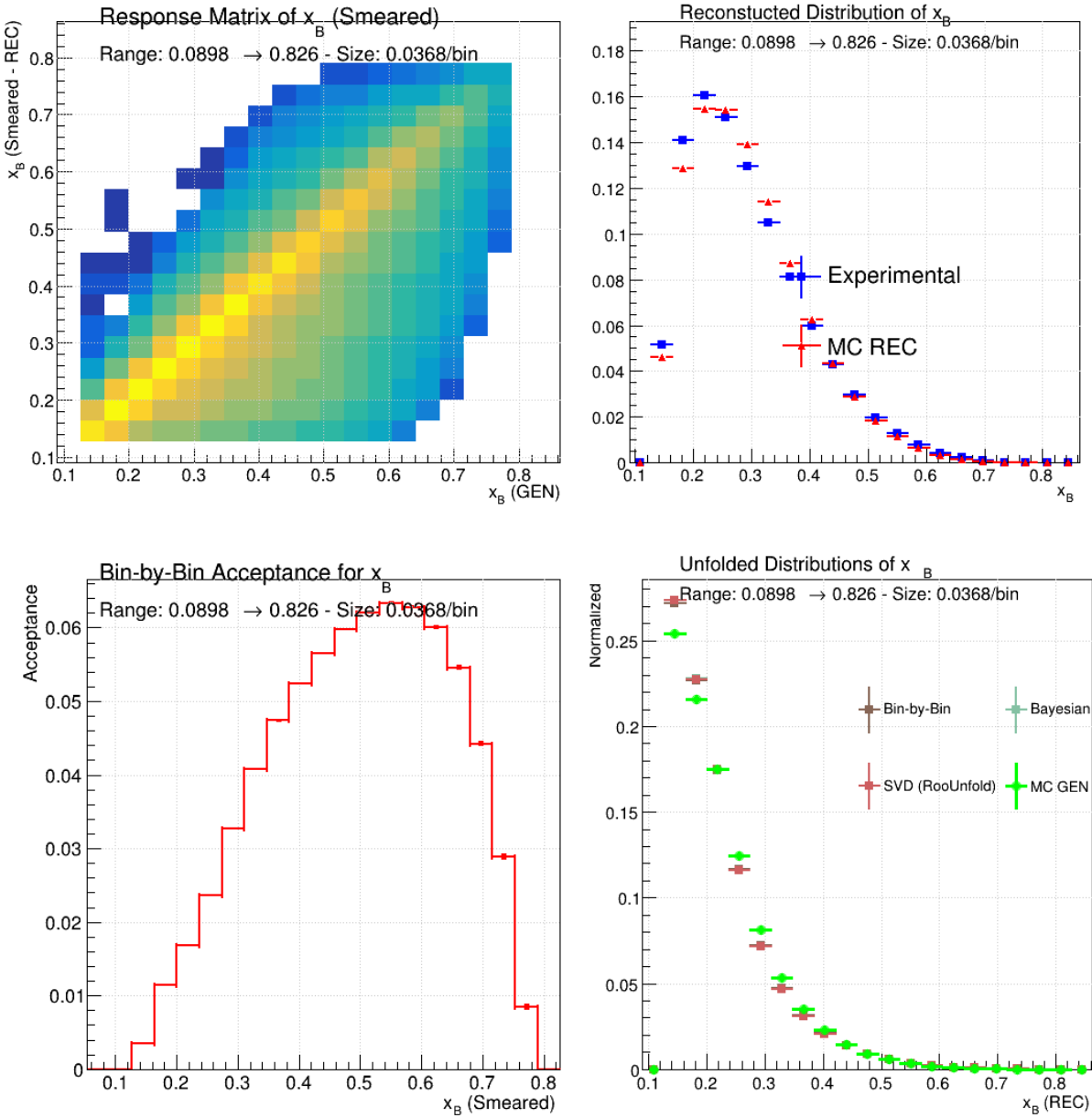


FIG. 49: Normalized Comparisons between data sets (including unfolded data) for x_B . Also discussed in [Acceptance Matrices](#) (See this section for more details).

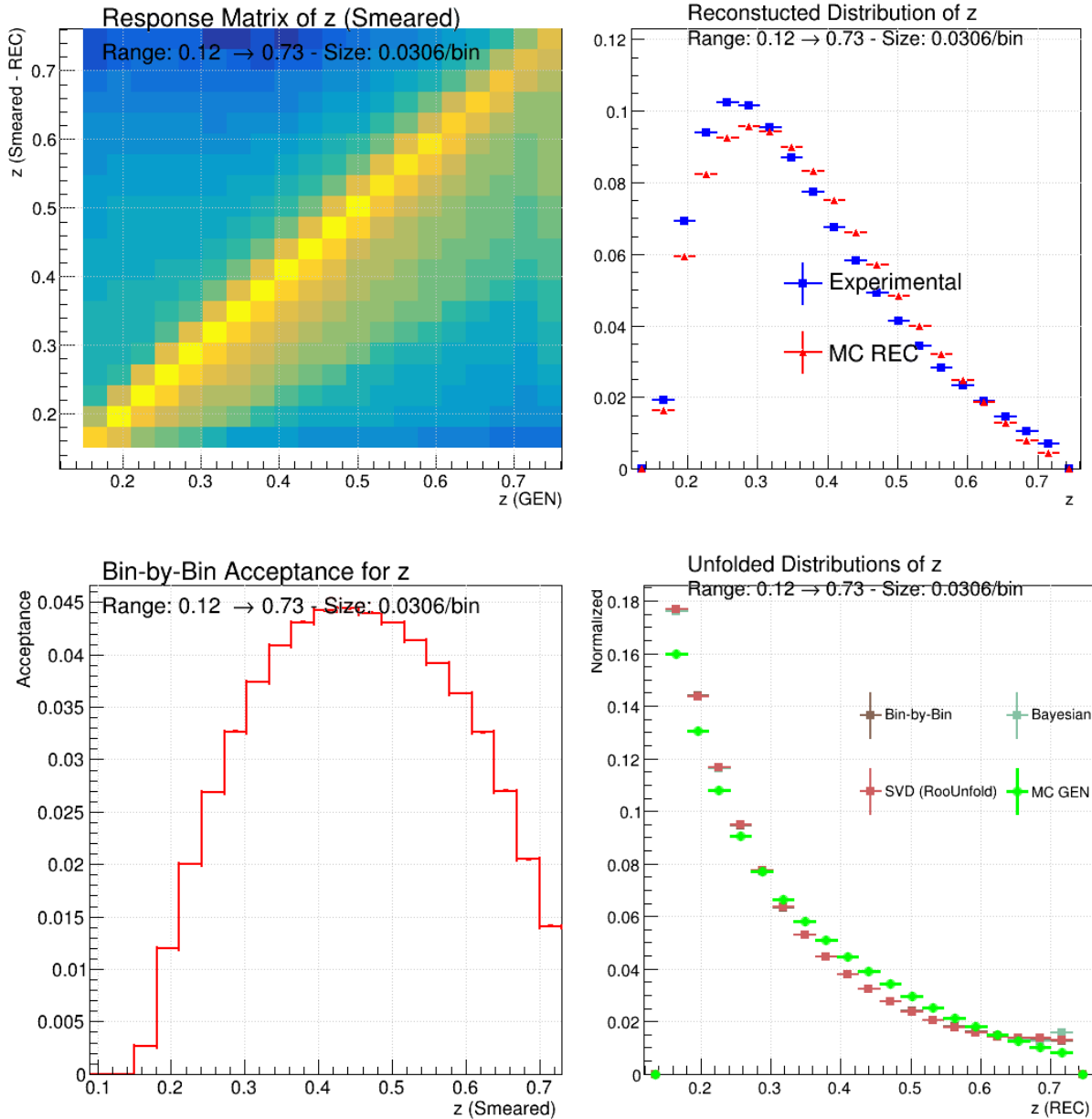


FIG. 50: Normalized Comparisons between data sets (including unfolded data) for z . Also discussed in [Acceptance Matrices](#) (See this section for more details).

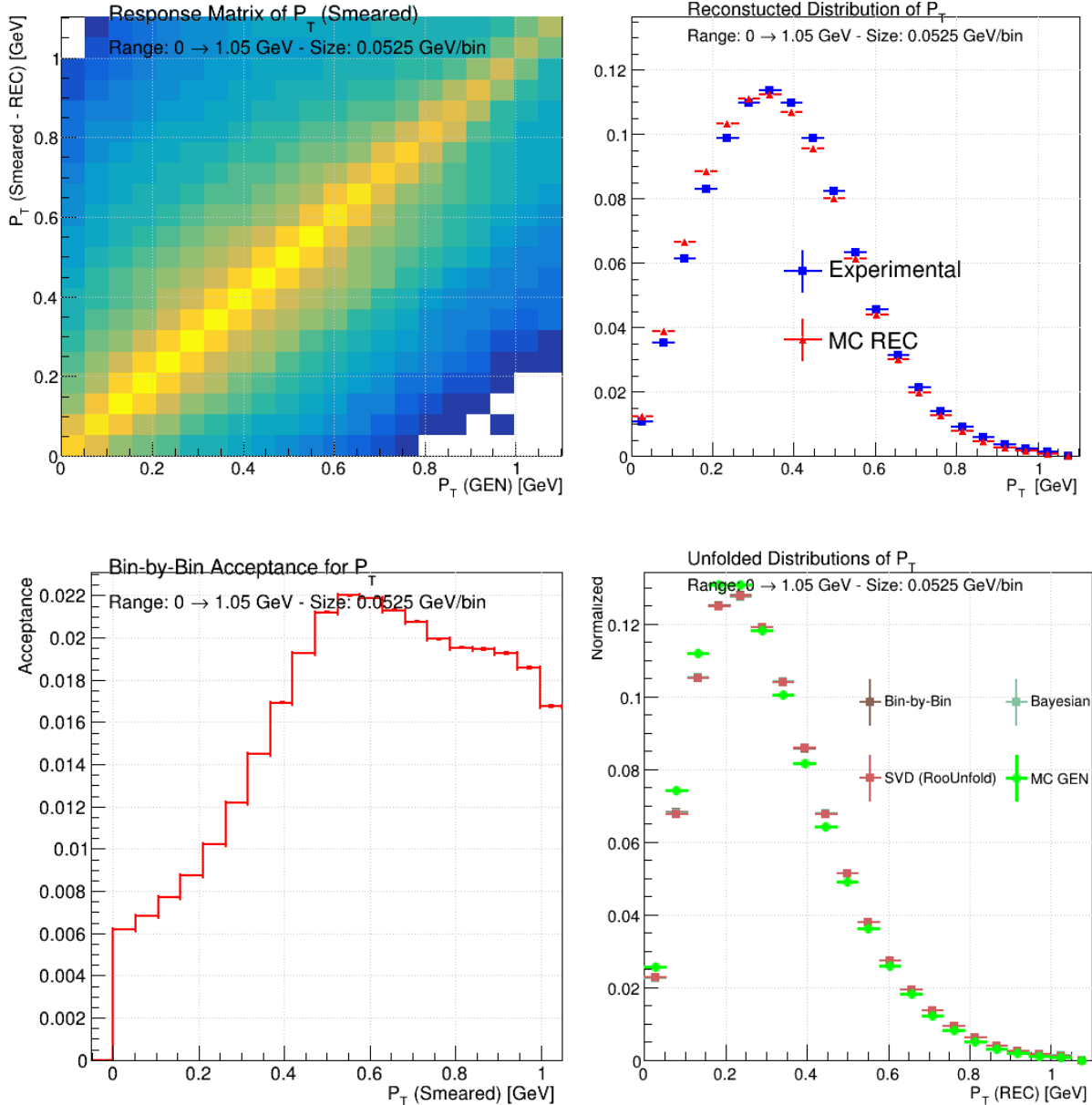


FIG. 51: Normalized Comparisons between data sets (including unfolded data) for P_T . Also discussed in [Acceptance Matrices](#) (See this section for more details).

³²⁰ The following images are to be released to visually demonstrate the cuts described in the [Data](#)
³²¹ [Analysis](#) Section.

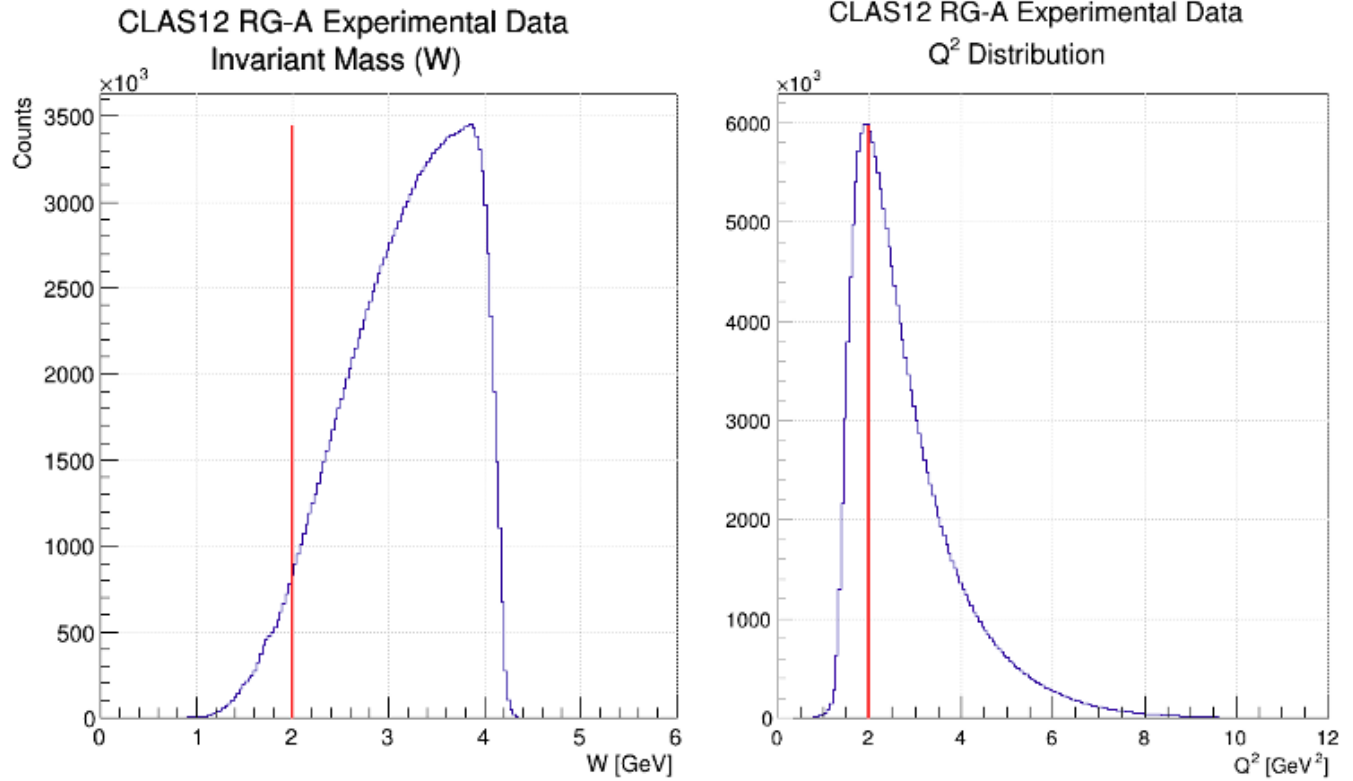


FIG. 52: Kinematic Cuts for Invariant Mass (W) and Q^2 . The red lines show the placements of the cuts (See the [Data Analysis](#) Section for more details).

³²²
³²³

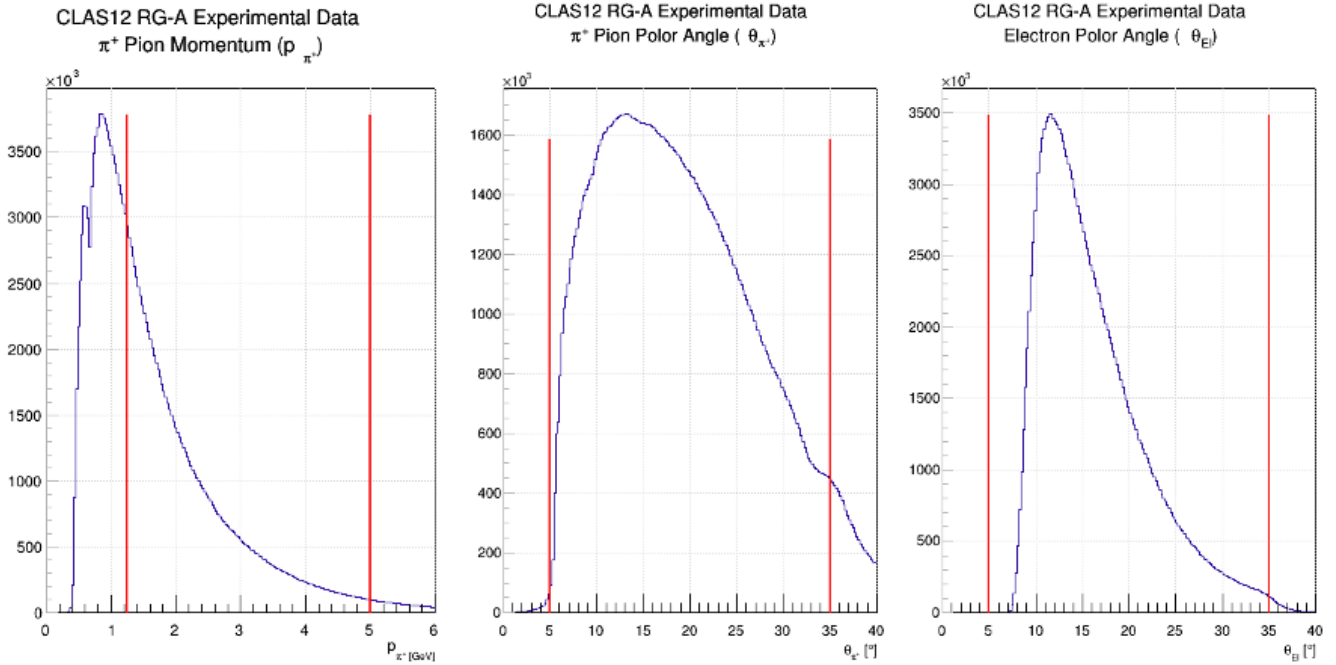


FIG. 53: Kinematic Cuts for the Pion Momentum and the Pion/Electron's Polar Angles. The red lines show the placements of the cuts (See the [Data Analysis](#) Section for more details).

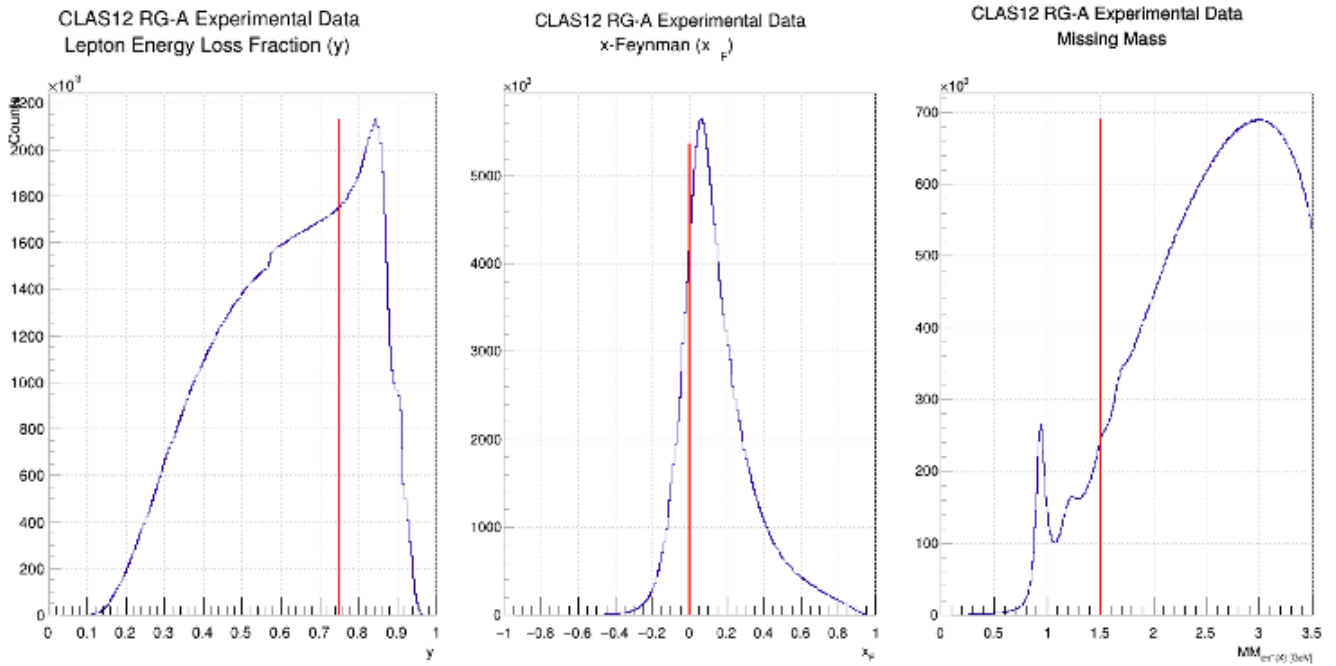


FIG. 54: Kinematic Cuts for y , x_F , and the Missing Mass distributions. The red lines show the placements of the cuts (See the [Data Analysis](#) Section for more details).

IX. APPENDIX

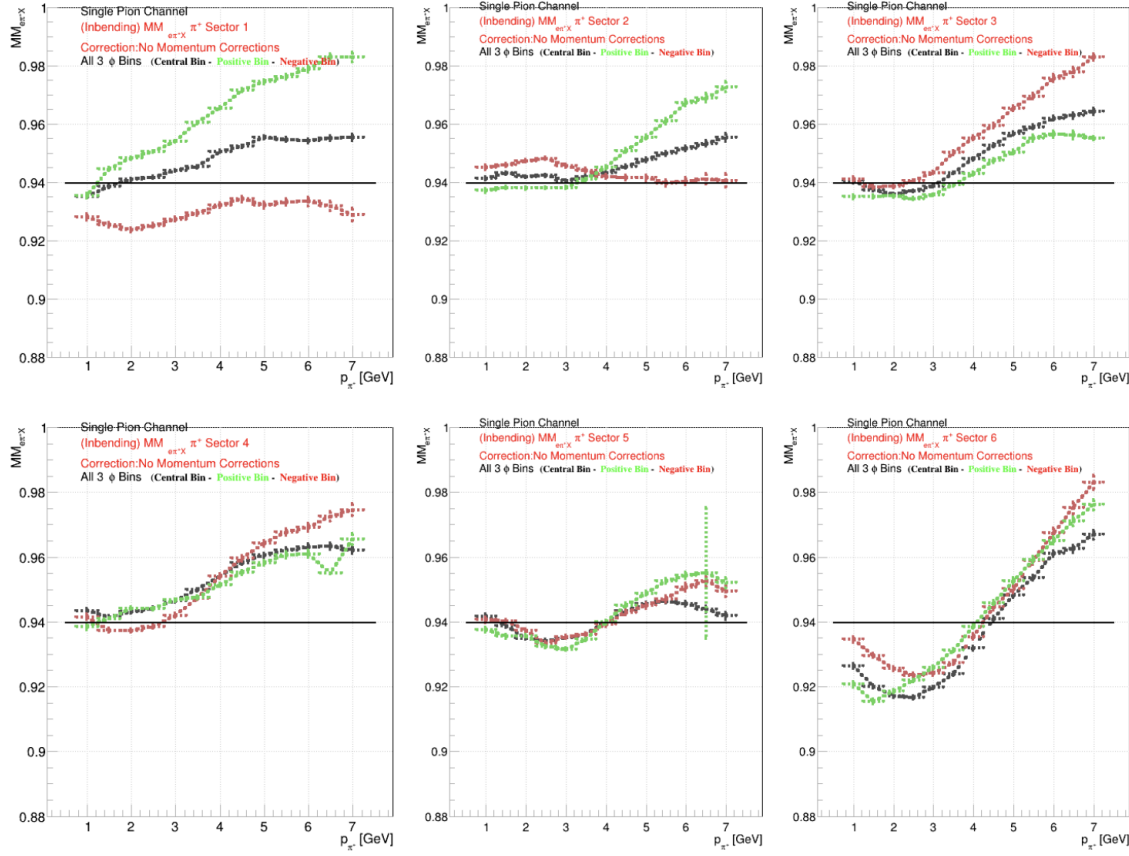


FIG. 55: Missing Mass vs. π^+ Pion Momentum in 3 ϕ bins. These plots show the deviation from the Neutron peak in the exclusive $ep \rightarrow e\pi^+N$ events **before** the momentum corrections are applied. See [CLAS12 Momentum Corrections](#) for more details.

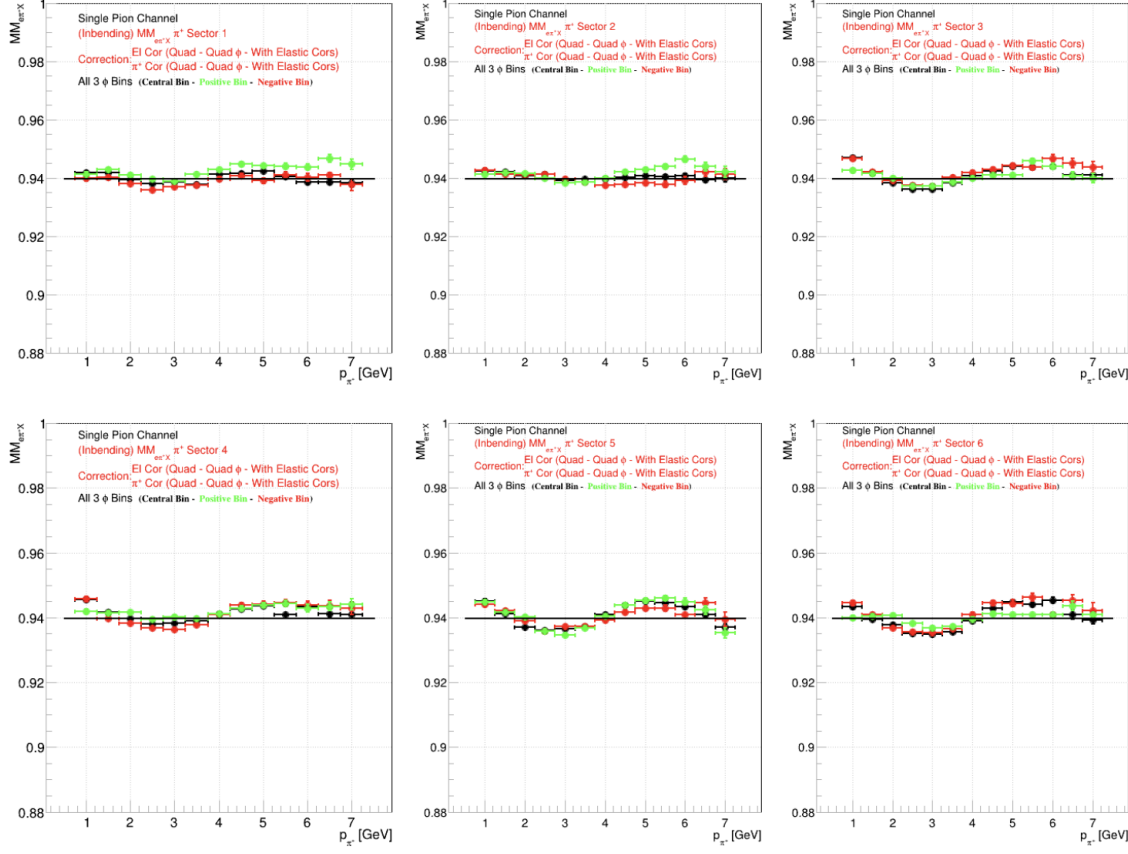


FIG. 56: Missing Mass vs. π^+ Pion Momentum in 3 ϕ bins. These plots show the improvements made by the corrections by bringing the Missing Mass peaks closer to the nominal value for exclusive $ep \rightarrow e\pi^+N$ events **after** the momentum corrections are applied. See [CLAS12 Momentum Corrections](#) for more details.

325 Code not referenced in other analysis notes.

```

double func(double x, double k, double b){
    return k * x + b;
}

struct line{
    double k;
    double b;
};

double isOutOfLines(double x, double y, line topLine, line botLine){
    return y > func(x, topLine.k, topLine.b) || y < func(x, botLine.k, botLine.b);
}

bool BadElementKnockOut(double Hx, double Hy, int sector, int cutLevel);

bool BadElementKnockOut(double Hx, double Hy, int sector, int cutLevel){

    double widthChange = 0;
    if (cutLevel == 0) widthChange = -1;
    if (cutLevel == 2) widthChange = 1;

    if (sector == 5) return 1;

    if (sector == 1){
        double k = tan(29.5*3.1415/180);
        double b = -92;
        return (isOutOfLines(Hx, Hy, {k, b + widthChange} , {k, b - widthChange - 2.4}) &&
               isOutOfLines(Hx, Hy, {k, b + widthChange - 9.1} , {k, b - widthChange - 9.1 - 2.4}) &&
               isOutOfLines(Hx, Hy, {k, b + widthChange - 127} , {k, b - widthChange - 127 - 2.4}) &&
               isOutOfLines(Hx, Hy, {k, b + widthChange - 127 - 8} , {k, b - widthChange - 127 - 8 - 2.4}));
    }
    if (sector == 2){
        double k = tan(30.4*3.1415/180);
        double b = 120.5;
        return (isOutOfLines(Hx, Hy, {k, b + widthChange} , {k, b - widthChange - 4.4}));;
    }
    if (sector == 3){
        return ((Hx - widthChange) > - 303 || (Hx + widthChange) < -310);
    }

    if (sector == 4){
        double k = tan(-29.6*3.1415/180);
        double b = -232.8;
        return (isOutOfLines(Hx, Hy, {k, b + widthChange} , {k, b - widthChange - 3.5}));;
    }

    if (sector == 6){
        double k = tan(-30.6*3.1415/180);
        double b = -185;
        return (isOutOfLines(Hx, Hy, {k, b + widthChange} , {k, b - widthChange - 2}) &&
               isOutOfLines(Hx, Hy, {k, b + widthChange - 8.3} , {k, b - widthChange - 8.3 - 2.2}));
    }
}

return 0;
}

```

FIG. 57: Fiducial Cuts Developed by Valerii Klimenko. Hx and Hy are the coordinates of matched hit in the PCAL.

326
327

```

1 auto smear_func = [&](TLorentzVector V4){
2
3     // true simulated values (i.e., values of the unsmeared TLorentzVector)
4     double iM = V4.M();
5     double smeared_P = V4.P();
6     double smeared_Th = V4.Theta();
7     double smeared_Phi = V4.Phi();
8
9     TLorentzVector V4_new(V4.X(), V4.Y(), V4.Z(), V4.E());
10
11    // calculate resolutions
12
13    double smeared_ThD = TMath::RadToDeg() * smeared_Th;
14    double momS1 = 0.0184291 - 0.0110883 * smeared_ThD + 0.00227667 * smeared_ThD * smeared_ThD - 0.000140152 * smeared_ThD * smeared_ThD * smeared_ThD + (3.07424e-06) * smeared_ThD * smeared_ThD * smeared_ThD;
15    double momS2 = 0.02 * smeared_ThD;
16    double momR = 0.01 * TMath::Sqrt( TMath::Power(momS1 * smeared_P, 2) + TMath::Power(momS2, 2));
17    momR *= 2.0;
18
19    double theS1 = 0.004 * smeared_ThD + 0.1;
20    double theS2 = 0;
21    double theR = TMath::Sqrt( TMath::Power(theS1 * TMath::Sqrt(smeared_P * smeared_P + 0.13957 * 0.13957) / (smeared_P * smeared_P), 2) + TMath::Power(theS2, 2));
22    theR *= 2.5;
23
24    double phiS1 = 0.85 - 0.015 * smeared_ThD;
25    double phiS2 = 0.17 - 0.003 * smeared_ThD;
26    double phiR = TMath::Sqrt( TMath::Power(phiS1 * TMath::Sqrt(smeared_P * smeared_P + 0.13957 * 0.13957) / (smeared_P * smeared_P), 2) + TMath::Power(phiS2, 2));
27    phiR *= 3.5;
28
29    // overwrite EB (i.e., applying the smear)
30
31    smeared_Phi += TMath::DegToRad() * phiR * gRandom->Gaus(0,1);
32    smeared_Th += TMath::DegToRad() * theR * gRandom->Gaus(0,1);
33    smeared_P += momR * gRandom->Gaus(0,1) * V4.P();
34
35    V4_new.SetE( TMath::Sqrt( smeared_P * smeared_P + iM * iM ) );
36    V4_new.SetRho( smeared_P );
37    V4_new.SetTheta( smeared_Th );
38    V4_new.SetPhi( smeared_Phi );
39
40    return V4_new;
41
42};

43

```

FIG. 58: Smearing Function applied to reconstructed Monte Carlo events. Based on code by F.X. Girod.

```

//=====// Modified Smearing Function //=====//
auto smear_func = [&](TLorentzVector V4, int ivec){
    // True generated values (i.e., values of the unsmeared TLorentzVector)
    double iM = V4.M();
    double smeared_P = V4.P();
    double smeared_Th = V4.Theta();
    double smeared_Phi = V4.Phi();
    TLorentzVector V4_new(V4.X(), V4.Y(), V4.Z(), V4.E());
    // Calculate resolutions
    double smeared_ThD = TMath::RadToDeg() * smeared_Th;
    double momS1 = 0.0184291 - 0.0110883 * smeared_ThD + 0.00227667 * smeared_ThD * smeared_ThD - 0.000140152 * smeared_ThD * smeared_ThD * smeared_ThD + (3.07424e-06) * smeared_ThD * smeared_ThD * smeared_ThD;
    double momS2 = 0.02 * smeared_ThD;
    double momR = 0.01 * TMath::Sqrt( TMath::Power(momS1 * smeared_P, 2) + TMath::Power(momS2, 2));
    momR *= 2.0;
    if(ivec == 0){
        // From D(Pion) Sigma Vs Momentum distributions:
        momR *= (2.0694e-02) * (V4.P()) + (-1.1212e-01) * (V4.P()) + (7.1348e-01);
        momR *= (-5.2125e-02) * (V4.P()) * (V4.P()) + (2.3416e-01) * (V4.P()) + (-1.9974e-01);
        // From D(Pion) Sigma Vs Theta distributions:
        momR *= (-2.7657e-03) * (V4.Theta()) * TMath::RadToDeg() * (V4.Theta()) * TMath::RadToDeg() + (8.1714e-02) * (V4.Theta()) * TMath::RadToDeg() + (4.0196e-01);
        momR *= (-7.3974e-04) * (V4.Theta()) * TMath::RadToDeg() * (V4.Theta()) * TMath::RadToDeg() + (1.0908e-02) * (V4.Theta()) * TMath::RadToDeg() + (9.9876e-01);
    }
    if(ivec == 1){
        // From D(Pi+ Pion) Sigma Vs Momentum distributions:
        momR *= (-5.2125e-02) * (V4.P()) * (V4.P()) + (2.7110e-01) * (V4.P()) + (4.8534e-01);
        momR *= (-3.4607e-02) * (V4.P()) * (V4.P()) + (1.5836e-01) * (V4.P()) + (6.8845e-01);
        // From D(Pi+ Pion) Sigma Vs Theta distributions:
        momR *= (-5.7711e-03) * (V4.Theta()) * TMath::RadToDeg() * (V4.Theta()) * TMath::RadToDeg() + (2.4354e-02) * (V4.Theta()) * TMath::RadToDeg() + (6.6472e-01);
        momR *= (-1.3210e-03) * (V4.Theta()) * TMath::RadToDeg() * (V4.Theta()) * TMath::RadToDeg() + (3.5065e-02) * (V4.Theta()) * TMath::RadToDeg() + (8.3333e-01);
    }
    double theS1 = 0.004 * smeared_ThD + 0.1;
    double theS2 = 0;
    double theR = TMath::Sqrt( TMath::Power(theS1 * TMath::Sqrt(smeared_P * smeared_P + 0.13957 * 0.13957) / (smeared_P * smeared_P), 2) + TMath::Power(theS2, 2));
    theR *= 2.5;
    double phiS1 = 0.85 - 0.015 * smeared_ThD;
    double phiS2 = 0.17 - 0.003 * smeared_ThD;
    double phiR = TMath::Sqrt( TMath::Power(phiS1 * TMath::Sqrt(smeared_P * smeared_P + 0.13957 * 0.13957) / (smeared_P * smeared_P), 2) + TMath::Power(phiS2, 2));
    phiR *= 3.5;
    // overwrite EB (i.e., applying the smear)
    smeared_Phi += TMath::DegToRad() * phiR * gRandom->Gaus(0,1);
    smeared_Th += TMath::DegToRad() * theR * gRandom->Gaus(0,1);
    smeared_P += momR * gRandom->Gaus(0,1) * V4.P();
    V4_new.SetE( TMath::Sqrt( smeared_P * smeared_P + iM * iM ) );
    V4_new.SetRho( smeared_P );
    V4_new.SetTheta( smeared_Th );
    V4_new.SetPhi( smeared_Phi );
    return V4_new;
};

```

FIG. 59: Modified Smearing Function applied to reconstructed Monte Carlo events. Iterative procedure for modifications described in Description.

-
- 328 [1] A. Bacchetta, U. D'Alesio, M. Diehl, and C. A. Miller, "Single-spin asymmetries: The trento conven-
329 tions," *Phys. Rev.*, vol. D70, p. 117504, 2004.
330 [2] N. Harrison, "Exploring the structure of the proton via semi-inclusive pion electroproduction." Thesis,
331 University of Connecticut, available at [https://www.jlab.org/Hall-B/general/thesis/Harrison_](https://www.jlab.org/Hall-B/general/thesis/Harrison_thesis.pdf)
332 [thesis.pdf](https://www.jlab.org/Hall-B/general/thesis/Harrison_thesis.pdf), 2015.
333 [3] A. Bacchetta *et al.*, "Semi-inclusive deep inelastic scattering at small transverse momentum," *JHEP*,
334 vol. 02, p. 093, 2007.
335 [4] T. B. Hayward, "Dihadron beam spin asymmetries on an unpolarized hydrogen target with CLAS12." Thesis,
336 College of William & Mary, available at [https://www.jlab.org/Hall-B/general/thesis/](https://www.jlab.org/Hall-B/general/thesis/THayward_thesis.pdf)
337 [THayward_thesis.pdf](https://www.jlab.org/Hall-B/general/thesis/THayward_thesis.pdf), 2021.
338 [5] S. Diehl and K. Joo, "A multidimensional study of sidis π^+ beam spin asymmetry over a wide range of
339 kinematics.." Internal Note., 2020.
340 [6] CLAS, "11 GeV polarized electrons on liquid hydrogen target to study proton structure, 3d imaging,
341 and gluonic excitations, RG-A analysis overview and procedure." Internal Note, under review. Snap-
342 shot from August 2020: [https://clas12-docdb.jlab.org/DocDB/0009/000949/001/RGA_Analysis_](https://clas12-docdb.jlab.org/DocDB/0009/000949/001/RGA_Analysis_Overview_and_Procedures-08172020.pdf)
343 [Overview_and_Procedures-08172020.pdf](https://clas12-docdb.jlab.org/DocDB/0009/000949/001/RGA_Analysis_Overview_and_Procedures-08172020.pdf).
344 [7] M. Ungaro *et al.*, "The CLAS12 Geant4 simulation," *Nucl. Instrum. Meth. A*, vol. 959, p. 163422, 2020.
345 [8] H. Avakian, "clasdis." <https://github.com/JeffersonLab/clasdis>, 2020.
346 [9] T. Sjostrand, S. Mrenna, and P. Z. Skands, "PYTHIA 6.4 Physics and Manual," *JHEP*, vol. 0605,
347 p. 026, 2006.
348 [10] L. Mankiewicz, A. Schafer, and M. Veltri, "Pepsi: A monte carlo generator for polarized leptoproduc-
349 tion," *Comput. Phys. Commun.*, vol. 71, pp. 305–318, 1992.
350 [11] G. Ingelman, A. Edin, and J. Rathsman, "LEPTO 6.5: A Monte Carlo generator for deep inelastic
351 lepton - nucleon scattering," *Comput.Phys.Commun.*, vol. 101, pp. 108–134, 1997.
352 [12] A. Höcker and V. Kartvelishvili, "SVD approach to data unfolding," *Nuclear Instruments and Meth-
353 ods in Physics Research Section A: Accelerators, Spectrometers, Detectors and Associated Equipment*,
354 vol. 372, pp. 469–481, apr 1996.
355 [13] G. D'Agostini, "A Multidimensional unfolding method based on Bayes' theorem," *Nucl. Instrum. Meth.*
356 *A*, vol. 362, pp. 487–498, 1995.